# POLITECNICO
## MILANO 1863

SCUOLA DI INGEGNERIA INDUSTRIALE
E DELL'INFORMAZIONE

# FBG sensorized epoxy resin coupon: manufacturing process, mechanical properties, and hygrothermal aging.

TESI DI LAUREA MAGISTRALE IN
AERONAUTICAL ENGINEERING
INGEGNERIA AERONATUCA

Author: **Davide Airoldi**

Student ID: 952847
Advisor: Giuseppe Sala
Co-advisor: Pietro Aceti
Academic Year: 2022-23

# Abstract

Composite materials are widely used in the aeronautical field because of their excellent strength-to-weight ratios, making them ideal for use in structural applications such as aircraft wings, fuselages, and rotor blades. However, these materials are highly susceptible to degradation caused by environmental factors, such as moisture and temperature variations. The hygrothermal aging of composite materials is a complex process that involves both physical and chemical changes, leading to a reduction in the material's mechanical and chemical properties over time.

One of the challenges in monitoring the degradation of composite materials is that it is often difficult to detect and quantify the damage that occurs within the material. This is especially true for materials that are subjected to cyclic loading, which can cause microcracking and delamination that are not easily visible from the surface. Therefore, there is a need for non-destructive techniques to monitor the health of composite structures and detect any damage that may occur.

Fiber Bragg's Grating (FBG) sensors offer a promising solution to this problem. FBGs are optical sensors that use the principle of Bragg reflection to measure changes in strain, temperature, or relative humidity. They consist of a fiber-optic cable with periodic variations in its refractive index, which act as a reflector for a specific wavelength of light. When the fiber is subjected to perturbations, such as deformations or changes in temperature, the reflected wavelength shifts in proportion to the change in strain or temperature.

The aim of this research project is to develop and validate a methodology for using FBG sensors to monitor the hygrothermal aging of the composite materials. Specifically, the research will focus on characterizing the relationship between changes in the wavelength of the sensor and the strains caused by manufacturing process, moisture absorption, and thermal effects on the polymeric matrix of the composite materials. Moreover, tensile tests will be performed in order to determine if the material shows a loss in mechanical properties after hygrothermal aging, and if it is able to recover its original performances after a drying process.

The research will involve the design and fabrication of epoxy resin specimens with FBG sensors embedded within them. The specimens will be subjected to dry tensile test, hygrothermal aging cycles, conditioned tensile test, drying process, and dried tensile tests. During these procedures the resulting changes in the FBG wavelengths will be measured and the data will be analyzed to determine the correlation between the FBG wavelength shifts and the mechanical properties of the specimens.

The results of this research could have significant implications for the development of more reliable and robust composite structures for the aeronautical industry. These sensors could give the possibility to monitor the residual strains during manufacturing and conditioning processes and during the life cycle of the component. FBG sensors could help ensure the ongoing integrity of composite components, reducing the risk of failure and improving safety.

**Keywords:** fiber optic; fiber bragg's grating sensors; composite materials; epoxy resin; hygrothermal aging; mechanical properties; tensile tests; humidity; temperature; moisture absorption.

# Sommario

I materiali compositi sono ampiamente diffusi nel campo aeronautico per il loro eccellente rapporto tra proprietà meccaniche e peso, rendendoli ideali per l'uso in applicazioni strutturali come le ali degli aeromobili, le fusoliere e le pale dei rotori. Tuttavia, questi materiali sono sensibili agli effetti dovuti alle condizioni ambientali, come umidità e variazioni di temperatura. L'invecchiamento dovuto a questi fattori si manifesta sui materiali compositi attraverso processi chimici e fisici, che diventano sempre più rilevanti nel tempo, portando alla degradazione delle performance del componente, con la riduzione delle sue proprietà meccaniche.

Uno dei problemi nel monitorare la degradazione dei materiali compositi è che spesso è difficile rilevare e quantificare i danni che si verificano all'interno del materiale. Ciò è particolarmente critico per i materiali che sono sottoposti a carichi ciclici, che possono causare microfratture e delaminazioni non facilmente visibili dalla superficie. Pertanto, esiste la necessità di sviluppare tecniche non distruttive per monitorare la salute delle strutture composite per rilevare eventuali danni che possono verificarsi.

I sensori FBG (Fiber Bragg's Grating) offrono una soluzione a questo problema. I sensori FBG sono sensori ottici che utilizzano il principio della riflessione di Bragg per misurare le variazioni di deformazioni meccaniche, o deformazioni relative a temperatura e umidità assorbita. Essi consistono in un cavo in fibra ottica con variazioni periodiche del suo indice di rifrazione, che agiscono come riflettore per una specifica lunghezza d'onda della luce. Quando la fibra è sottoposta a perturbazioni, come deformazioni o variazioni di temperatura, la lunghezza d'onda riflessa si sposta di un valore proporzionale alla variazione di deformazione e temperatura.

Lo scopo di questo progetto di tesi è quello di sviluppare e validare una metodologia che permetta l'utilizzo dei sensori FBG nel monitoraggio dell'invecchiamento idrotermico dei materiali compositi. In particolare, la ricerca si concentrerà sulla relazione tra le variazioni di lunghezza d'onda del sensore e le deformazioni causate dal processo di fabbricazione, l'assorbimento di umidità e gli effetti termici sulla matrice epossidica utilizzata nei materiali compositi aeronautici. Inoltre, verranno effettuati test di trazione al fine di determinare se il materiale mostra una perdita delle proprietà meccaniche dopo l'invecchiamento idrotermico e se il componente è in grado di recuperare le sue prestazioni originali dopo un processo di asciugamento.

La ricerca prevede la progettazione e fabbricazione di provini in resina epossidica con sensori FBG incorporati al loro interno. I campioni saranno sottoposti a test di trazione a secco, cicli di invecchiamento idrotermico, test di trazione condizionati

dall'assorbimento di umidità, processi di asciugamento e test di trazione sui componenti asciugati. Durante questi procedimenti, verranno misurate le variazioni di lunghezza d'onda e i dati verranno analizzati per determinare la relazione tra le variazioni di lunghezza d'onda e le proprietà meccaniche dei provini.

I risultati di questa tesi potrebbero avere implicazioni significative per lo sviluppo di strutture aeronautiche più affidabili e robuste per l'industria aeronautica. Questi sensori potrebbero fornire la possibilità di monitorare le deformazioni residue durante i processi di produzione e di condizionamento e durante il ciclo vita del componente. I sensori FBG potrebbero contribuire a garantire il monitoraggio continuo dell'integrità del componente, riducendo il rischio di guasti e incrementando la sicurezza del velivolo.

**Parole chiave:** fibre ottiche; sensori fbg; materiali compositi; resina epossidica; invecchiamento igrotermico; proprietà meccaniche; test di trazione; umidità; temperatura; assorbimento di umidità.

# Contents

# Introduction

Epoxy resins are widely used as composite matrix phases in the aeronautic industry due to their excellent mechanical properties, low shrinkage, and high durability. However, producing defect-free specimens can be challenging, and understanding the material's behavior under different environmental conditions is crucial for ensuring its long-term performance. This thesis work aimed to address these challenges by investigating the production process of epoxy resin specimens and conducting mechanical tests to evaluate their properties under different conditions. The importance of this study stems from the fact that composite materials are increasingly being used in aircraft structures for their excellent performance and the optimal balance between the weight and mechanical properties. However, these materials are highly sensitive to aging due to environmental conditions. Before studying the behavior of the complete composite material, consisting of both matrix and reinforcing fibers, it is important to characterize the matrix phase alone to have a complete understanding of the origins of the problems mentioned before. One of the major issues affecting composite materials is prolonged exposure to humid environments, and since reinforcing fibers are often insensitive to moisture, the problem appears to arise from the matrix itself.

In the aeronautic field, minimizing downtime and maximizing aircraft availability is essential. This makes the development of a Structural Health Monitoring (SHM) system indispensable, as it enables real-time monitoring of component health, allowing for timely maintenance interventions. Optical fibers are increasingly gaining ground in this field due to their flexibility, the possibility of being incorporated into the components themselves, and their insensitivity to electromagnetic fields. In particular, for the achievement of the objectives of this thesis, two FBG sensors were used, which allowed monitoring during the production phase of resin specimens, thus determining any deformations and residual stresses in the material that could compromise its mechanical properties. Furthermore, these specimens were then immersed in a high temperature water tank to simulate a hot-wet environment and promote moisture absorption by the resin. Even during this phase, fiber optic sensors were used to observe the developed deformations. A tensile testing campaign was carried out to study the mechanical properties of the material both in dry conditions and after the conditioning process, in order to determine whether and to what extent moisture deteriorates the performance of the resin. To carry out these tests, the tensile testing machine present in the laboratory of the Politecnico di Milano was used, together with the use of a strain gauge that allowed for the recording of stresses and

deformations, which were then compared with those obtained from the fiber optics. This step was crucial to check the correct functioning of the FBG sensor even after prolonged water immersion. Furthermore, to verify whether the material was able to recover its mechanical properties after a drying phase, further tensile tests were performed on specimens that had been previously conditioned and dried to allow for the release of all moisture. Fiber optic sensors are still not widely used in monitoring moisture absorption. Therefore, the work carried out in this thesis is still of an exploratory and preliminary nature, but it aims to lay the foundation for a more developed study of these sensors and their use in aeronautical applications. This is because their use could allow for significant economic savings and a strong increase in aircraft safety.

# 1 State of the art

The aerospace community is under constant pressure for materials development to achieve improved performance. Specifically, there is the need to find materials with lighter weight, higher operating temperatures, and greater stiffness without excessively increasing the costs. This requirement leads to the development of composite materials, which have better tensile strength and resistance to compression than aluminum alloys, widely used in the aeronautical field.

Despite the good mechanical properties, composite materials could suffer fatigue and environmental damage. In the aeronautical field, a structural failure is not acceptable because it can cost human lives, beyond a significant financial loss. Therefore, it is crucial to plan a maintenance program that regularly assesses the integrity of the structure and, if necessary, repair or substitute any damaged component.

Another crucial requirement in the aeronautical field is to minimize downtime and maximize machine availability, as every moment the airplane is not working can lead to a significant financial loss. The development of Structure Health Monitoring (SHM) systems allows real-time monitoring of the structure, environment, and performance parameters through embedded or attached sensors. The primary goals of SHM are to reduce inspection time, increase availability, and improve safety and structure life.

This chapter provides an overview of composite materials, including their benefits, fabrication process, and common issues, with a particular emphasis on the effects of moisture absorption. It also explores the concept of Structural Health Monitoring and highlights the techniques currently used in the aerospace industry. [1]

## 1.1. Composite Materials

A composite material can be defined as a macroscopic combination of two or more distinct materials that have a recognizable interface between them. One material acts as a supporting matrix, while another material, such as fibers or particles, reinforces the entire structure. The first level of classification is the type of matrix, which can be ceramic, metallic, or polymeric. In aeronautical constructions, the matrix is typically polymeric and performs several functions, including:

- Giving shape and dimensional stability to the structural elements. [2]

- Stabilizing the fibers in compression.

- Transmitting loads to the fibers to take advantage of their mechanical properties.
- Allowing the overlap of different layers to create a laminate with multi-directional reinforcement.

The reinforcements can be in the form of particles or fibers, which can be continuous or discontinuous. In the aeronautical field, the reinforcements are typically fibers with lengths much greater than their thickness or diameter. Three common types of reinforcing fibers are glass fibers, carbon fibers, and Kevlar fibers. Reinforcing fibers can be placed in predefined directions and organized in woven or tridimensional laminates with multiple layers. Figure 1 shows a possible classification scheme for composite laminate types.
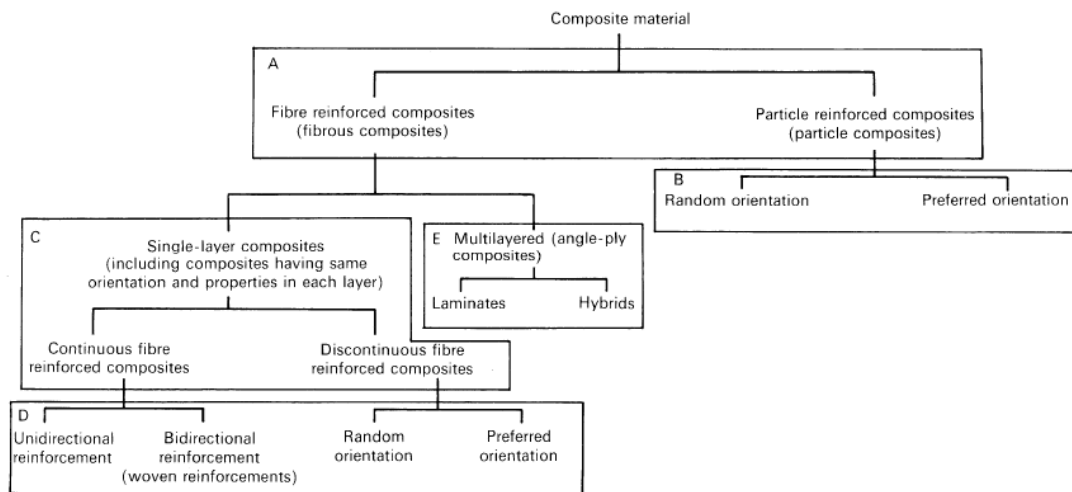


Figure 1 - Classification scheme of composite laminates

The mechanical properties of advanced composite materials make them of interest in aeronautical constructions. They increase structural efficiency, which is the structure's ability to satisfy stiffness and resistance requirements with the lowest possible weight.

The following table (Table 1) shows how the reinforcing fibers permit the development of new materials with a higher merit index.

| | Specific weight γ [] | Young Modulus E $[GPa]$ | E/ γ $[Mm]$ | Breakage stress $\sigma^R [Mpa]$ |
|---|---|---|---|---|
| Al | 26.3 | 73 | 2.8 | 500 |
| Ti | 46.1 | 115 | 2.5 | 1500 |
| Steel | 76.6 | 207 | 2.7 | 2000 |
| S Glass | 24.4 | 86 | 3.5 | 3500 |
| Carbon (high resistance) | 18 | 228-262 | 14 | 3000-4500 |
| Carbon (high E) | 18 | 353-393 | 21 | 2500 |

Table 1 – Mechanical properties of metallic alloy and fibers that are widely used in the aeronautical field.

One limitation of composites is that fibers can only transmit uniaxial stresses along their direction. Additionally, the presence of the polymeric matrix, which has lower mechanical properties, reduces the overall structural performance. As shown in Figure 2, it is possible to overlap unidirectional layers that are differently oriented, creating a multi-directional laminate that ensures optimal mechanical properties in every direction.
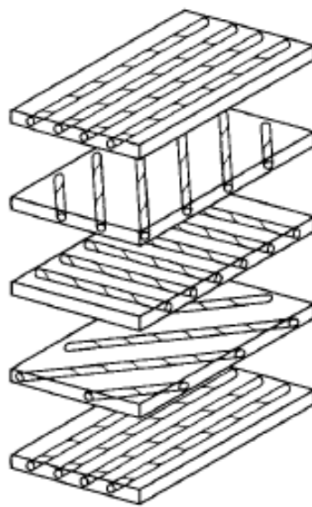


Figure 2 - Overlapping of uni-directional layers

The primary advantage of using composite materials is weight reduction, with weight savings in the range of 20-50% often quoted. The reduction of joints and bonded parts is another advantage, as composites allow the creation of unitized parts using automated layup machinery and rotational molding processes. For example, the Boeing 787 Dreamliner fuselage is a monocoque ("single shell") molded structure that delivers higher strength at a much lower weight. Aerodynamic benefits can be achieved with composites that were impossible with metals. Most "classical" metal aircraft control-lift surfaces have a single degree of curvature due to the limitations of metal fabrication techniques. Using composites further improvements in aerodynamic efficiency can be obtained by adopting a double-curvature design or variable-camber twisted wings. [1] [3]

### 1.1.1.   Manufacturing process of Aerospace Composites

The manufacturing process of composite materials involves depositing a matrix and fibers on a mold to shape them as required. There are various deposition techniques available, including spray-up or lay-up. The latter is commonly used in the aerospace field and it is divided into dry or wet lay-up. Dry lay-up is the most frequently used technique in aerospace constructions, which consists of the deposition of pre-impregnated fibers on a mold. The use of pre-impregnated fibers brings several advantages, such as a better distribution of matrix, uniform thickness of the layer, and excellent draping, cutting, and deposition that are easily automatable. However, they are difficult to conserve, and on-field reparations and cold curing are impossible.

The production process is divided into three phases: cutting, lamination, and curing. [4]

#### Cutting

It is essential to obtain the desired shape of the object from ribbons and coils. This process can be performed manually (low precision, repeatability, and production rates) or automated. The choice depends on the number of objects to produce. Two different approaches can be adopted: cutting directly with the final shape or cutting smaller pieces and organizing them to obtain the final shape.

A trade-off is necessary between the two techniques because the first is faster but produces a large quantity of shrinkage, and the second is slower but reduces the wastefulness.

Every procedure must be done in the *Clean Room*, as shown in Figure 3. It is a sterile room where is possible to control temperature, pressure, and humidity. This is essential because every impurity on the laminate could create damage to the structure [4].

Figure 3 - Politecnico's Clean Room

## Lamination

Once the desired shape is obtained through the cutting phase, the layers are organized to achieve the final laminate. This process can be done manually or automatically. In the manual process, a *Laser Projection System* projects the desired shape onto the mold, helping the operators to achieve the proper deposition of the layers. However, this method has some potential issues, such as poor deposition accuracy and the need for intermediate compaction every 4-5 layers. In contrast, an automated machine sucks the layers and arranges them in the correct position. The lamination process follows a ply-book that specifies how to perform each step correctly [4].

## Vacuum Bag

Once the laminate is ready, it is placed in a vacuum bag, which permits to:

- Evacuate air bubbles and reduce the empty spaces in the laminate.
- Evacuate volatile substances.
- Support layers adhesion.
- Allow compaction.

In addition to the layers, as shown in Figure 4, in the vacuum bag there are also:

- A peel-ply, which protects the surface.
- A bleeder, which absorbs the excess resin.
- A breather, which permits the exit of water, air, and gases [4].
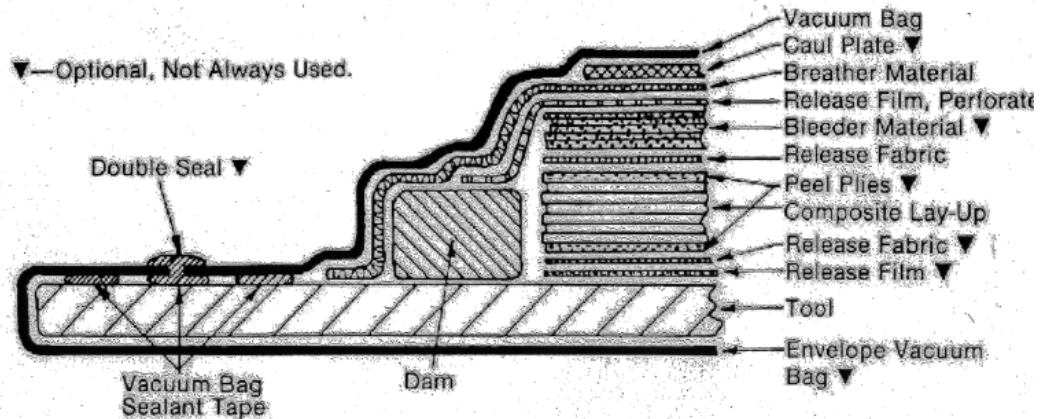
- A dam, which prevents the sliding of layers.



Figure 4 - Vacuum bag

## Curing Process

The last operation is the curing process, which irreversibly gives the material its final shape. It is a temperature and pressure cycle that makes the resin fluid and allows its distribution through the fibers.

The cycle can be carried out inside an autoclave, an oven, or a press. In the aeronautic field, the most commonly used method is the autoclave, which permits the production of high-quality components without any limits on dimensions, material types, accuracy, or roughness.

The autoclave is a thermally insulated oven where pressure can be controlled, and it ensures that vacuum is obtained in the vacuum bag. It is equipped with:

- A heating and air circulation system, which ensures homogeneous temperature distribution.
- A cooling system.
- A pressurization system.
- A vacuum pump for the bag
- A control system
- A handling system for the biggest components.

Curing is a delicate process, and it needs to follow specific gradients of temperature and pressure. Otherwise, an incorrect cycle can entail incomplete polymerization and distribution of the resin or lacking laminate compactness. Figure 5 shows the curing cycle in terms of temperature, pressure, and vacuum effect [4].
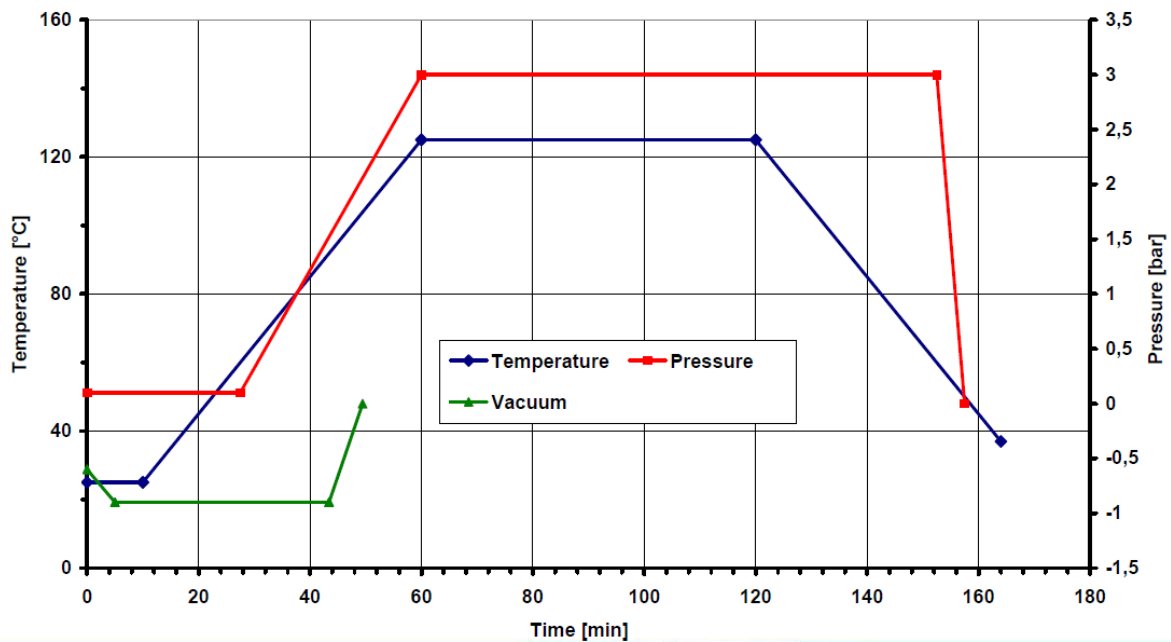
Figure 5 - Curing cycle

## 1.1.2. Composite damages

Composite materials offer various structural and functional advantages compared to traditional ones, but they also exhibit some behavior peculiarities and criticalities when exposed to fatigue, environmental effects, or accidental stresses.

This sub-section aims to introduce fatigue damages and examine in-depth hygrothermal effects.

### Fatigue damages

A central difference between composite materials and metals is the tendency to accumulate damage in a scattered and progressive way, rather than localized macro-cracks. There are four common different types of damage: progressive matrix damage, damage to the interface between the matrix and fibers, fibers breakage due to traction or compression stresses, and delaminations.

The first three types occur inside the thickness of a layer and are caused by stress components that act in the layer's plane. The last type is caused by transversal stress components outside the laminate's plane. The prevalence of a particular damage type is due to the material characteristics and the lamination sequence. Figure 6 shows the typical progression of damage in a composite laminate [5].
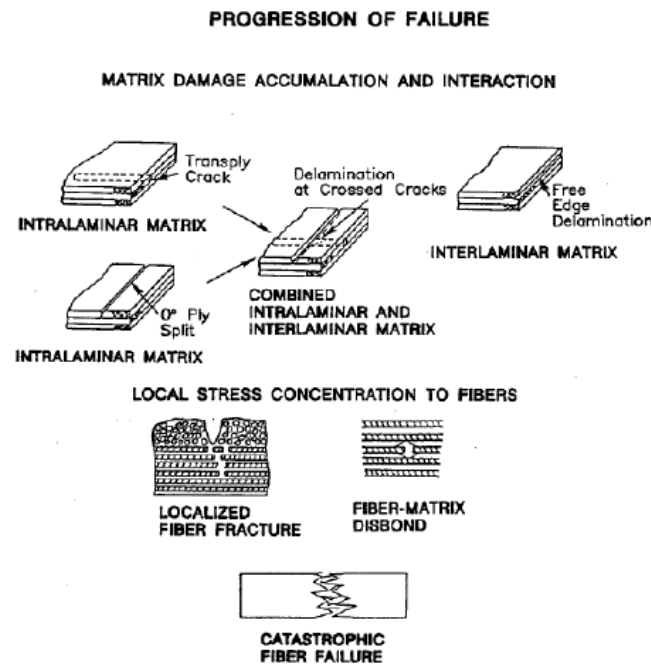
PROGRESSION OF FAILURE

MATRIX DAMAGE ACCUMALATION AND INTERACTION

Figure 6 - Typical failure in composite material

## Hygrothermal effects

Every composite material is sensitive to the effects caused by environmental conditions, in particular humidity and temperature variations. The hygrothermal aging of composite materials, which follows the absorption of humidity from the external environment, manifests itself through physical and chemical processes which become more and more relevant over time, leading to the degradation of the component's performances and the reduction of mechanical and physical properties. [6] [7]

Relative humidity and temperature are the most crucial environmental factors that impact the degradation severity of composite materials. In the initial phase of the humidity absorption process, moisture affects the resin, and then for longer exposures to humid environments, it also affects the interface region with the fibers. During hygrothermal aging, several physical-chemical processes occur simultaneously and affect each other [8]. The humidity absorption mechanism is described as a diffusion process, defined as the chemical process through which water molecules tend to move spontaneously from an area of high concentration toward an area of low concentration until an equilibrium condition is reached. Several factors can affect the absorption process, including matrix and reinforcements properties, degree of cure, porosity, polarity, environmental conditions, thickness, and design choices [2] [8] [9] [10] [11].

Composite materials are particularly vulnerable to moisture absorption because of the characteristics of the resin. The polymeric matrix used in composite materials features a strong hygrophilic behavior, explained by the presence of polar chemical groups, which spontaneously attract water molecules and form hydrogen bonds [12] [8] [13].

The hygrophilic nature depends on the morphology of the material, which presents porosities, voids, and free spaces, as seen in Figure 7 [8] [9] [10] [14] [15] [16].
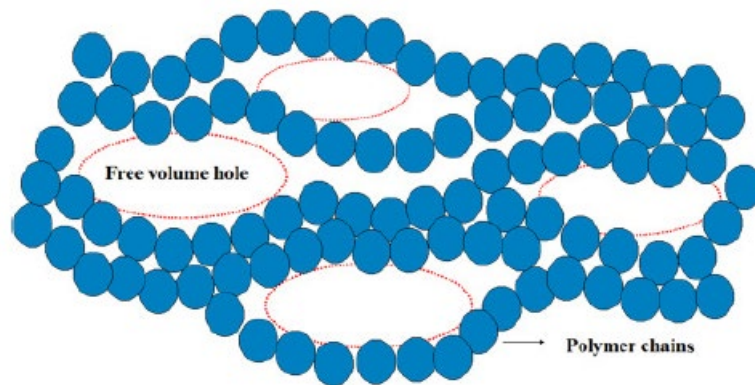


Figure 7 - Typical morphology of a polymer, which presents empty volumes where water molecules can accumulate during diffusion.

The diffusion rate also depends on external relative humidity and temperature conditions. In general, high levels of humidity and temperature accelerate the diffusion process.

The hygrothermal aging process can be divided into two phases [6] [7] [12] [17]:

- Physical processes: resin plasticization and swelling, reversible for short exposure time.

- Chemical processes: hydrolysis of chemical bonds and other secondary effects, which can cause irreversible damage to the material in the long term.

As water molecules move through the resin, the polymeric matrix undergoes a plasticization phase, which can be defined as a change in the morphology of the component, resulting in dimensional changes [18] [19] [20]. The absorption of water molecules induces a reorganization of the molecular chains of the polymer, by interacting with polar groups and reducing the intermolecular bond forces. This reduction increases the chain mobility, and the material passes from a glassy (stiff and brittle) to a rubbery (softer and tough) state, the so-called plasticization [21].

This change in chain mobility alters the mechanical properties, with a reduction of strength modulus and stiffness [21]. The most critical conditions are observed in the "*hot-wet*" conditions, characterized by high temperatures and high humidity concentration, as seen in Figure 8. [5]
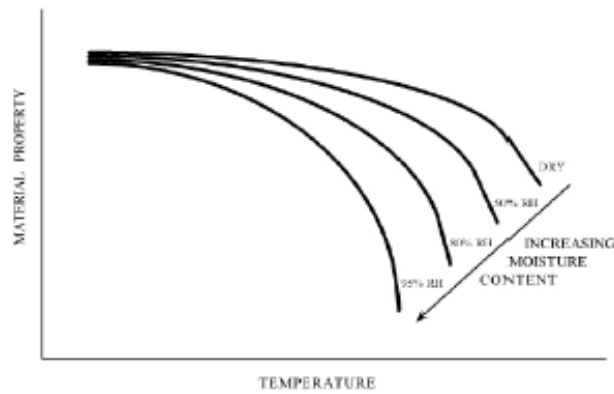
Figure 8 - Humidity and temperature influence on mechanical properties of a composite laminate

Plasticization can affect certain physical properties, especially the glass transition temperature $T_g$, which decreases as the material become softer [21]. This reduction in $T_g$ is directly related to the increase in the mobility of the polymer chains, which is in turn related to the degree of plasticization.

Another effect of plasticization is swelling, which is a dimensional change of the polymer caused by an increase in the free volume between the molecular chains. This is due to their increased mobility. Swelling is a visible effect of the increase in distance between the polymer chain molecules. Although water molecules are not completely free to move inside the polymer, their movement depends on the amount of free volume available. When water molecules fill the voids and form hydrogen bonds with polymer molecular chains, they cause an increase in the polymer's inner volume (swelling), which enhances a more intense diffusion and increases the absorption process, since the surface exposed to humidity is bigger. The increase in the free volume is associated with a reduction of intermolecular forces (Van der Waals), leading to the increased mobility of the polymer chains [21].

From a mechanical point of view, the swelling process induces the generation of additional stress states that lead to more intense total stress of the laminate. The total strain has three different contributions: mechanical ($\varepsilon_M$), thermal ($\varepsilon_{th}$), and hygroscopic ($\varepsilon_{hy}$). Thus:

$$\varepsilon_{tot} = \varepsilon_M + \varepsilon_{th} + \varepsilon_{hy}$$

( 1.1 )

Thermal stresses are directly proportional to the temperature variation $\Delta T$, through a thermal expansion coefficient $\alpha$. The orthotropic characteristics of the laminate induce different coefficients between the longitudinal ($\alpha_L$) and the transverse ($\alpha_T$) directions. Therefore, there are two different thermal strains:

$$\varepsilon_L^{th} = \alpha_L \Delta T$$

( 1.2 )

$$\varepsilon_T^{th} = \alpha_T \Delta T$$

( 1.3 )

Similarly, it is possible to define the hygroscopic deformations, which are related to the humidity content in the laminate (C). The moisture content is expressed as the ratio between the absorbed water mass ($m_w$) and the dry material mass ($m^0$). Thus:

$$C = \frac{m_w}{m^0} = \frac{m - m^0}{m^0}$$

( 1.4 )

Where $m$ represents the mass of the conditioned laminate. The dimensional variation of the laminate is proportional to the moisture content (under a linear behavior hypothesis), through a hygroscopic expansion coefficient $\beta$, which can be divided into $\beta_L$ (longitudinal direction) and $\beta_T$ (transverse direction). Such that:

$$\begin{pmatrix} \varepsilon_L^{hy} \\ \varepsilon_T^{hy} \\ \gamma_{LT}^{hy} \end{pmatrix} = \begin{pmatrix} \beta_L \\ \beta_T \\ 0 \end{pmatrix} C$$

( 1.5 )

The relation just exposed shows the absence of shear hygroscopic deformations and can be understood that the transverse (concerning the direction of the fibers) strain is maximum [5].

To better understand when moisture absorption can lead to reversible or irreversible effects, a distinction must be made between short/long-term exposures and action on the sole resin or the whole composite. When only the resin is considered, plasticization can be completely recovered. In general, immersion tests with diffusion up to saturation show that moisture absorption causes plasticization, which is recoverable with a drying procedure that brings the material back to the initial humidity level, with a complete recovery of mechanical properties. Hydrolysis, which is a molecular bond breakage, is not expected for limited expositions to humid environments (the period leading to saturation); otherwise, for longer exposure time, the aging processes become more and more complex and relevant, up to the point of causing non-recoverable deterioration of the polymer (proper breakage) [21].

When the reinforcing fibers are included in the material, its response to plasticization and, in general, to hygrothermal aging can differ significantly from the case of the sole resin. Fibers are generally impermeable to water or absorb much less water than resin, with a smaller diffusion coefficient. However, the presence of fibers in the material modifies the diffusion and aging process, as it promotes a differential swelling due to different diffusion and thermal expansion coefficients between fibers and matrix. These different coefficients can induce stresses in the transversal direction at the

fiber/matrix interface, which may lead to micro-cracks, new voids, and defects, creating new paths for water penetration and amplifying the damages [21]. The amount of damage depends on various factors such as the type of fibers, their volume fraction, and orientation. Natural fibers tend to absorb more water than standard ones like carbon and glass. The fiber volume fraction affects the amount of water absorbed as the fibers behave as barriers against moisture entrance. In the longitudinal direction, high mechanical properties are dominant, and the swelling deformation is almost negligible. However, the presence of fibers promotes water penetration at the fiber/matrix interface and induces capillarity effects that accelerate the diffusion process, resulting in water accumulation at the interface level [21].

When moisture acts on the interface, the effect is no longer only physical but also chemical. Water molecules promote the replacement and breakage of polymeric bonds, leading to irreversible loss of mechanical properties, since bonds do not reform after water removal. The interface deterioration is quantified through the reduction of the interfacial shear stress ($\tau_{ISS}$), which is derived from the interfacial energy following pull-out tests, after immersion tests, as reported in the equation below:

$$\tau_{ISS} = \frac{2\Delta E_{int}}{\pi d L^2}$$

( 1.6 )

Where $\Delta E_{int}$ is the difference of interfacial energy before and after the water absorption, $d$ and $L$ are respectively the reinforcement diameter and length.

In summary, the humidity response of the resin, fibers, and their interface is not the same, because water molecules interact differently, leading to different degradation mechanisms. The resin is a hygrophilic material, capable of absorbing large amounts of humidity, undergoing plasticization and swelling in the first phase of moisture absorption, with a recoverable reduction of mechanical properties. For prolonged aging, other processes such as oxidation, leaching, and hydrolysis start, leading to non-reversible effects. Fibers, on the other hand, undergo less humidity absorption since diffusion is obstructed, but they suffer a long-term degradation mechanism called dissolution, which is responsible for the removal of specimens with an irreversible reduction of weight. The interface is particularly susceptible to hydrolysis since it is made up of chemical bonds that ensure the cohesion between the fibers and the matrix. The interface is attacked by water molecules during hygrothermal aging (long-term exposure), leading to bond breakages, and a consequent reduction of stress transfer between matrix and fibers. Additionally, differential swelling generates stresses at the interface, leading to the formation of micro-cracks and debonding. A degraded interface is also responsible for further water penetration inside the composite, with the risk of increasing damage severity [21].

## 1.2.  Structural Health Monitoring (SHM)

In recent decades, the use of fiber-reinforced polymer (FRP) composites has increased in aerospace applications, as they offer a potential weight reduction in structural parts, leading to decreased fuel consumption, $CO_2$ emissions, and costs compared to metal structures. However, predicting the failure mechanism of composite materials remains challenging, as they may fail differently under different conditions, such as tension or compression, matrix and fibers materials, layup sequence, and environmental factors. Consequently, an over-engineered design is often required to comply with rigorous safety regulations, which counteracts the initial purpose of using composites for weight reduction.

To address this challenge, structural health monitoring (SHM) of aerospace composites is crucial to prevent unpredicted failures. Embedding sensing systems within the composite structure, capable of detecting critical parameters such as strain, temperature changes, or moisture absorption, can improve the ability to monitor the in-service structural health and the manufacturing process. This provides an alternative to existing non-destructive inspection (NDI) techniques, which are typically used at the end of major process steps and their application is limited by the size of the structure. The embedding of sensors provides extra protection against the operational environment, increasing the lifetime of the sensors and the composite structure. Implementing SHM into aircraft provides various benefits such as:

- **Availability**: more efficient and effective maintenance procedures with reduced downtime. Furthermore, a substantial time-saving inspecting parts that are difficult to access.

- **Safety**: early detection and diagnosis of defect/damage and improved design efficiencies through continuous monitoring.

SHM also provides economic advantages, as shown in Figure 9, by allowing the actual level of consumption of the component to be known. If the component undergoes mild usage, its service life can be extended until the mild usage line reaches the design life of the component, earning service time corresponding to the green zone in Figure 9. Otherwise, without an SHM system, the structure is substituted when the predicted service time is reached. If the structure undergoes a more severe usage than the predicted one, the final life consumption is reached before the predicted one. Without an SHM system the component is still used until the predicted time but in this last part (the red one in the graph) the material is at risk of failure. With SHM, the structure can be replaced in advance to prevent this risk of failure, increasing safety.

Overall, SHM sensor technology is a cost-effective approach that increases the lifetime of the composite structures by providing continuous data to repair and maintain the

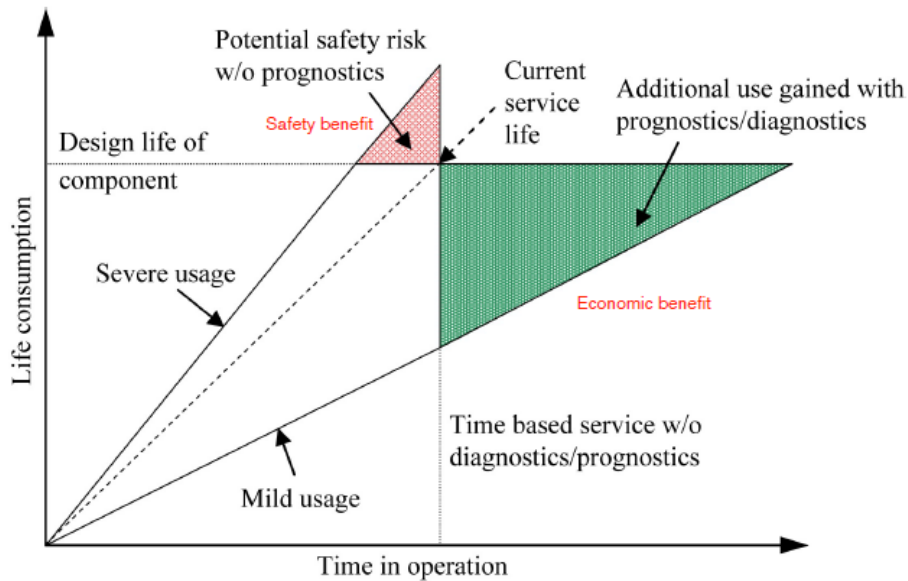part promptly, reducing unnecessary maintenance operations of aircraft structures [22].



Figure 9 - SHM economic and safety benefits

The working principle of an SHM system consists of several different steps:

1. Interaction between sensors and material/structure

2. Analysis

3. Diagnosis:

   a. Detection and monitoring of characteristic parameters (such as flaws, stress/strain, etc.).

   b. Detection of whether the damage is present in the structure.

   c. Identification of the location of the damage.

   d. Quantification of the severity of the damage.

4. Prognosis:

   a. Prediction of the evolution of damage

   b. Evaluation of remaining structural integrity

   c. Risk assessment and definition of maintenance procedures
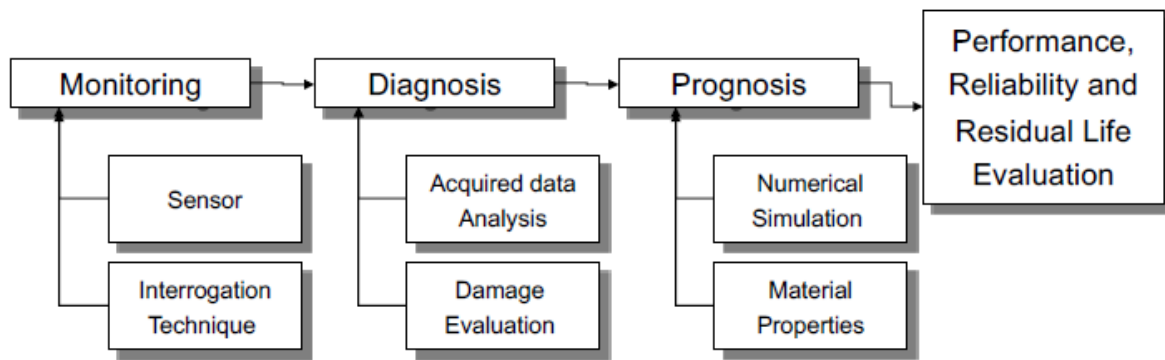
Figure 10 - SHM principles and set-up

The implementation of SHM systems is essential to ensure that the interrogated structures can perform properly and survive the harsh aerospace environment to which they are exposed throughout their working lifetime. Generally, aerospace applications require lightweight, small, and low-power-consuming monitoring systems that are immune to electromagnetic interference. Furthermore, a sensor for SHM should fulfill a few basic specifications:

1. It should only monitor the real damage condition of the host structure and be independent of changes in the environment.

2. It should reliably transmit the acquired signals.

3. It should produce as little impairment as possible on the host structure.

4. It should survive the surrounding work environment for at least as long as the service life of the host structure.

5. It should be easy to handle, attach, integrate, and operate.

6. It should preferably have a low cost.

As shown in Figure 10, a complete SHM system comprises not only sensors, but also a data acquisition system, data storage hardware, and algorithms for signal processing. Therefore, it involves interdisciplinary engineering fields [23].

Implementing SHM systems provides several benefits. Firstly, it ensures that structures are functioning correctly and efficiently. Secondly, it can detect damages early on, leading to a lower risk of structural failure and improved safety. Thirdly, it allows for more efficient and effective maintenance procedures, which can reduce downtime and costs. Lastly, SHM systems can provide insight into the actual usage of a component, allowing for better prediction of the remaining lifespan and replacement timing.

## 1.3.  Humidity Sensors

Monitoring moisture absorption in composite materials is crucial in the aeronautical field as it can significantly affect the structural integrity and performance of aircraft components. As presented in Section 1.1.2, composite materials are prone to moisture absorption, which can lead to several problems such as dimensional instabilities, delamination, degradation of mechanical properties, and reduction in fatigue life. Therefore, monitoring moisture absorption in composite materials is critical for ensuring the structural integrity, reliability, and safety of aircraft components. It allows for the timely detection of any moisture-related issues, enabling prompt maintenance and repair action to be taken.

In this section, some of the most widespread techniques for moisture absorption measurement are:

1. **Capacitive sensors**: these sensors measure the change in capacitance that occurs when a dielectric material (such as a composite material) absorbs moisture. The capacitance change can be used to determine the amount of water that has been absorbed.

2. **Resistive sensors**: these sensors measure changes in electrical resistance caused by moisture absorption. The sensors typically consist of a conductive material that is coated with a moisture-absorbing layer.

3. **Piezoelectric sensors**: these sensors measure changes in the voltage or current generated by a piezoelectric material (such as quartz) when it is subjected to pressure or stress. When a composite material absorbs moisture, it can cause changes in pressure or stress that can be detected by the sensor.

4. **Quartz crystal microbalance (QCM) sensors**: these sensors measure changes in the mass of a quartz crystal caused by moisture absorption. As the crystal absorbs moisture, its resonant frequency changes, which can be measured and used to determine the amount of water that has been absorbed.

5. **Fiber optic sensors**: these sensors use the principle of light reflection to measure moisture absorption. A fiber optic cable is placed in contact with the composite material, and changes in the refractive index of the material or in the length of the cable due to moisture absorption cause changes in the wavelength of the reflected light. This type of sensor is analyzed in depth in Section 1.4.1.

## 1.4. Optical Fibers

Recent advances in sensors, microelectronics, and adaptive signal processing technologies have revolutionized the traditional approaches to dealing with problem-solving. These technological development have allowed mechanical systems to achieve optimal functionality, similar to biological systems such as the human brain and body. These systems, which are known as smart, adaptive, and intelligent, could mimic human muscular, sensory, and nervous system by employing embedded sensors, actuators, advanced signal processing, and control capabilities. Among the sensors suited for incorporation into materials and structures and for the realization of such adaptive and smart systems, optical fibers are considered to lead the pack in sensor technology. If successfully implemented, this technology is posed to revolutionize the approaches to systems' health monitoring and management, performance assessment, and implementation of adaptive systems and structures. Because of their very low weight, small size, high bandwidth, and immunity to electromagnetic and radio frequency interferences, fiber optic sensors have significant performance advantages over traditional sensors. They offer unique capabilities, such as:

- Monitoring the manufacturing process of composite and metallic parts.

- Performing non-destructive testing once fabrication is complete.

- Enabling structural and component health monitoring for prognosis health management.

- Ensuring structural control for component life extension.

In contrast to classical sensors that are largely based on measurements of electrical parameters such as resistance or capacitance, fiber optic sensors use a variety of novel phenomena inherent in the structure of the fiber itself. As a result, the ability of fiber optic sensors to displace traditional sensors for rotation, acceleration, electric and magnetic fields measurement, temperature, pressure, acoustics, vibration, linear and angular position, strain, humidity, viscosity, chemical measurements, and a host of other sensor applications have been enhanced [24].

The structure of the fiber, as shown in Figure 11, is coaxial and divided as follows:

- Core: is an $8\ \mu m$ diameter glass filament for single-mode fibers and $50 - 62.5\mu m$ for multi-mode fibers. It is in the middle and its refraction index is about 1.5.

- Cladding: it surrounds the core and can reach $125\mu m$ for the external diameter. It is also made of glass but characterized by a slightly lower refraction index (about 1.475) and, together with the core, constitutes the real guide for the signal.

- Coating: it is a protective layer aimed to give greater resistance to the fiber. It can be polyimide ($170\mu m$), acrylate ($250\mu m$), or Ormocer ($195\mu m$) with different mechanical properties.

- Jacket: the most external component. It is an additional protective sheath made of polymeric material. The color of this element identifies the type of fiber [25].
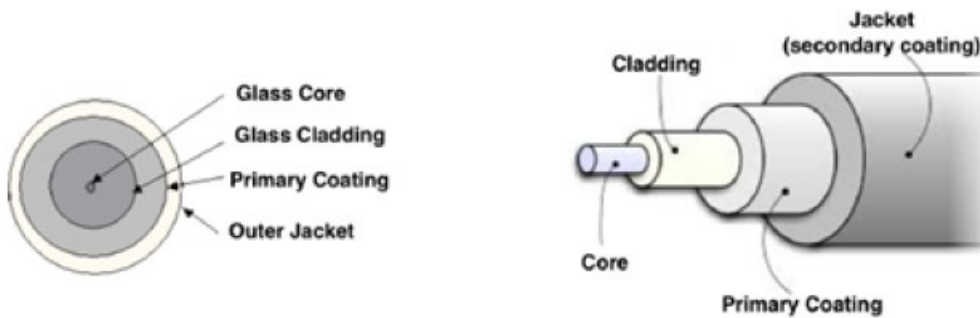
Figure 11 - Optical fibers structure

## Working principle

The optical fiber behaves like a conductor which confines the light inside it through the phenomenon of total reflection, which is a particular case of the refracting phenomenon whereby a beam of light passing through two different materials, with different refracting indices, changes its direction. Core and cladding have two different refractive indices that create a waveguide for light propagation, which permits the transmission of the signal through the core. The ratio between the two refracting indices is directly proportional to the sinus of the refracting angles, as shown by the Snell law:

$$n_1 * \sin(\theta_I) = n_2 * \sin(\theta_T)$$

( 1.7 )
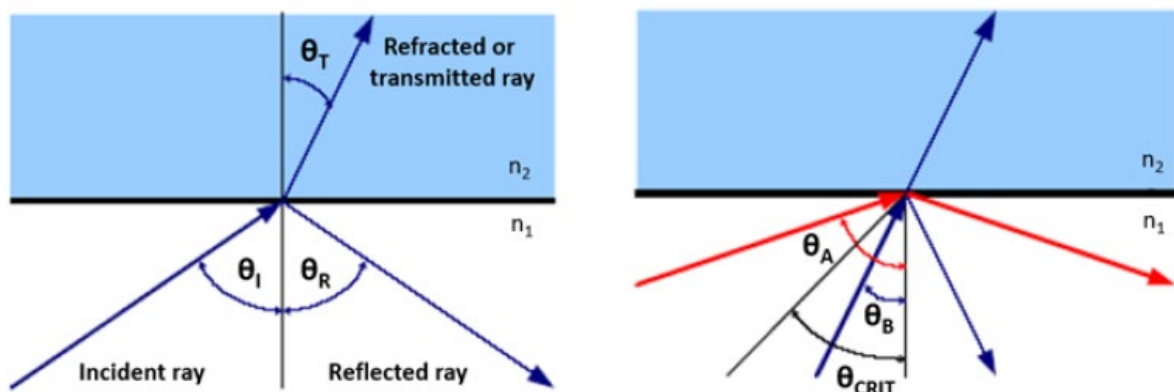
Figure 12 - Refracting phenomenon

Where referring to Figure 12, $\theta_I$ is the angle of the incident beam, and $\theta_T$ is the angle of the refracted one. Total reflection occurs when $\theta_T$ reaches the amplitude of 90° because there is no longer a refracted wave. This condition brings to a critical value of $\theta_I$:

$$\theta_I \geq \theta_{cr} = \arcsin\left(\frac{n_2}{n_1}\right)$$

( 1.8 )

Figure 12 shows two light rays that affect the interface between the core and the cladding inside the optical fiber. Beam A hits with an angle $\theta_A$ greater than $\theta_{cr}$ and remains trapped in the core because it is totally reflected. Beam B hits with an angle lower than $\theta_{cr}$ and it is therefore refracted in the cladding and lost. Not all the light beams entering the core will be able to travel through it. The acceptance cone (reported in Figure 13) is therefore defined as the limit within which the rays must be introduced into the fiber to guarantee their total reflection without excessive attenuation and loss of signal intensity.
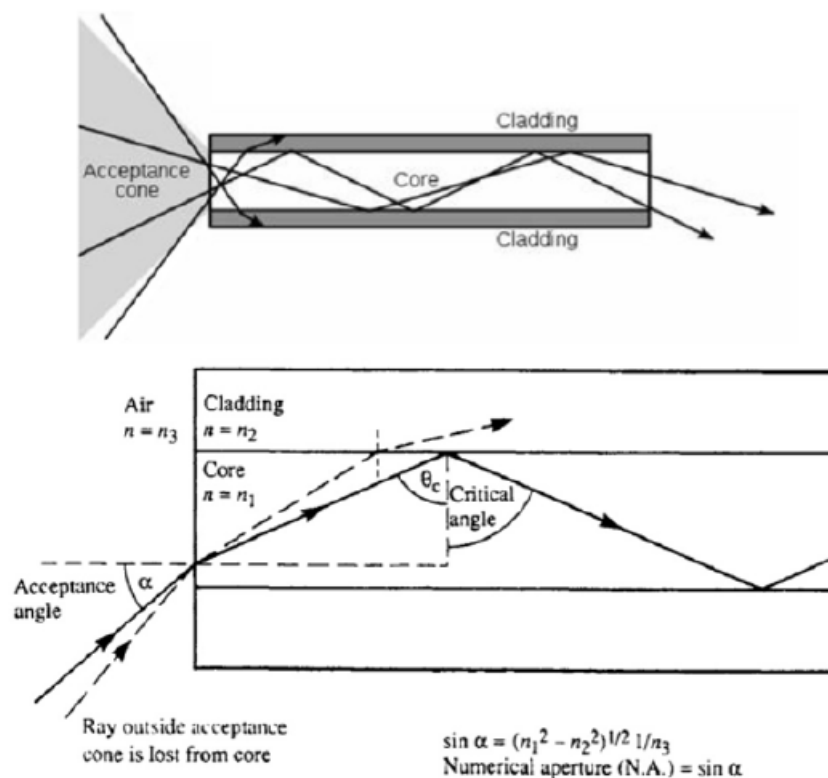


Figure 13 - Acceptance cone

This phenomenon generates a certain limit in the use of the optical fiber itself: it is necessary to pay attention not to subject it to too narrow bending angles, otherwise, the total or partial loss of signal will occur, as shown in Figure 14.
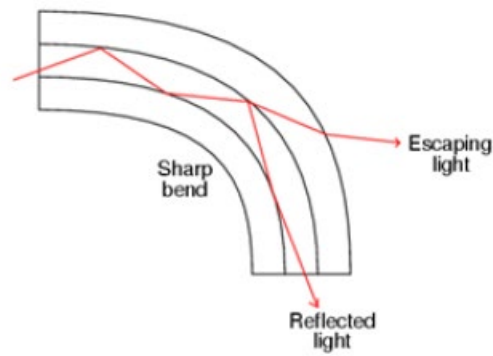
Figure 14 - Signal loss due to fiber bending

The signal exiting from the source has known characteristics in terms of amplitude, phase, and frequency. If the component undergoes a perturbation, like deformation, temperature change, humidity absorption, vibrations, and others, the fiber embedded in it feels the effect of this perturbation, and the signal that reaches the processors will have different properties. Thanks to this phenomenon it is possible to link physical phenomena with optical ones and to monitor possible damages in the component [25].

## 1.4.1.  Fiber optic sensors

The fiber optic sensors are divided into three categories: integral, discrete, and distributed sensors. The integral sensors permit to obtain information as an average of what is detected inside the structure, and this implies that if the difference between the maximum and minimum peaks intensity were significant, there would be a considerable loss of information. The discrete sensors, on the other hand, provide highly detailed information on the stress state of the host material, but only in restricted points in the order of a few millimeters. Finally, the distributed sensors can perform measurements along the entire length of the optical fiber [26].

### Mach-Zehnder interferometric sensor (integral)

The first example of an optical fiber sensor is the Mach-Zehnder interferometric sensor, represented in Figure 15, which is an integral sensor because it is based on the comparison of two different signals generated by the same source.
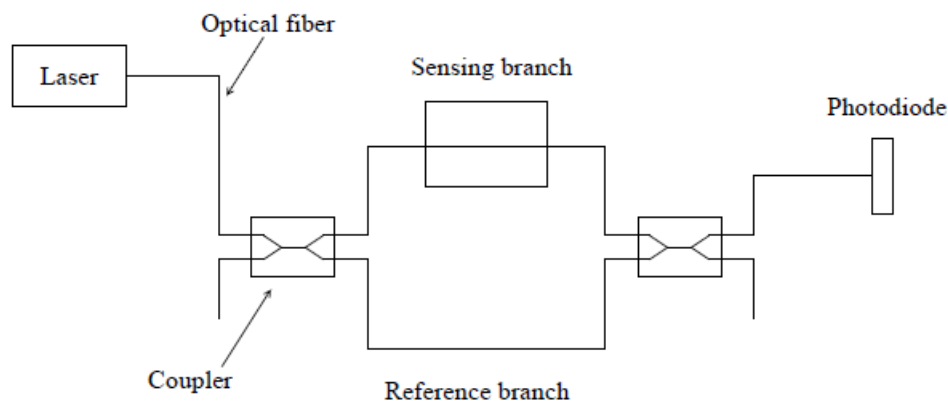
Figure 15 - Mach-Zehnder interferometric sensor structure

The starting signal is divided by the coupler (that works as a splitter) in a sensing branch and a reference one. The first one is embedded in the component while the other is free. If the component does not undergo any deformation, the signal does not change, so the sensing branch and the reference one bring the same signal that reaches the photodiode with a certain phase and gives an image. Otherwise, if the component suffers a deformation, the sensing branch signal changes and does not correspond to the reference one. The image obtained in the photodiode is different and the perturbation is linked to a phase shift of light due to the deformation of the component.

With an easy working principle, it is possible to link physical phenomena with a signal perturbation in terms of a phase shift of light. Moreover, the Mach-Zehnder sensor guarantees high sensitivity, but the reference branch is difficult to insulate, and this sensor cannot perform local measurements because the deformation could be in every point of the component [24].

### Michelson interferometric sensor

Like the Mach-Zehnder sensor, the Michelson one uses a phase shift of the light to measure physical phenomena on the component. A light beam is divided by the coupler into two branches, which are identical until they reach the component, where one branch is longer than the other. When the signal comes to the end of the fibers, the light is reflected and returns, it is again coupled, and it reaches the photodiode. The length difference between the two branches entails an offset in the returning signal, which is known. If the sensing length undergoes a deformation, the offset will change and it permits the detection of external phenomena that occur in the last piece of the fiber, producing a local measurement with high sensitivity. On the other hand, this type of sensor is difficult to embed in composite without invasivity and it is difficult to couple the branches because they must be parallel. In Figure 16, a scheme of the Michelson sensor is represented [24].
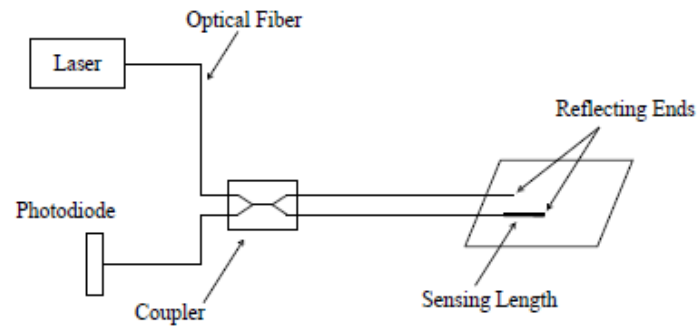
Figure 16 - Michelson interferometric sensor scheme

### Fabry-Perot interferometric sensor

To avoid the coupling problem of the branches, the Fabry-Perot sensor uses a single fiber to measure physical phenomena. The light beam, through the fiber, comes to the component where the fiber has a capillary tube with two fibers facing each other, leaving a small distance between the two which creates the Fabry-Perot cavity, as represented in Figure 17. The ends of this cavity are characterized by two semi-reflecting planes. When the light reaches the cavity, part of the signal will be reflected and part of it reaches the other reflecting plane, where the signal will be mirrored. If the length of the cavity changes, the phase shift between the two reflected signals will also change. This perturbation is related to the deformation of the cavity, linked to several physical phenomena on the component.
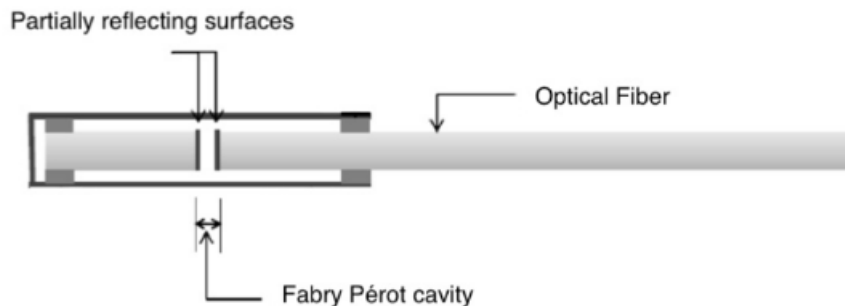


Figure 17 - Fabry-Perot cavity

Figure 18 - Fabry-Perot interferometric sensor structure

The Fabry-Perot interferometric sensor is characterized by high sensitivity and low invasivity, but it is not easy to restore the continuity of the fiber [24].

### Rayleigh, Raman, and Brillouin scattering sensors

They are sensors based on the phenomenon of diffusion that allows to carry out temperature and deformation measurements. When a ray of monochromatic light hits

a material, it is possible to observe its fragmentation in terms of the spectrum of the signal. If the frequency of the new waves is equal to that of the impacting waves, the phenomenon is called Rayleigh scattering. On the contrary, when a signal of intensity $I$ passes through the fiber and two new signals are generated, one with greater amplitude ($I_A$), and one with a minor one ($I_S$) concerning the original one, it is called the Raman diffusion phenomenon. The relative intensity of anti-Stokes signals depends on the local temperature of the fiber and, for this reason, sensors based on Raman diffusion allow distributed temperature measurements. Brillouin scattering in optical fibers provides a means of measuring distributed strain and temperature along the fiber. The stimulated Brillouin scattering (SBS) is usually described as the interaction of two opposite propagating waves, an input laser wave (pump) and a Stokes wave. If phase-matching conditions are met, an acoustic wave is generated:

$$f_{pump} = f_{Stokes} + v_B$$

( 1.9 )

This acoustic wave scatters photons from the pump to the Stoke wave, stimulating the process. From a practical point of view, the process of SBS can be viewed as a narrowband amplification, in which a continuous-wave pump produces a narrowband ($30 - 50\, MHz$) gain in a spectral region around $f_{Stokes} = f_{pump} - v_B$. Brillouin-based sensors are competent at distributed sensing along the fiber, making them advantageous [27].
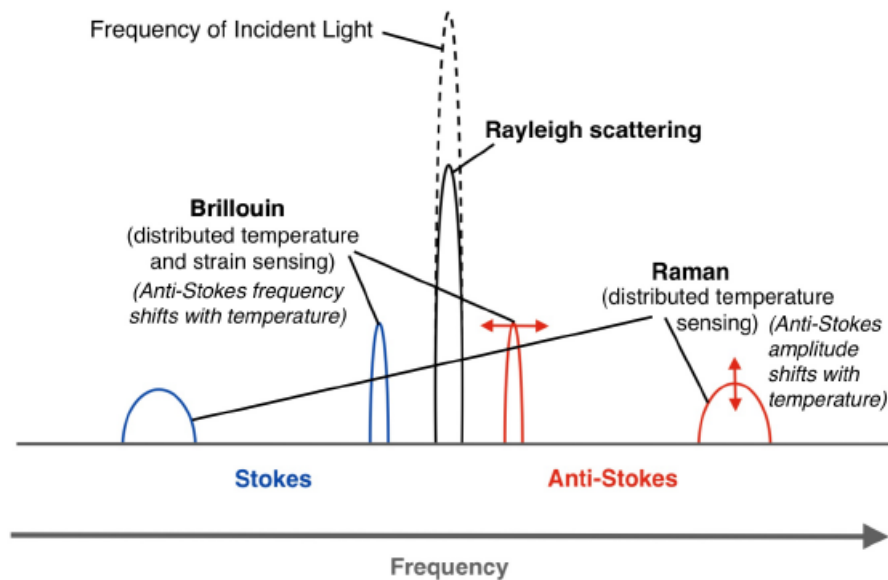


Figure 19 - Distributed sensors based on diffusion phenomena

## Fresnel Reflection Refractometers (FRR)

These sensors allow to measure temperature variations, refractive index changes, and mechanical stresses based on the principle of reflection inside the optical fibers, as previously illustrated. The light, after passing through the optical fiber, leaves it,

entering the medium. Part of the signal is therefore dispersed and partly reflected once again in the fiber. The amount of reflected light can be measured and, since this value is affected by any folding of the fiber and its expansion or contraction due to temperature variations or mechanical stresses, it is possible to use this technology as a sensor [27].
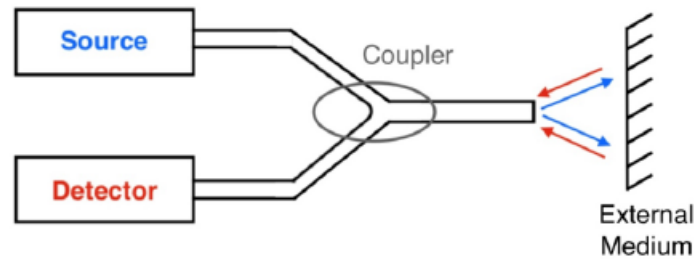
Figure 20 – FRR

## 1.4.2. Fiber Bragg Grating Sensors (FBG)

Fiber Bragg grating has embraced the area of fiber optic since the days of its discovery, and most fiber optic sensor systems today make use of FBG technology. Researchers have gained enormous attention in the field of FBG-based sensing due to its inherent advantages, such as small size, fast response, distributed sensing, embedment possibility, and immunity to electromagnetic fields. These sensors are popularly used in measurements of various physical parameters, such as pressure, temperature, humidity, and strain for civil, industrial, military, and aerospace engineering applications [28].

### 1.4.2.1. Theory of FBGs

The Fiber Bragg Grating sensors are intrinsic sensors, in which the physical parameter to be measured directly interacts with the optical fiber and modifies the characteristics of the light, which remains however always confined within the fiber.

The FBGs are formed by a periodic modulation of the refractive index of the fiber core along the longitudinal direction. To inscribe the grid, the fiber is appropriately doped so that it becomes photosensitive, so it can modify the local value of the core refractive index ($n$) when it is exposed to a suitable energy source, such as a laser beam.

The parameters that characterize an FBG are:

- $\Lambda$ is the period of the grid.
- $L$ is the length of the grid.
- $n_{eff}$ is the effective refraction index of the grid.
- $\lambda_b$ is Bragg's wavelength.

- $\Delta_n$ is the variation of the refractive index of the grid.

When the light travels inside the grating structure, some portion of light gets reflected from each grating plane. Each pair of fringes reflects a small part of light at a specific wavelength $\lambda_b$. The reflection spectrum has specific characteristics, which depend on the grating period and effective refractive index, as shown below by the Bragg condition:

$$\lambda_b = 2n_{eff} * \Lambda$$

( 1.10 )
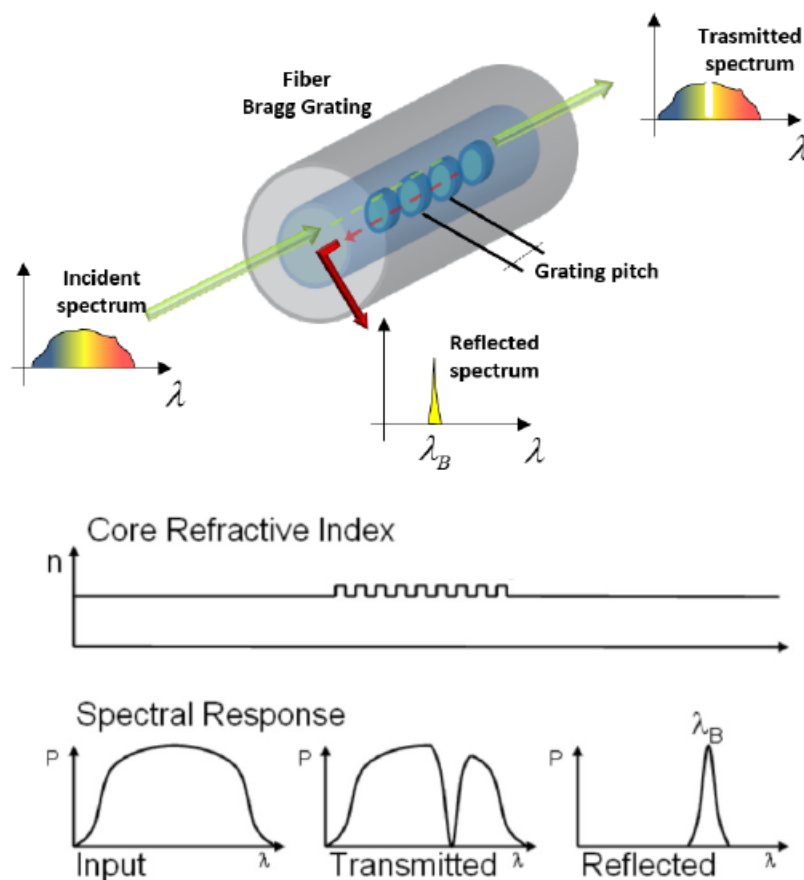


Figure 21 - Constant Bragg Grating

The sensor works on the principle of wavelength shift. If all the fringes are equal, the reflected light has a single peak at $\lambda_b$, given by the sum of the contributions of each pair of fringes (Figure 21). Any perturbation, due to physical phenomena, causes a variation of $L$, $\Lambda$, or $n_{eff}$ on the grid, which shifts $\lambda_b$ (Figure 22), which is reported in the reflection spectrum. It is possible, in this way, to obtain the measurement of the observed quantity, by measuring the variation of $\lambda_b$ and using appropriate photo-thermo-elastic constants [27].
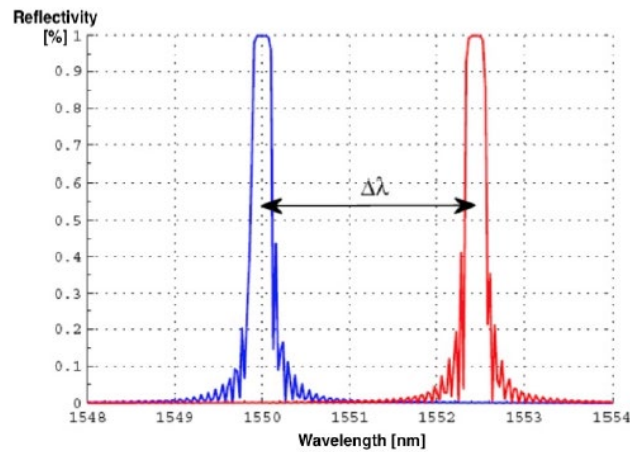
Figure 22 - Wavelength shifting

The main possible cases are:

- Uniform perturbation across the grid: the reflected spectrum shows a rigid translation. This is what happens with thermal and mechanical stresses. An example is shown in Figure 23 (a). In the case of traction, the peak shifts to the right, toward major $\lambda$, in the case of compression, instead, to the left.
- Linear perturbation: the resulting reflection spectrum is wider and with a lower peak value, as represented by Figure 23 (b)
- Arbitrary perturbation: the spectrum can undergo considerable deformations even with the splitting of the peak, Figure 23 (c) [27].
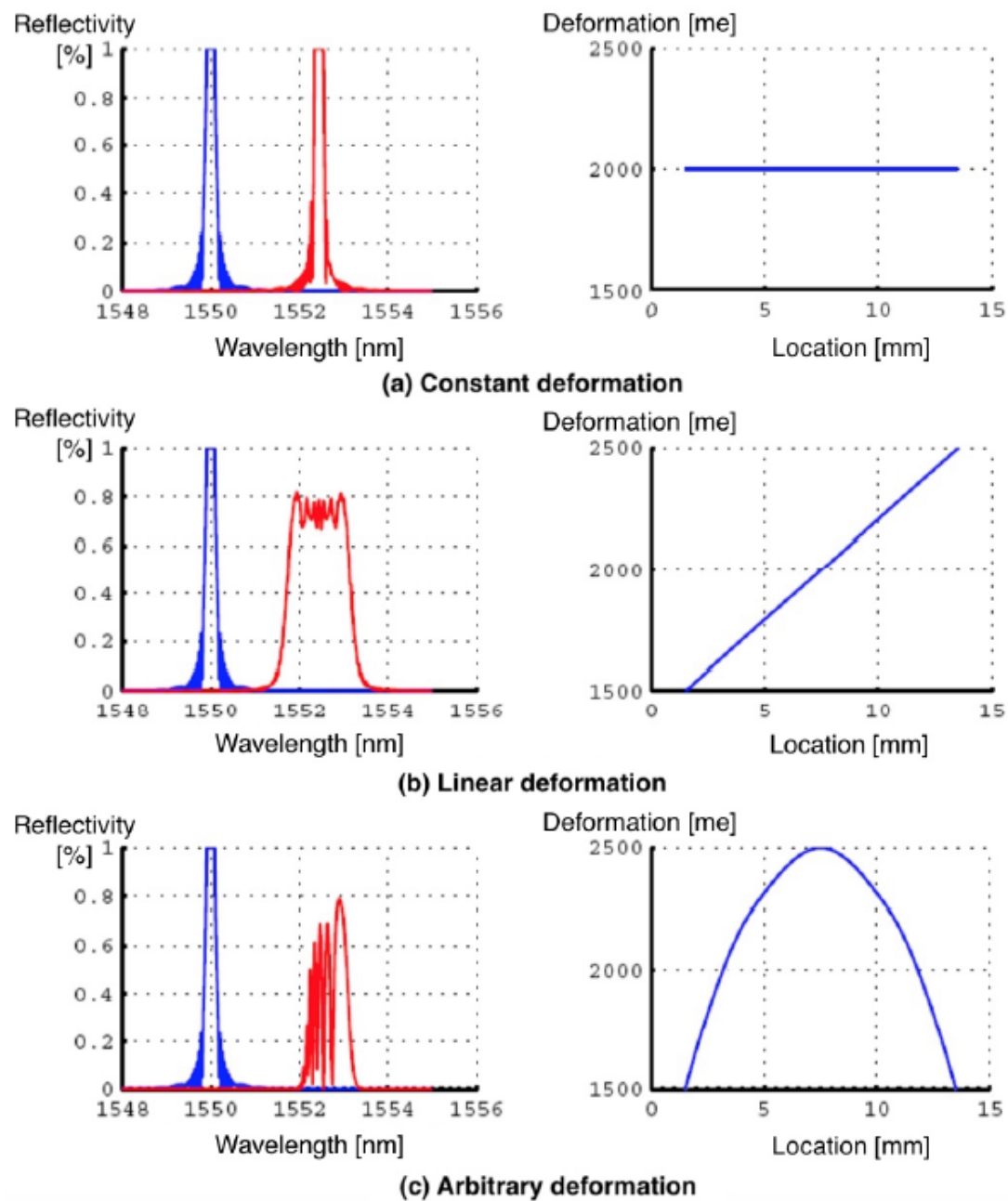
Figure 23 - Reflection spectrum related to different cases of deformation

It is possible to form different types of gratings, listed in Table 2.

| Type of grating | Grating structure | Spectra | Description |
|---|---|---|---|
| Uniform FBG | | | Characterized by periodic perturbation of the refractive index and works on the principle of Bragg's law. |

| | | | |
|---|---|---|---|
| Chirped FBG | | | The grating period changes linearly with the position causing broadly reflected spectra. |
| Long period grating | | | Core mode couples with co-propagating cladding mode causing resonance at transmission spectra. |
| Tilted FBG | | | Tilt in grating allows light to be coupled with cladding mode instead of core mode resulting in fine-comb resonance in transmission spectra. |
| Phase-Shifted FBG | | | A pi-phase discontinuity is presented in FBG forming a cavity by two FBG mirrors resulting in an extremely narrow notch in reflection spectra. |
| Superstructure FBG | | | Several FBGs are combined to form superstructure FBG whose transmission spectra consists of individual FBGs characteristic. |
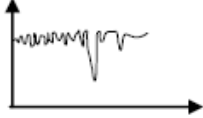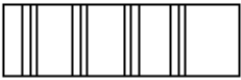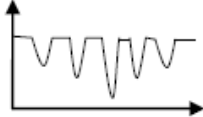
Table 2 - Grating types

To understand how the sensing mechanism of FBG takes place, consider an external parameter "$X$" also called the measured quantity, which may be temperature, strain, pressure, or humidity. The Bragg wavelength of FBG is dependent on this external parameter and can be calculated by differentiating the Bragg condition (Eq. 1.10):

$$\Delta\lambda_b = 2\frac{\partial(\Lambda n_{eff})}{\partial X}\Delta X = 2(\Lambda\frac{\partial n_{eff}}{\partial X} + n_{eff}\frac{\partial\Lambda}{\partial X})\Delta X$$

( 1.11 )

For example, if the sensor undergoes temperature perturbation and mechanical strain, the wavelength change will be:

$$\Delta\lambda_b = 2\left(\Lambda\frac{\partial n_{eff}}{\partial l} + n_{eff}\frac{\partial\Lambda}{\partial l}\right)\Delta l + 2\left(\Lambda\frac{\partial n_{eff}}{\partial T} + n_{eff}\frac{\partial\Lambda}{\partial T}\right)\Delta T$$

( 1.12 )

Which, after some manipulations, becomes:

$$\Delta\lambda_b = \lambda_b(1 - p_e)\varepsilon + \lambda_b\xi\Delta T = K_\varepsilon\varepsilon + K_T\Delta T$$

( 1.13 )

Where $\varepsilon$ is the axial strain, $\Delta T$ is the temperature change, $p_e$ is the photo-elastic constant, and $\zeta$ is the thermo-optical coefficient. In this way, it is possible to link physical measurements and wavelength shifting, but it is important to decouple the temperature and mechanical strain contribution to distinguish them, so a second sensor is needed:

$$\begin{pmatrix}\Delta\lambda_{b1}\\\Delta\lambda_{b2}\end{pmatrix} = \begin{bmatrix}K_{\varepsilon_1} & K_{T_1}\\K_{\varepsilon_2} & K_{T_2}\end{bmatrix}\begin{pmatrix}\varepsilon\\\Delta T\end{pmatrix}$$

( 1.14 )

Inverting the K-matrix it is possible to obtain the two separate contributions [28] [24].

In several applications, multiple sensors or an array of sensors are required to carry out measurements of either the same parameter at multiple places or multiple parameters located at different points of the structure. The sensors can be either surface-mounted or embedded in smart structures. For this purpose, multiplexing techniques are developed to achieve distributed sensing network. Many multiplexing techniques have been reported in studies such as Spatial-division multiplexing (SDM) and the more common Time-division multiplexing (TDM) and Wavelength-division multiplexing (WDM). The working principle of the TDM technique (Figure 24) consists of a time delay in the signals received by a processor. A light beam is emitted by a source in the fiber, where are placed some gratings with a certain distance between them. Every grating reflects part of the signal, which returns to the processor. The time between every returning signal gives information on the distance between gratings, which is related to deformations, linked to physical phenomena. This technique has a distance limitation because the processor needs the time to process the signal before the next one comes, so the gratings must have a minimum distance between each other $(20 - 30\ cm)$.
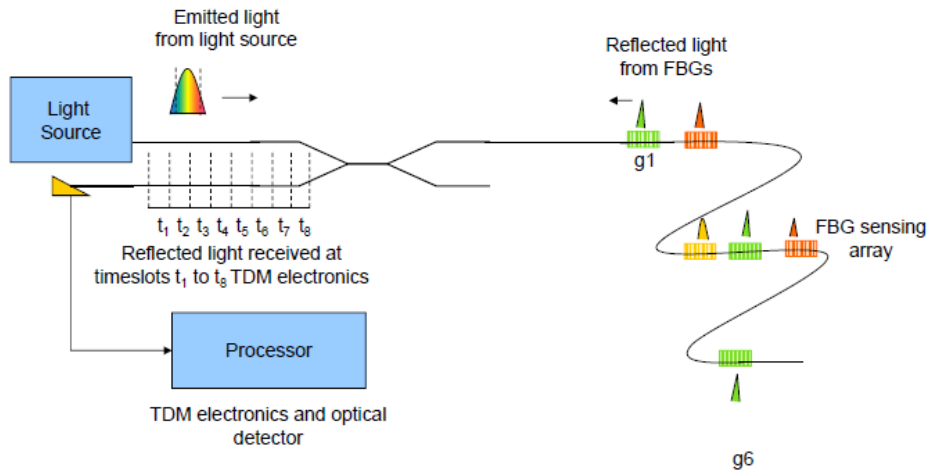
Figure 24 - TDM technique

In the WDM technique (Figure 25) the source emits a light beam with a complete spectrum and when it reaches the gratings, the beam is reflected with a certain wavelength, different for each grating in the fiber. So, each sensor will reflect a different peak, which corresponds to a different segment of the light spectrum. In this way, it is possible to recognize the sensor that corresponds to every peak and discover the deformation related to each point of the structure [28] [24].
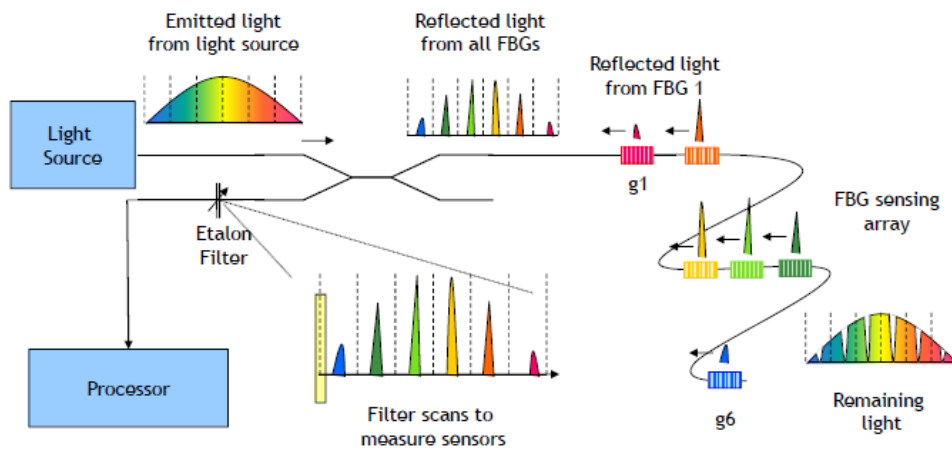


Figure 25 - WDM technique

## 1.4.2.2. FBG embedding

One of the main advantages of an SHM system is the sensor embedding directly inside the structure because it guarantees real-time monitoring of the components' health without compromising the aerodynamic properties of the structure. A necessary condition for developing Smart Structures is the development of embedding techniques that ensure the correct working of the sensors/actuators, preserve their characteristics, and maintain the invasivity below some acceptance bounds. The critical aspects of the FBG embedding process are characterized by three main problems: the presence of reinforcing fibers off-axis concerning the FO, the

incompatibility of standard coating with curing cycles, and the presence of FO exiting from the laminate.

## Presence of reinforcing fibers off-axis

It is important to avoid the sensor's shape distortions, which could compromise the correct working of the sensor. From this point of view, is crucial to avoid an excessive misalignment of the grating fringes that could bring signal losses. Both aspects are influenced by the lamination sequence of the host component. The presence of reinforcing fibers that are differently oriented compared to the optical fibers can cause different phenomena:

- Sensor deformations (Figure 26a) – the compression of reinforcing fibers presses the optical fiber and causes a misalignment of the grating fringes. This phenomenon causes an alteration in the signal spectrum, which results divided into two peaks (Figure 26b), and it does not give any useful information.
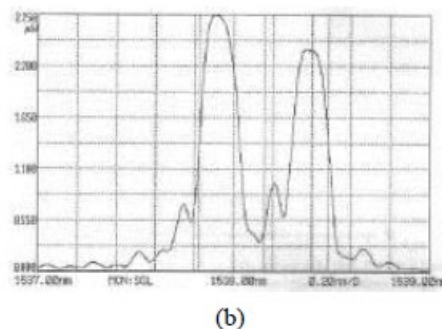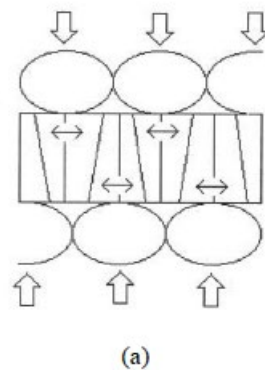


(a)



(b)

Figure 26 - (a) Sensor compression due to reinforcing fibers. (b) Signal spectrum division

- Signal attenuation (Figure 27) – the presence of reinforcing fiber can cause micro-bendings of the fiber optic, which produces an intensity reduction of the signal. This problem could be solved by increasing the signal intensity in such a way that the signal resists the attenuations.
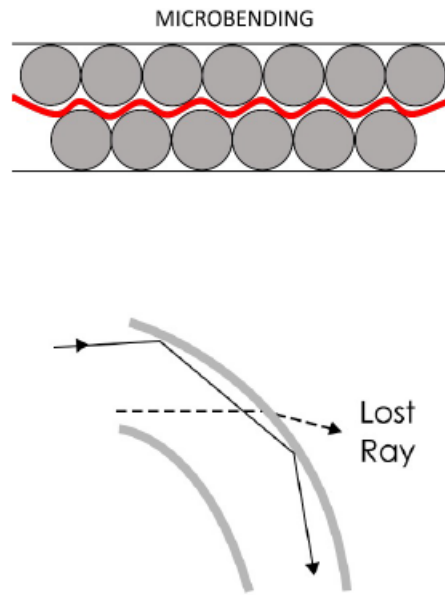
MICROBENDING

Lost
Ray

Figure 27 - Micro-bending of the sensor that causes signal losses.

- Defects birth inside the laminate (Figure 28) – the presence of the sensor could be invasive for the composite material, and a misalignment between FO and reinforce could cause a loss of the mechanical properties of the laminate because the reinforcing fibers exit from their plane to overtake the optical fibers. The presence of the fiber optic causes the birth of weak points in the laminate due to the presence of empty spaces, without resin (Figure 29).
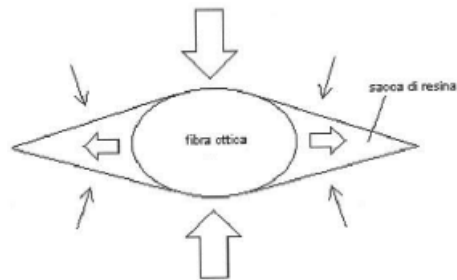
sacca di resina

fibra ottica

Figure 28 - Reinforcing fibers deviation due to the presence of FO
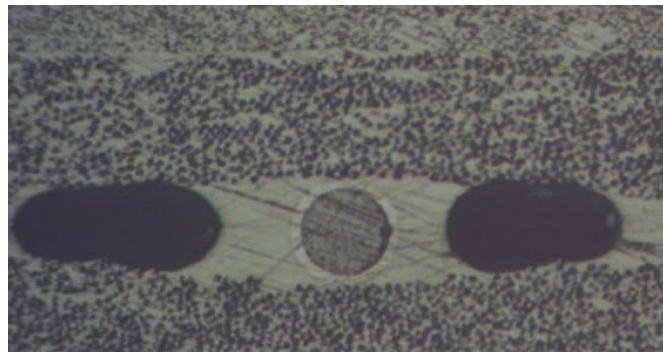
Figure 29 - Voids due to the absence of the resin

The less dangerous embedding condition is a unidirectional laminate with reinforcing fibers and optical ones oriented in the same direction. However, this solution goes in contrast with the most important peculiarity of composite materials, which can project ad hoc sequences of the laminates to maximize the structural efficiency of the component. So, the adopted solutions are different and consist of the use of a thicker and more resistant coating to avoid optical fiber compression. Reinforcing fibers can move a little bit to accommodate the FO into the layer. Another solution is the possibility to use elastomeric pads and Glass Fiber Reinforcing Panels (GFRP) to create a protective layer for the sensor into the laminate. This solution guarantees protection for the FBG but creates an additional thickness to the laminate.

## Incompatibility of standard coating with the curing cycle

A crucial aspect of the embedding process is the need to preserve the polymeric coating integrity, which is a necessary condition for the load's transmission from the host material to the sensor. Standard FO sensors have an acrylic coating, which has a glass transition temperature of about $86°C$ and when the laminate undergoes a curing cycle, the coating gets poor mechanical properties, becomes soft, and can be deformed when the host material is compressed. The load transfer capability is guaranteed only in absence of any coating deformation, so the adopted solution is to use poly-imide coatings, which can tolerate higher temperatures without any excessive deformation since they have a $T_g$ of about $187°C$.

## Presence of FO exiting from the laminate

A last important aspect is the protection and connection of the FO exiting from the laminate. In this type of sensor, the fiber itself connects the FBG with the outside, the point where the fiber exits the laminate is a discontinuity point which creates stress concentration. Moreover, the resin of the host material, during the curing cycle, is highly fluid and tends to climb back to the fiber due to a capillarity phenomenon. The reticulation of such resin causes the birth of dangerous compression stress states. The solution is to adopt a PTFE pipe embedded in the laminate for 10mm and which is extended since the fiber reaches the optical connector. The penetration of the resin into the fiber is obstructed by a bubble of epoxy resin [29] [30].
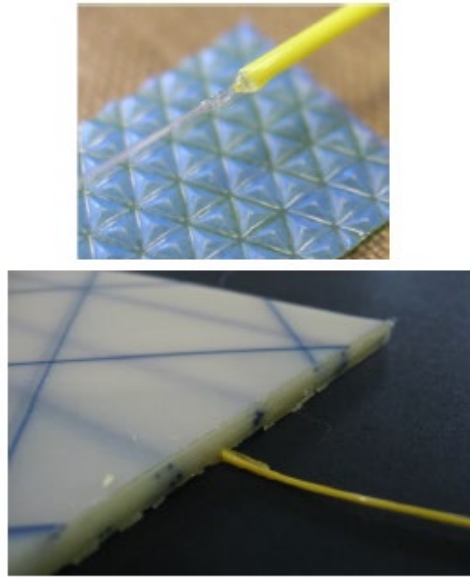
Figure 30 - PTFE tubes and epoxy resin

## 1.4.2.3. FBG as humidity sensor

As presented in Section 1.4.2.1, an FBG is formed by photoinduced refractive index modulation in the core of a single-mode fiber. The structure formed within the fiber behaves like a notch filter, which reflects the light signal at a wavelength termed the Bragg wavelength ($\lambda_B$) that satisfies the Bragg condition. The value of $\lambda_B$ is dependent on the effective refractive index ($n_{eff}$) of the optical fiber and the grating pitch ($\Lambda$) of the FBG and is given by:

$$\lambda_b = 2n_{eff}\,\Lambda$$

( 1.15 )

Where both the refractive index and the grating pitch can be affected by strain and temperature. As such, FBGs are very popular in temperature and strain-sensing applications. The shift in Bragg wavelength due to the change in strain or thermal effect is given by:

$$\frac{\Delta\lambda_B}{\lambda_B} = (1 - p_e)\varepsilon + \xi\Delta T$$

( 1.16 )

The FBG sensors could be used to detect moisture absorption because the coatings, such as polyimide, contain hydrophilic groups that can interact with water molecules to form hydrogen bonds. The polar groups on the surface of the polyimide film adsorb water molecules in a humid environment and the quantity of absorbed water as well as the free volume inside the coating will increase with the increase of relative humidity ($RH$). The relative humidity parameter is defined as the ratio between the

partial pressure of the water vapor ($P_w$) and the saturation water vapor pressure ($P_{ws}$), as shown by the expression below:

$$RH = \frac{P_w}{P_{ws}} * 100$$

So, the polymeric film undergoes a linear expansion phenomenon. If the humidity in the measured environment changes, the coating layer will be deformed. The coating will transmit its deformation to the FBG which will be translated into a wavelength shift. Moreover, for an FBG sensor partially bonded on a host structure, the mismatch of the thermal expansion coefficient between the optical fiber and the host structure induces a thermal strain. In order to report the effect of the temperature and humidity of the coating on the core, the mixture law must be applied. According to the congruence equations and CLT (Classical Lamination Theory) must be true that:

$$\begin{cases} \varepsilon = \varepsilon_c = \varepsilon_f \\ F_{tot} = F_c + F_f \end{cases}$$

$$\rightarrow \sigma_{tot} = V_c E_c + V_f E_f \rightarrow E_{tot}\varepsilon_{tot} = V_c E_c \varepsilon_c + V_f E_f \varepsilon_f \rightarrow E_{tot} = V_c E_c + V_f E_f$$

( 1.17 )

Calling $F_{tot}$ the external force acting on the system, which is subjected to thermal and moisture effects (no mechanical stresses applied), the total deformation $\varepsilon$ will be:

$$F_{tot} = E_{tot}A_{tot}\varepsilon \rightarrow \varepsilon = \frac{F_{tot}}{A_c E_c + A_f E_f}$$

$$F_{tot} = F_c + F_f = A_c E_c \beta_c \Delta RH + A_c E_c \alpha_c \Delta T + A_f E_f \beta_f \Delta RH + A_f E_f \alpha_f \Delta T$$

( 1.18 )

Therefore, adding a mechanical strain, the axial strain of the polyimide coated FBG can be divided into three contributions:

$$\varepsilon = \frac{F_{tot}}{A_{tot}E_{tot}} = \frac{A_c E_c \beta_c + A_f E_f \beta_f}{A_c E_c + A_f E_f}\Delta RH + \frac{A_c E_c \alpha_c + A_f E_f \alpha_f}{A_c E_c + A_f E_f}\Delta T + \varepsilon_M = \varepsilon_{RH} + \varepsilon_T + \varepsilon_M$$

( 1.19 )

Where $\varepsilon_{RH}$ represents the strain caused by humidity changes, $\varepsilon_T$ stands for strain due to temperature changes, and $\varepsilon_M$ is the mechanical strain due to external loads. The core is made of glass, so it is not sensitive to moisture, so $\beta_f = 0$. The strain induced by moisture and temperature can be expressed as a function of, respectively, $\Delta RH$ and $\Delta T$:

$$\varepsilon_{RH} = \frac{E_c A_c}{E_c A_c + E_f A_f}\beta_c \Delta RH$$

( 1.20 )

$$\varepsilon_T = \frac{E_c A_c \alpha_c + E_f A_f \alpha_f}{E_c A_c + E_f A_f}\Delta T$$

( 1.21 )

Where $E$ is the Young's modulus, $A$ the cross-sectional areas, $\alpha$ the coefficient of thermal expansion, and $\beta_c$ the constant coefficient of hygroscopic expansion of the polymer. The subscript c stands for the coating, while $f$ stands for the bare fiber.

Substituting ( 1.20 ) and ( 1.21 ) in ( 1.19 ) and then in ( 1.16 ), it is possible to obtain:

$$\frac{\Delta\lambda_B}{\lambda_B} = (1 - p_e)\varepsilon_M + (1 - p_e)\frac{E_c A_c}{E_c A_c + E_f A_f}\beta_c\Delta RH + \left\{(1 - p_e)\frac{E_c A_c \alpha_c + E_f A_f \alpha_f}{E_c A_c + E_f A_f} + \xi\right\}\Delta T$$

( 1.22 )

The response is a linear superimposition of mechanical strains, RH, and T effects. In the presence of variations in relative humidity, $\Delta RH$, and temperature, $\Delta T$, the relative Bragg wavelength shift $\frac{\Delta\lambda_B}{\lambda_B}$ is therefore given by:

$$\frac{\Delta\lambda_B}{\lambda_B} = S_{RH}\Delta RH + S_T\Delta T + S_M\varepsilon_M$$

( 1.23 )

Where $S_{RH}$, $S_T$, and $S_M$ are the sensor sensitivities to relative humidity, temperature, and mechanical strains, respectively, expressed in Equation ( 1.22 ).

In the following, a way to decouple temperature and humidity measurements is presented, for the aim of simplicity, a zero mechanical strain case is considered.

In the equation above, $S_T$ and $S_{RH}$ are known since the material and fiber properties are known, so there are only two unknown variables: $\Delta T$ and $\Delta RH$. The way chosen to solve this problem consists of using two different FBG sensors with different properties, obtaining:

$$\begin{pmatrix} \dfrac{\Delta\lambda_{B_1}}{\lambda_{B1}} \\ \dfrac{\Delta\lambda_{B_2}}{\lambda_{B2}} \end{pmatrix} = \begin{bmatrix} S_{T_1} & S_{RH_1} \\ S_{T_2} & S_{RH_2} \end{bmatrix}\begin{pmatrix} \Delta T \\ \Delta RH \end{pmatrix}$$

( 1.24 )

Under the hypothesis of $S_{RH_2}S_{T_1} - S_{RH_1}S_{T_2} \neq 0$, it is possible to invert ( 1.24 ) to obtain the desired variables:

$$\begin{pmatrix} \Delta T \\ \Delta RH \end{pmatrix} = \frac{1}{S_{RH_2}S_{T_1} - S_{RH_1}S_{T2}}\begin{bmatrix} S_{RH_2} & -S_{RH_1} \\ -S_{T_2} & S_{T_1} \end{bmatrix}\begin{pmatrix} \dfrac{\Delta\lambda_{B_1}}{\lambda_{B1}} \\ \dfrac{\Delta\lambda_{B_2}}{\lambda_{B2}} \end{pmatrix}$$

( 1.25 )

Since the temperature may change in the process of humidity measurement, the Bragg wavelength variation of the polyimide coated FBG caused by temperature fluctuation

should be eliminated. This can be easily solved by using the second sensor with a coating that is not humidity sensitive, which in the following will be called bare-FBG $(B - FBG)$. So $S_{RH_2} = 0$, and ( 1.25 ) can be rewritten as follows:

$$
\begin{pmatrix} \Delta T \\ \Delta RH \end{pmatrix} = \frac{1}{S_{RH_1} S_{T2}} \begin{bmatrix} 0 & S_{RH1} \\ S_{T2} & -S_{T1} \end{bmatrix} \begin{pmatrix} \dfrac{\Delta \lambda_{B1}}{\lambda_{B1}} \\ \dfrac{\Delta \lambda_{B2}}{\lambda_{B2}} \end{pmatrix}
$$

( 1.26 )

The ( 1.26 ) can be easily solved to obtain the relative humidity variation ΔRH [31] [32] [33] [34] [35] [36].

### 1.4.2.4. Equation of FBG embedded in a host material

When the fiber is embedded in a host material, such as epoxy resin, the equations presented in Section 1.4.2.3 change. If perfect strain transfer between the embedded FBG sensor and the host material is assumed, the ( 1.17 ) will be:

$$
\begin{cases} \varepsilon = \varepsilon_c = \varepsilon_f = \varepsilon_h \\ F_{tot} = F_c + F_f + F_h \end{cases}
$$

$$
\rightarrow \sigma_{tot} = V_c E_c + V_f E_f + V_h E_h \rightarrow E_{tot} \varepsilon_{tot} = V_c E_c \varepsilon_c + V_f E_f \varepsilon_f + V_h E_h \varepsilon_h
$$

$$
\rightarrow E_{tot} = V_c E_c + V_f E_f + V_h E_h
$$

( 1.27 )

Therefore:

$$
\varepsilon = \frac{F_{tot}}{A_c E_c + A_f E_f + A_h E_h}
$$

( 1.28 )

Where

$$
F_{tot} = F_c + F_f + F_h =
$$
$$
= A_c E_c \beta_c \Delta RH + A_c E_c \alpha_c \Delta T + A_f E_f \alpha_f \Delta T + A_h E_h \beta_h \Delta RH + A_h E_h \alpha_h \Delta T
$$

( 1.29 )

Substituting in ( 1.28 ) and adding a mechanical strain, it is possible to obtain:

$$
\varepsilon = \frac{F_{tot}}{A_{tot} E_{tot}} = \frac{A_c E_c \beta_c + A_h E_h \beta_h}{A_c E_c + A_f E_f + A_h E_h} \Delta RH + \frac{A_c E_c \alpha_c + A_f E_f \alpha_f + A_h E_h \alpha_h}{A_c E_c + A_f E_f + A_h E_h} \Delta T + \varepsilon_M
$$

( 1.30 )

Considering that the cross-sectional area of the host material is considerably bigger than the core and coating ones, $A_c E_c \beta_c \ll A_h E_h \beta_h$ and $A_c E_c \alpha_c, A_f E_f \alpha_f \ll A_h E_h \alpha_h$, this brings to:

$$\varepsilon = \frac{F_{tot}}{A_{tot}E_{tot}} = \frac{A_h E_h \beta_h}{A_c E_c + A_f E_f + A_h E_h}\Delta RH + \frac{A_h E_h \alpha_h}{A_c E_c + A_f E_f + A_h E_h}\Delta T + \varepsilon_M$$

( 1.31 )

Thus:

$$\frac{\Delta \lambda_B}{\lambda_B} = (1 - p_e)\frac{E_h A_h}{E_c A_c + E_f A_f + E_h A_h}\beta_h \Delta RH + \left\{(1 - p_e)\frac{E_h A_h \alpha_h}{E_c A_c + E_f A_f + E_h A_h} + \xi\right\}\Delta T$$

( 1.32 )

### 1.4.2.5. Alternative formulation

A series of equations linking wavelength variations of fiber Bragg grating sensors to changes in temperature, mechanical strain, and relative humidity were introduced in the previous section. These equations might also be expressed by taking into account the factors that result from changes in the refractive index and the pitch of the gratings, considering the first one dependent on stresses rather than strains. The relative wavelength variation can be expressed as follows:

$$\frac{\Delta \lambda_B}{\lambda_B} = \varepsilon + \xi \Delta T - p_e(\varepsilon_r + \varepsilon_M)$$

( 1.33 )

Here, $\varepsilon$ stands for the actual strain that the core experiences, which can be the result of a combination of mechanical, thermal, and moisture effects that implicate a change in the grating pitch's length. $\varepsilon_r$ is the fictitious strain applied on the fiber core due to the residual stress. In other words, it is the strain that the core "would" assume minus the strain that the core actually assumes. In mathematical terms:

$$\varepsilon_r = \varepsilon_M + \alpha_f \Delta T - \varepsilon =$$
$$= \varepsilon_M + \alpha_f \Delta T$$
$$- \left[\frac{A_h E_h \beta_h}{A_c E_c + A_f E_f + A_h E_h}\Delta RH + \frac{A_h E_h \alpha_h}{A_c E_c + A_f E_f + A_h E_h}\Delta T + \varepsilon_M\right]$$
$$= \alpha_f \Delta T - \frac{A_h E_h \beta_h}{A_c E_c + A_f E_f + A_h E_h}\Delta RH - \frac{A_h E_h \alpha_h}{A_c E_c + A_f E_f + A_h E_h}\Delta T$$

( 1.34 )

Therefore, ( 1.33 ) becomes:

$$\frac{\Delta \lambda_B}{\lambda_B} = (1 - p_e)\varepsilon_M + (1 + p_e)\frac{A_h E_h \beta_h}{A_c E_c + A_f E_f + A_h E_h}\Delta RH$$
$$+ \left[(1 + p_e)\frac{A_h E_h \alpha_h}{A_c E_c + A_f E_f + A_h E_h} + \xi - p_e \alpha_f\right]\Delta T$$

( 1.35 )

Equation ( 1.35 ) can be rewritten as:

$$\frac{\Delta\lambda_B}{\lambda_B} = \varepsilon_M + \frac{A_h E_h \beta_h}{A_c E_c + A_f E_f + A_h E_h}\Delta RH + \frac{A_h E_h \alpha_h}{A_c E_c + A_f E_f + A_h E_h}\Delta T$$
$$+\xi\Delta T$$
$$-p_e\left\{\varepsilon_M + \alpha_f\Delta T - \frac{A_h E_h \beta_h}{A_c E_c + A_f E_f + A_h E_h}\Delta RH - \frac{A_h E_h \alpha_h}{A_c E_c + A_f E_f + A_h E_h}\Delta T\right\}$$

$$( 1.36 )$$

Where the first line of the equation above denotes the actual stress applied on the fiber core, which implies an effective enlargement of the grating pitch $\Lambda$; the second line represents the change of the refractive index $n_{eff}$ due to the temperature variations; the third line is the change of $n_{eff}$ due to the stress present inside the core, which induces a photo-elastic phenomenon.

Equation ( 1.35 ) presents differences from ( 1.32 ) because the photo-elastic phenomenon is considered related to the stresses in the core and not anymore to the strains [37].
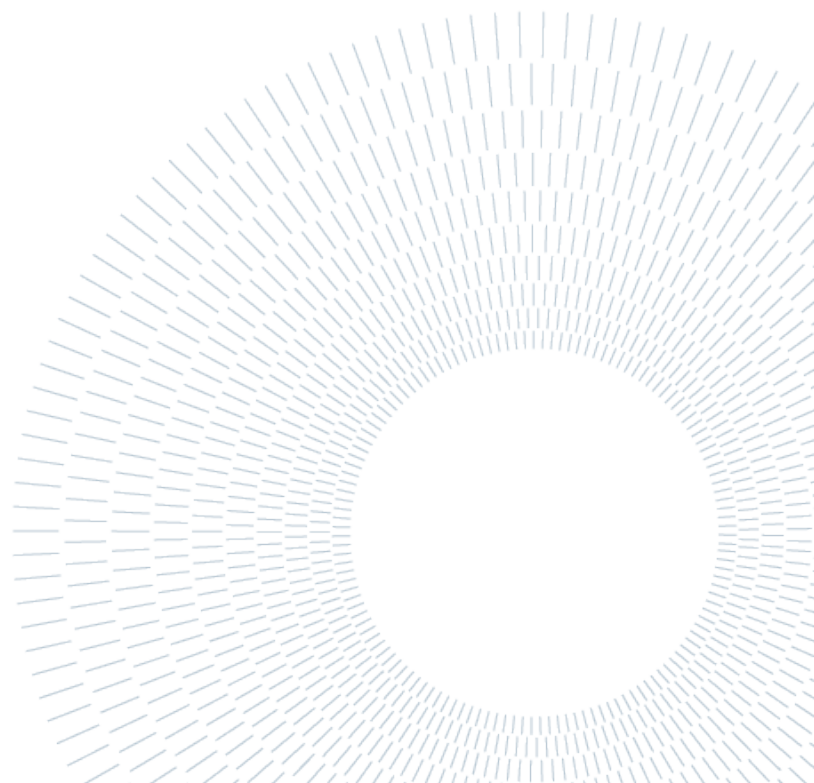
# 2 Manufacturing

The purpose of this thesis work is to characterize the mechanical properties of Epoxy resin specimens before and after conditioning them in a hot water tank to stimulate exposure to high temperatures and moisture over time. Before proceeding with the test phase, it was necessary to produce the specimens following the ASTD D638 norm. Section 2.1 provides an overview of the material, Section 2.2 describes the production procedure of the mold used to obtain the specimens' shape requested by ASTD D638. In Sections 2.3 and 2.4, an introduction to the different specimens produced is presented, while Section 3.2.1 reports the analysis of the residual strains made during the manufacturing process through FBG sensors embedded in the specimens.

## 2.1. Epoxy Resin

The work presented in this thesis focuses only on the matrix phase the composite materials are made of, in particular on a specific epoxy resin used in automotive and aeronautical applications. Epoxy resin is a type of thermosetting polymer that is formed by mixing two components: a resin, and a hardener. When the two components are mixed, a chemical reaction occurs and causes the resin to cure and harden into a strong, durable material. Epoxy resin is often used as a coating or adhesive because of its excellent bonding properties and resistance to water, chemicals, and heat. It is an epoxy matrix system developed for structural and aesthetic applications, suitable for the manufacturing of sporting goods and industrial uses. Epoxy resin is commonly used as the matrix material in composites because its excellent adhesive properties allow it to bond well with the reinforcing fibers. It also has a low viscosity, which means it can easily flow and wet out the fibers, resulting in a more uniform distribution of the resin throughout the composite structure. One of the key advantages of epoxy resin is its ability to provide excellent mechanical properties, such as high strength, stiffness, and toughness, making them ideal for use in a wide range of applications, from aerospace to automotive components, to sporting goods and marine structures.

However, it's important to note that the mechanical properties of the composite made with epoxy resin can be highly dependent on the quality of the manufacturing process. Proper curing of the resin, the use of appropriate fiber types and orientation, and careful attention to manufacturing details can all play a critical role in determining the final properties of the composite structure.

The resin code is EP10ST, and it can be cured in an autoclave, vacuum bag, and hot mold processes, in a temperature range between 90 and 150°C. The resin is compatible with all commercially available reinforcing materials such as fiberglass, carbon fiber, or Kevlar and with all reinforcing types such as fabrics, UD tapes, and non-woven.

## Uncured matrix properties

Dynamic thermal properties by DSC analysis, following ISO 11357–5 regulations are:

- $T_{onset} = 135 - 138°C$
- $T_{peak} = 145 - 147°C$
-

## Viscosity profile

The viscosity of the epoxy resin is a measure of its thickness or resistance to flow. It is an important characteristic that affects the manufacturing process of composite materials. This characteristic can vary widely depending on the specific formulation, temperature, and curing conditions. The following figure shows the variation of viscosity with the increase in temperature, as reported by the technical data sheet of the material.
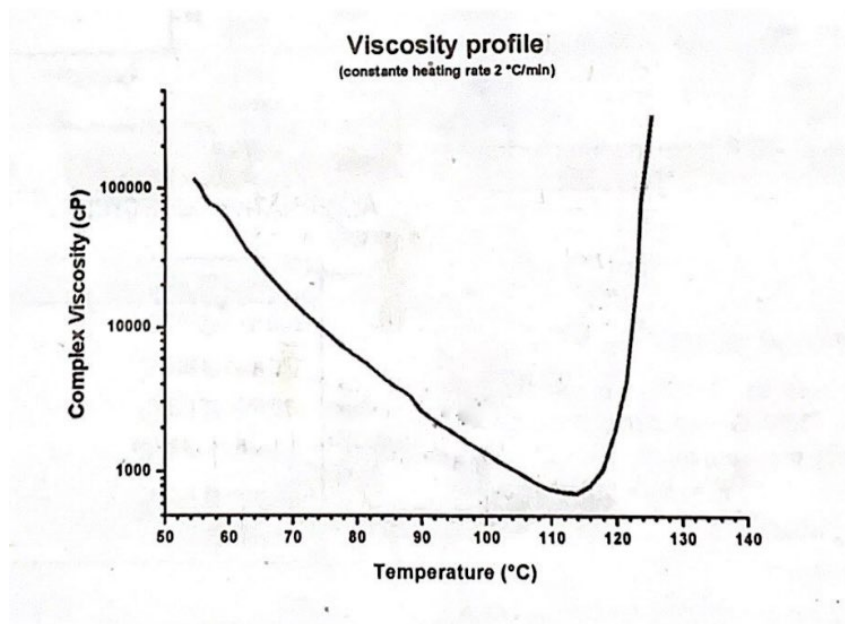


Figure 31 - Viscosity profile of EP10ST resin

## Gel time curve

The gel time is the time it takes for the resin to change from a liquid state to a solid or gel state during the curing process. It is an important parameter that affects the handling, processing, and ultimate properties of the cured epoxy and it can be

influenced by several factors, such as the type and amount of curing agent used, the viscosity of the resin, and the temperature.

Some values of gel time at relevant temperatures are:

- Gel time @ 100°C: 25 minutes
- Gel time @ 120°C: 7 minutes
- Gel time @ 150°C: 1.5 minutes

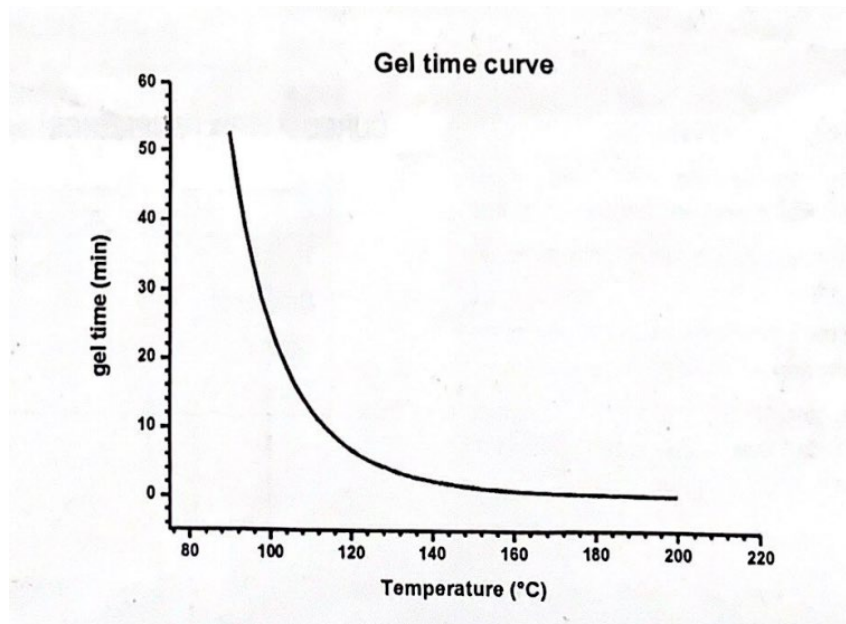The trend of gel time over the temperature is presented in Figure 32.



Figure 32 - Gel time curve of EP10ST resin

## Casting and curing process

The material, in environmental conditions, presents a solid state and it is necessary to develop a procedure to make the material suitable for the casting process in the mold. The process includes a heat procedure to make the material liquid and a degassing process to eliminate all the air bubbles in the material which could produce voids and imperfections that could influence moisture absorption.

The procedure selected consists of three different phases:

1. Heat the resin (and the mold) to 90°C and maintain it in the oven for 25 minutes.
2. Perform a degassing process in the vacuum oven, at 90°C for 25 minutes.
3. Bring the resin (and the mold) to 120°C and perform the casting process in the mold using a syringe.
4. Leave the resin in the mold for one hour at 120°C to obtain a complete curing process.

## 2.2.   Production of the mold

Having to carry out tests on resin-only specimens, it was decided to follow the ASTM D638 Standard regulation (Standard Test Method for Tensile Properties of Plastics), which requires the use of dog-bone shape specimens. Following the regulations, it was selected a Type I specimen, whose dimensions are shown in Figure 33 and Table 3.

To obtain these specimens, it was created a silicone rubber mold (Figure 34) using plastic specimens, with a geometry referable to the ASTM D638 (Type I) standard. A thin incision with a depth of 1.5mm was made on the borders of the mold in order to position and fix the optical fiber in the proper way. The exiting fibers were fixed using a metal bar properly screwed on a metallic plate, where the mold was placed.

The material used to produce the mold was silicone rubber GLS-50, the solidification process was ensured by adding a 5% volume of catalyst (T-30).
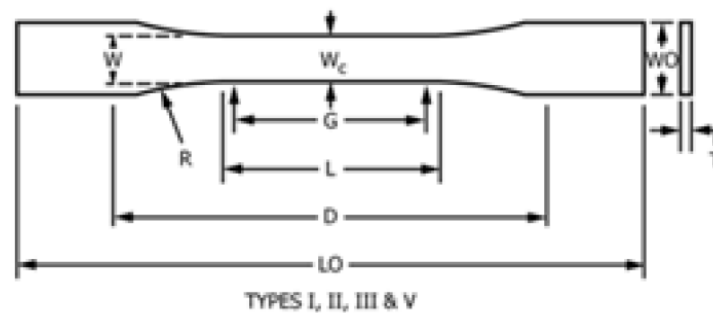


Figure 33 - Dog-Bone specimen following ASTM D638

| | |
|---|---|
| W – Width of the narrow section | 13$mm$ (±0.50) |
| L – Length of the narrow section | 57$mm$ (±2.25) |
| WO – Width overall, min | 19$mm$ (±0.75) |
| LO – Length overall, min | 165$mm$ (±6.50) |
| G – Gage length | 50$mm$ (±2.00) |
| D – Distance between grips | 115$mm$ (±4.50) |
| R – Radius of fillet | 76$mm$ (±3.00) |
| T – Thickness, max | 7$mm$ (±0.28) |

Table 3 - Specimen dimensions
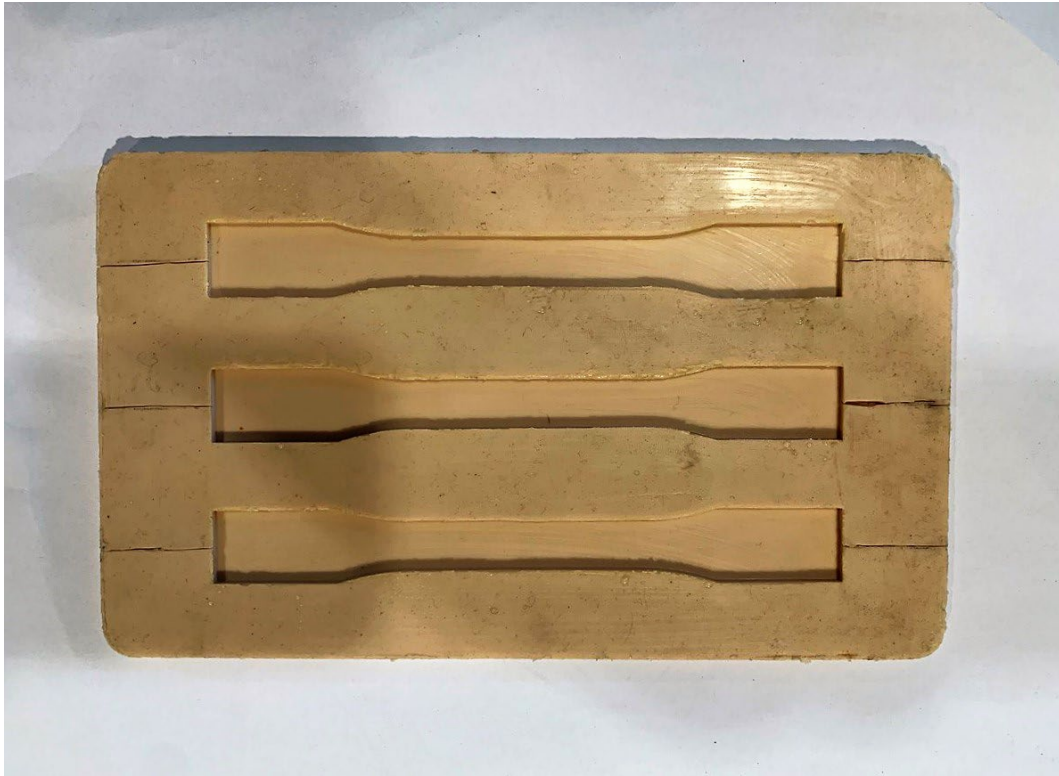
Figure 34 - Silicone rubber mold

## 2.3. Production of the non-sensorized specimens

To become familiar with the resin curing and casting process, a preliminary activity phase was planned. The primary objective of this activity was to produce uniform specimens with centered and stretched fibers. To achieve this goal, non-sensorized fibers were embedded in the resin.

The first issue encountered during this phase was the identification of an appropriate resin treatment procedure. It was necessary to reduce the resin's viscosity and perform a degassing process to eliminate any air bubbles that may be present in the material. The timing was crucial in this phase since the resin could begin its polymerization process if exposed to high temperatures. After conducting several tests, the following procedure was settled on:

- Heat the resin in the oven at 90°C for 25 minutes.

- Place the resin in the vacuum ovens at 90°C for 25 minutes, performing the degassing process every 2-3 minutes.

- Heat the resin again in the oven at 115°C for 10 minutes to reduce its viscosity.

- Cast the resin in the mold using a syringe.

- Cure the resin in the oven at 120°C for 60 minutes.

- Allow the specimen to cool.

By following this procedure, specimens with a uniform distribution of the resin can be obtained while minimizing the presence of air bubbles and defects.

The second essential aspect of the activity was determining how to secure the fibers at the center of the specimen's width and thickness and stretch them to obtain accurate measurements when using real sensorized fibers. To accomplish this, the mold was positioned on a metal plate, and two metallic bars were fastened onto it. A rubber pad was utilized to prevent excessive pressure on the fibers from the bars. The arrangement of the mold is illustrated in Figure 35.
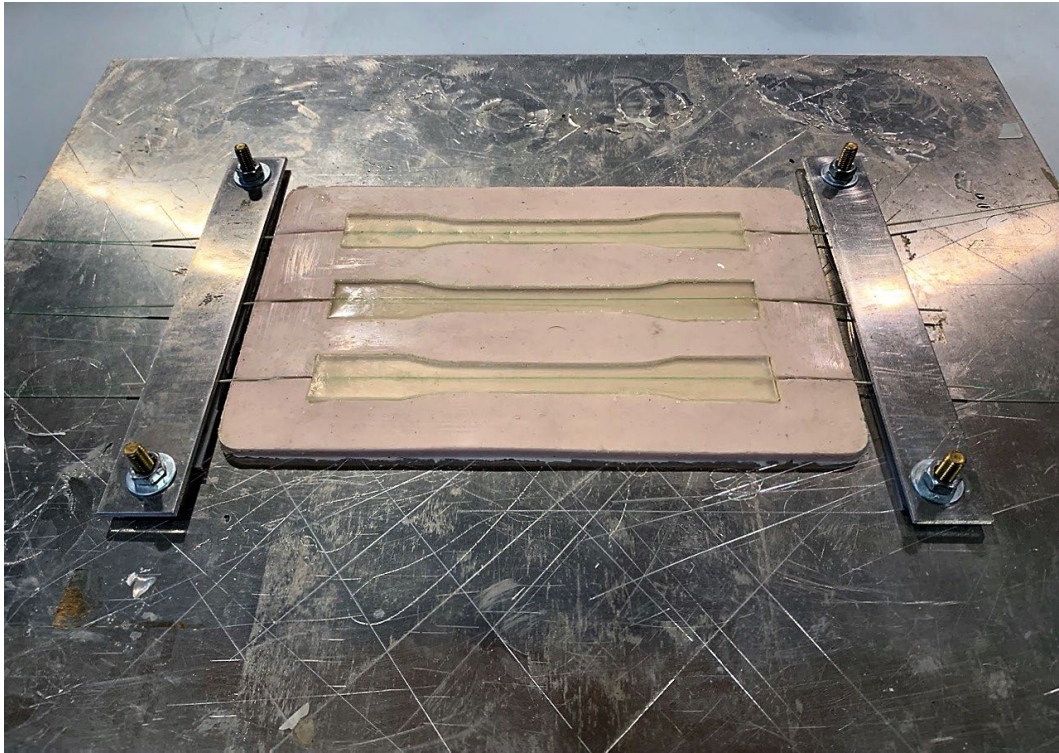
Figure 35 - Specimen production set.

Using this method, a set of 20 specimens was produced, and a series of tests were conducted on them as detailed in Section 3.1. Figure 36 displays some examples of the specimens that were obtained.
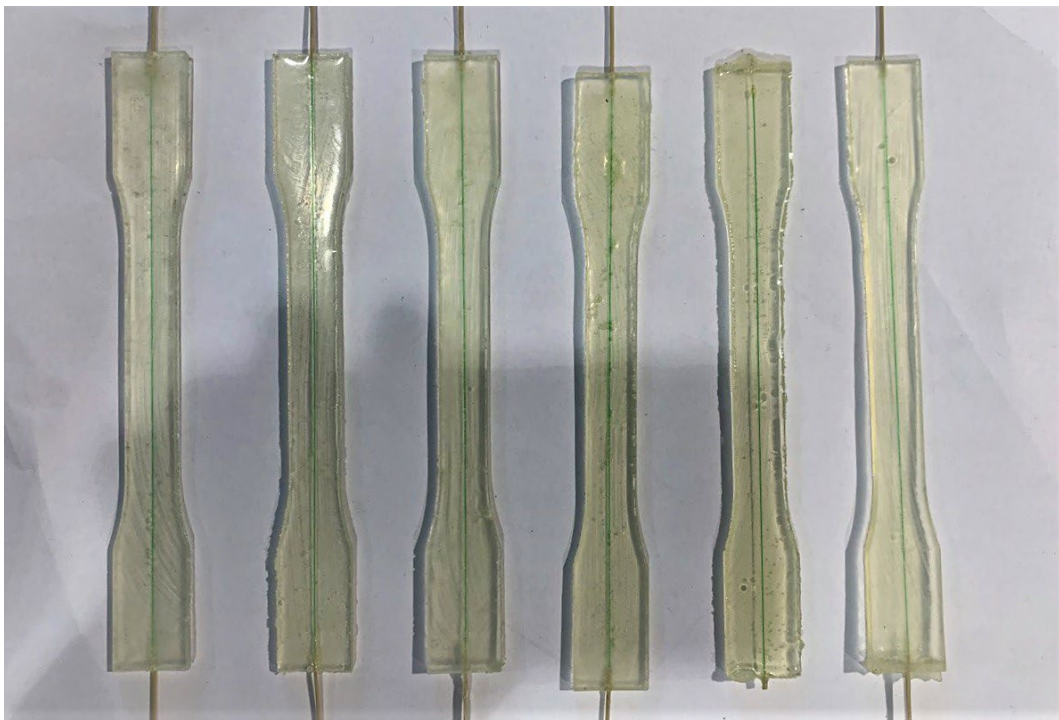


Figure 36 - Not-Sensorized specimens

## 2.4. Production of the sensorized specimens

After becoming acquainted with the production of the specimens, it was feasible to proceed with the creation of sensorized specimens by embedding real FBG sensors. Because of the high cost of the sensors, it was necessary to produce them in a single attempt. Two sensitized specimens were successfully created, and a third specimen without any embedded fibers was produced as a reference point.

FBG6466 and FBG6463 were the sensors utilized for this purpose and they were two uniform apodized Femto Second Gratings (FSGs) in Single Mode Fiber (SMF). An FSG is a type of optical grating, which is a periodic structure in the refractive index of an optical fiber. It is called a Femto Second Grating because it is typically inscribed in the fiber using ultrafast laser pulses that are in the femtosecond ($10^{-15}s$) time scale. A uniform apodized FSG in a single-mode fiber refers to an FSG that has a uniform refractive index modulation along its length and is "apodized", meaning that the refractive index modulation is tapered at both ends. The tapering helps to reduce unwanted reflection and scattering of light at the ends of the grating. A single-mode fiber is a type of optical fiber that has a very small diameter and is designed to transmit only a single mode of light.

The nominal Bragg's wavelength measured are:

- FBG6466: $\lambda_B = 1583\ [nm]$
- FBG6463: $\lambda_B = 1529\ [nm]$

They were both coated with polyimide material, which is commonly used in fiber optic sensors due to its excellent mechanical, thermal, and chemical properties. These coatings are known to exhibit hydrophilic behavior, meaning that they can absorb moisture from the surrounding environment. This property enables the coating to deform when exposed to moisture and it transfers the strains to the core, which is impermeable to humidity. In this way, the strains caused by moisture absorption may be identified.

With these sensors, monitoring of the manufacturing process of these specimens was done, and the results are described in Section 3.2.1. The specimens obtained were conditioned in a hot water tank to monitor moisture absorption, as it is possible to see in Section 3.2.2. After the conditioning cycle, a tensile test campaign was done, as shown in Section 3.2.3.

# 3 Experimental Phase

Once the fabrication of the specimens was finished, the experimental phase began. The numerous tests conducted to evaluate the residual strains caused by the manufacturing process, moisture absorption, and drying process are described in this chapter. These experiments aimed to track modification in the mechanical properties of specimens made exclusively of resin. This study can be extended by conducting additional tests on composite material specimens, in which the matrix phase is identical. This enables us to obtain specific indications regarding the moisture absorption capacity of the chosen resin, as well as that of the two-phase composites. From these two properties, we can also gather information about the behavior of the fiber phase alone.

To provide a set of data that could be compared to the outcomes acquired with the FBG sensors, the non-sensorized specimens were tested in the early stages of the experimental phase. The following tests were run on non-sensorized specimens:

- Tensile tests on dry specimens

- Conditioning of specimens in a water tank

- Tensile tests on wet specimens

- Drying process on wet specimens

- Tensile tests on dried specimens

Sensorized specimens were then taken into consideration. They were conditioned in a hot-wet environment by immersing them in a water tank for an extended period of time. Throughout this period, the strains of the optical fiber generated by the hygrothermal effects were constantly monitored using an optical interrogator, which enabled us to evaluate the variation in terms of wavelength reflected by the grating.

## 3.1. Not-Sensorized specimens

The dimensions and characteristics of the initial set of specimens are presented in Table 4. Each specimen is named according to the date of its production and its location in the mold, denoted by letters A, B, or C. The first group of specimens underwent a dry tensile test campaign, and the results are reported in Section 3.1.1. Meanwhile, the second group of specimens was subjected to a hot water tank conditioning to observe their moisture absorption behavior.

| | Name | Central Section $[mm^2]$ | Volume $[mm^3]$ | Mass $[g]$ | Density |
|---|---|---|---|---|---|
| DRY TENSILE TESTS | 25.10.A | 34,565 | 7651,621 | 9,010 | 1,178 |
| | 25.10.B | 39,470 | 8587,354 | 9,570 | 1,114 |
| | 3.11.A | 36,891 | 7999,808 | 9,240 | 1,155 |
| | 4.11.A | 37,356 | 8038,590 | 9,400 | 1,169 |
| | 7.11.B | 47,984 | 10334,981 | 11,500 | 1,113 |
| | 8.11.A | 44,370 | 9691,654 | 10,730 | 1,107 |
| | 9.11.B | 35,784 | 7782,802 | 9,125 | 1,172 |
| | 18.11.A | 32,417 | 6970,540 | 8,030 | 1,152 |
| | 18.11.C | 30,277 | 8322,657 | 9,609 | 1,149 |
| | 2.12.A | 38,865 | 8351,544 | 9,520 | 1,140 |
| | 2.12.B | 37,179 | 8028,394 | 9,700 | 1,208 |
| CONDITIONING | 8.11.B | 36,857 | 7958,773 | 9,390 | 1,180 |
| | 8.11.C | 35,601 | 7744,410 | 9,310 | 1,202 |
| | 10.11.A | 37,327 | 8161,137 | 9,920 | 1,216 |
| | 10.11.C | 40,814 | 8959,808 | 10,420 | 1,163 |
| | 18.11.B | 35,913 | 7712,101 | 8,830 | 1,145 |
| | 22.11.A | 44,840 | 9915,645 | 11,380 | 1,148 |
| | 22.11.B | 36,650 | 8330,177 | 10,070 | 1,209 |
| | 24.11.A | 47,366 | 10102,918 | 11,850 | 1,173 |
| | 24.11.B | 44,288 | 9729,666 | 11,590 | 1,191 |

Table 4 - Not-sensorized main specimens characteristics

### 3.1.1. Tensile tests on dry specimens

To kickstart the experimental phase, eleven unconditioned specimens underwent a tensile test campaign that led to their fracture. The tests were carried out at Politecnico's laboratory, using an MTS Electromechanical tensile machine (Figure 37) capable of measuring strains and stresses on the specimens by employing an extensometer, as well as setting a deformation speed.
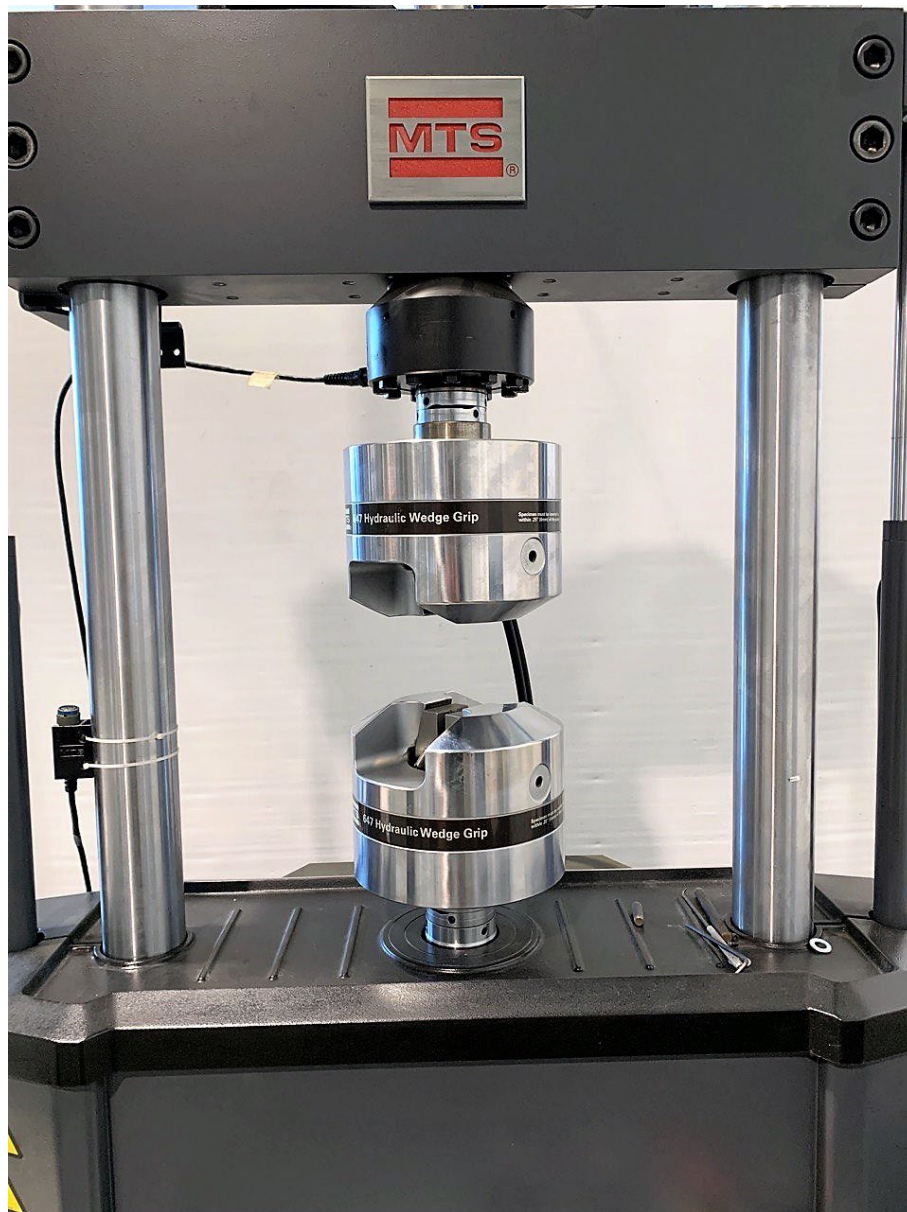


Figure 37 - MTS Electromechanical tensile machine

The primary objective of this activity was to obtain precise measurements of the essential mechanical properties of the components under analysis, including Young's modulus, breakage stress, and strain at break. It was crucial to test a sufficiently large sample size to obtain statistical indications on these properties, enabling a comparison of the conditioned components' performance, tested in Section 3.1.3.

Before conducting the tests, all the specimens underwent characterization. The thickness and width were measured at different points on each piece, as shown in Figure 38 and Figure 39. Additionally, the specimens were weighted with a precision balance, and their density was calculated to evaluate the presence of any air bubbles inside the components.



Figure 38 - Thickness measurement points
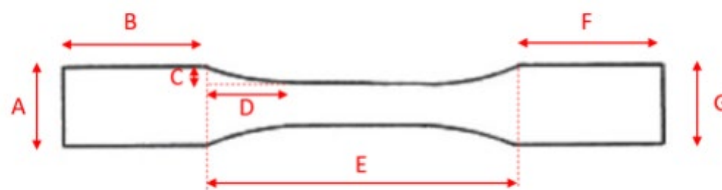


Figure 39 - Length measurement points

The tests conducted on the selected specimens enabled the observation of stress-strain diagrams, the trends of which are depicted in Figure 40 and Figure 41. The values for Young's modulus, stress, and strain at break for each specimen are reported in Table 5, while the average and standard deviation values are shown in Table 6.
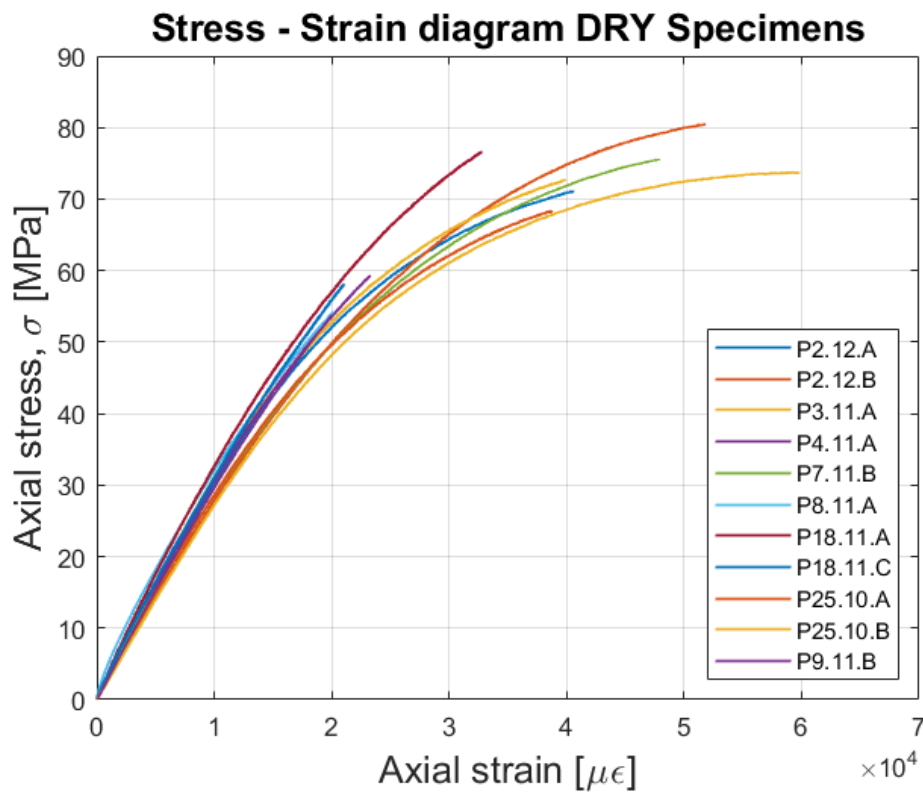


Figure 40 - Stress-Strain diagram of non-sensorized dry specimens

| Name | Young's Modulus $E\ [GPa]$ | Stress at break $\sigma_{BREAK}$ $[MPa]$ | Strain at break $\varepsilon_{BREAK}$ |
|---------|------|-------|--------|
| 25.10.A | 3,0 | 68,33 | 0,0387 |
| 25.10.B | 2,7 | 73,63 | 0,0598 |
| 3.11.A | 3,3 | 72,54 | 0,0399 |
| 4.11.A | 3,4 | 59,22 | 0,0233 |
| 7.11.B | 3,1 | 75,58 | 0,0479 |
| 8.11.A | 7,0 | 54,33 | 0,0201 |
| 9.11.B | 3,1 | 53,81 | 0,0200 |
| 18.11.A | 3,8 | 76,58 | 0,0327 |
| 18.11.C | 3,5 | 57,95 | 0,0210 |
| 2.12.A | 3,2 | 71,14 | 0,0406 |
| 2.12.B | 2,9 | 80,58 | 0,0518 |

Table 5 - Mechanical properties of unconditioned
.

The determined mechanical properties are almost uniform, even though some specimens, like 8.11.A, 9.11.B, and 18.11.C, fractured at lower strains and stresses, exhibited an elastic-fragile behavior, and lacked any signs of plasticization. While 25.10.B, on the other hand, has a longer plastic behavior and can withstand almost 60000με. This specimen will be studied in terms of chemical properties in Section 3.3, performing DSC analysis in order to calculate the glass transition temperature and check if it shows differences in terms of composition.
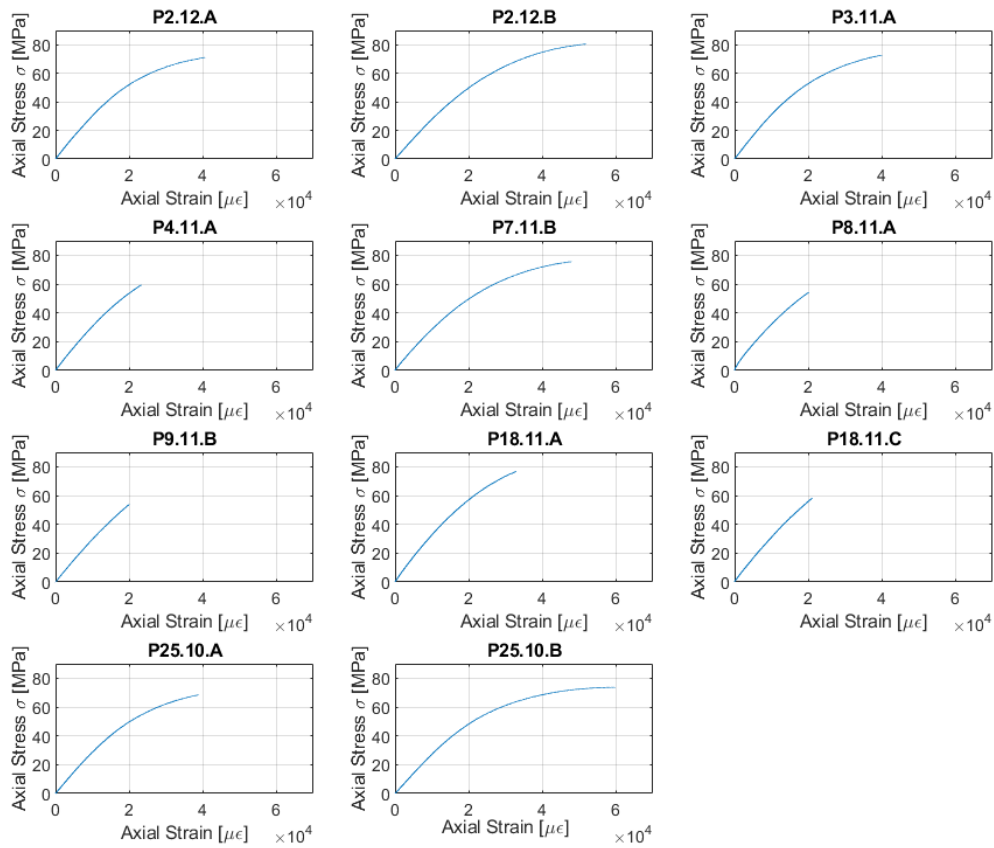
Figure 41 - Stress-Strain diagrams

| | Young's Modulus [$GPa$] | Stress at break [$MPa$] | Strain at break |
|---|---|---|---|
| Average | 3,20 | 69,57 | 0,0394 |
| Standard Deviation | 0,3309 | 8,488 | 0,0129 |

Table 6 - Average and standard deviation values (P8.11.A excluded)

## 3.1.2. Conditioning

The second test carried out consists of the immersion of a set of nine specimens to observe the mechanical properties variation on components that underwent moisture absorption. The process of humidity absorption in epoxy resin is a phenomenon that occurs over an extended period. To accelerate this process and recreate hot-wet conditions, this set was immersed in a water tank at $80°C$. The tank's control system maintained a water temperature that varied between $75°C$ and $85°C$, we will see the

consequences in Section 3.2.2. These specimens served as sentinel components, and their mass was periodically monitored to track the moisture absorption process and determine the time needed to achieve saturation.

The specimens were immersed for 1195 hours, and it was found that the mass increased by approximately 6.11%. This trend is shown in Figure 42, where each point on the plot represents the value:

$$\%m = \frac{m_k - m_0}{m_0}$$

Where $m_k$ is the average mass of the specimens at the k-measurement, and $m_0$ is the average initial mass of the specimens. Figure 43 displays the weight trend of each specimen, it is possible to observe that their behavior is consistent. Table 7 reports the initial and final values of the specimens' masses.
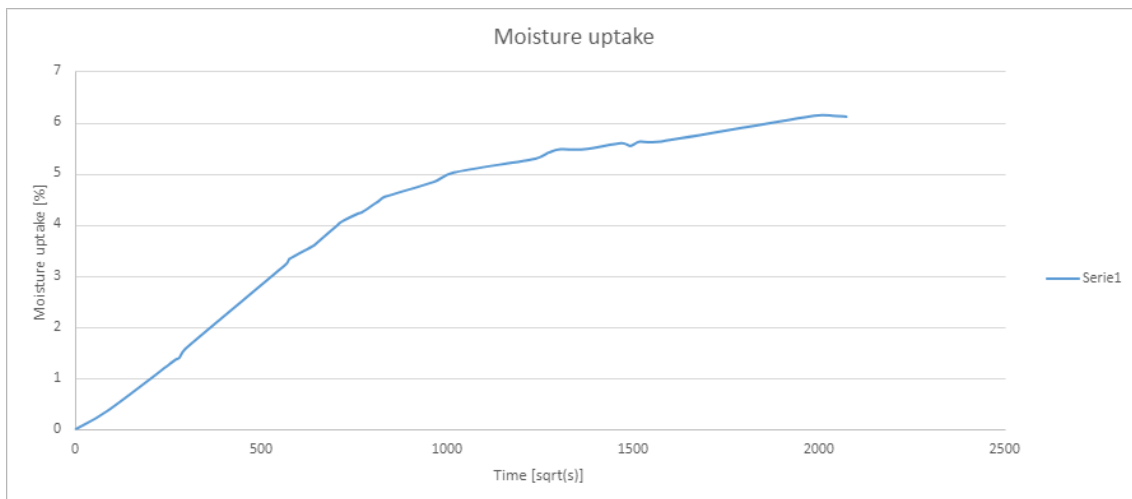


Figure 42 – Moisture uptake diagram

| Specimen | Initial mass $m_i$ [g] | Final mass $m_f$ [g] |
|---|---|---|
| 8.11.B | 9,39 | 9,94 |
| 8.11.D | 9,31 | 9,85 |
| 10.11.A | 9,92 | 10,52 |
| 10.11.C | 10,42 | 11,05 |
| 18.11.B | 8,83 | 9,34 |
| 22.11.A | 11,38 | 12,09 |
| 22.11.B | 10,07 | 10,68 |
| 24.11.A | 11,85 | 12,63 |
| 24.11.B | 11,59 | 12,33 |

Table 7 - Mass variations before and after the conditioning process.

From the figure above it is possible to observe that the absorption rate decreases over time since a plateau is reached. The absorption rate in an epoxy resin specimen decreases over time because, as the component absorbs moisture, it becomes increasingly saturated. As the resin reaches its saturation point, it can no longer absorb water at the same rate. This is because the resin's internal structure presents porosities and voids that become more filled with water molecules as the absorption process progresses, which restricts the ability of additional molecules to enter. Additionally, the absorbed moisture can cause swelling or expansion of the resin, which can create internal stresses that make it more difficult for additional water molecules to penetrate the resin. As a result, the absorption rate in the epoxy resin specimen typically decreases over time until it reaches a state of equilibrium, where the amount of moisture absorbed is balanced by the amount of moisture released.
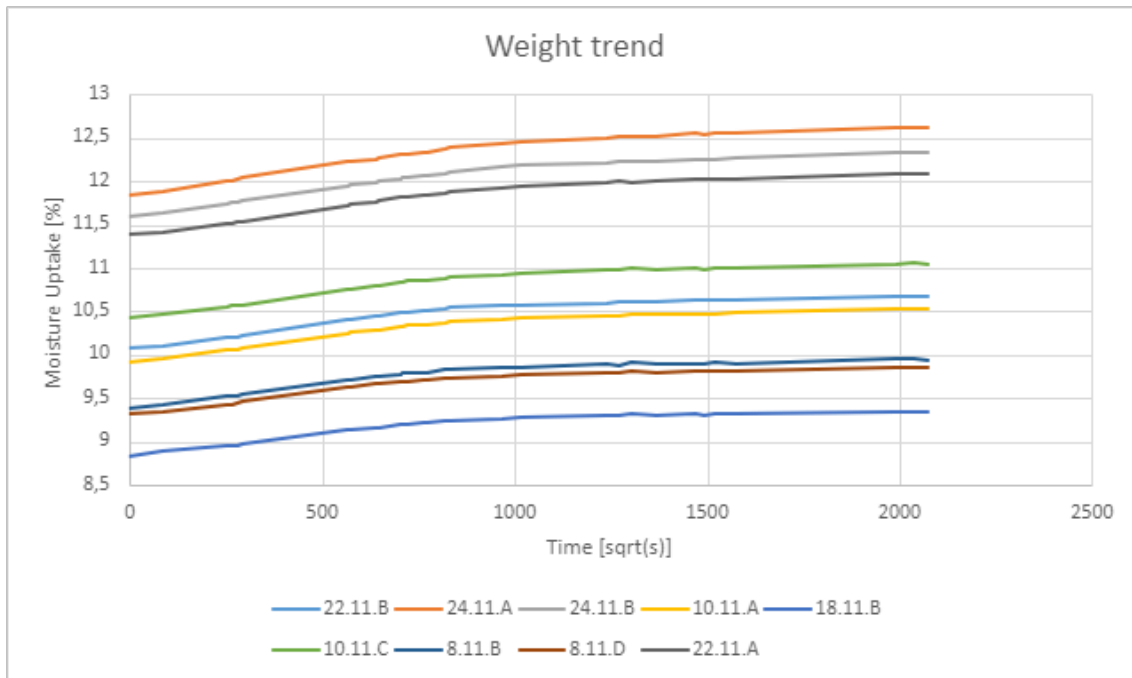
Figure 43 - Weight trend of each conditioned specimen

Another observed phenomenon was the whitening of the specimens. After several days of immersion, they changed color from transparent and shiny (as seen in Figure 36) to white and opaque (as shown in Figure 44). This whitening is due to a phenomenon called water whitening or blushing, which occurs because water and epoxy resin have different refractive indices. As the water molecules penetrate the resin, they interact with the polymer's molecular structure, causing a change in the way light is absorbed and reflected, resulting in the whitening effect.



Figure 44 - Whitening phenomenon

### 3.1.3.  Tensile tests on wet specimens

Once reached saturation, the specimens were divided into two groups, the first one underwent a tensile test campaign, while the second one underwent a drying process in an environmental chamber, as presented in Section 3.1.4.

In this section are presented the results and analysis done on the conditioned specimen tested with the MTS Electromechanical tensile machine already seen in Figure 37.

The specimens selected for this campaign are reported in Table 8, where it is possible to see their values of Young's modulus, breakage stress, and max strain. The average and standard deviation values are instead reported in Table 9.

From the stress-strain plots presented in Figure 45 and Figure 46, the homogeneous behavior of conditioned specimens can be observed. All the specimens present almost the same strain at break, and they show small differences in terms of maximum stress. Their behavior seems to present a short elastic phase that quickly becomes a plastic phase. This means that they are more deformable than dry specimens, but they encounter earlier breakage. The reduction of the elastic phase of epoxy resin immersed in water can be attributed to the material's plasticization. Water can reduce the material's glass transition temperature, leading to an increase in molecular mobility and a decrease in the material's stiffness. This behavior can result in a decrease in the material's ability to absorb elastic energy before breaking.

| Name | Young's Modulus $E\ [GPa]$ | Stress at break $\sigma_{BREAK}$ $[MPa]$ | Strain at break $\varepsilon_{BREAK}$ |
|---|---|---|---|
| 10.11.A | 3,50 | 52,85 | 0,0234 |
| 22.11.A | 2,42 | 48,65 | 0,0270 |
| 22.11.B | 2,62 | 56,53 | 0,0280 |
| 24.11.A | 2,60 | 50,72 | 0,0269 |
| 24.11.B | 2,57 | 55,60 | 0,0295 |

Table 8 - Young's modulus, breakage stress, and strain at break of conditioned specimens

| | Young's Modulus E [$GPa$] | Stress at break [$MPa$] | Strain at break $\varepsilon_{BREAK}$ |
|---|---|---|---|
| Average | 2,74 | 52,87 | 0,0270 |
| Standard Deviation | 0,4297 | 3,2911 | 0,0022 |

Table 9 - Average and standard deviation values
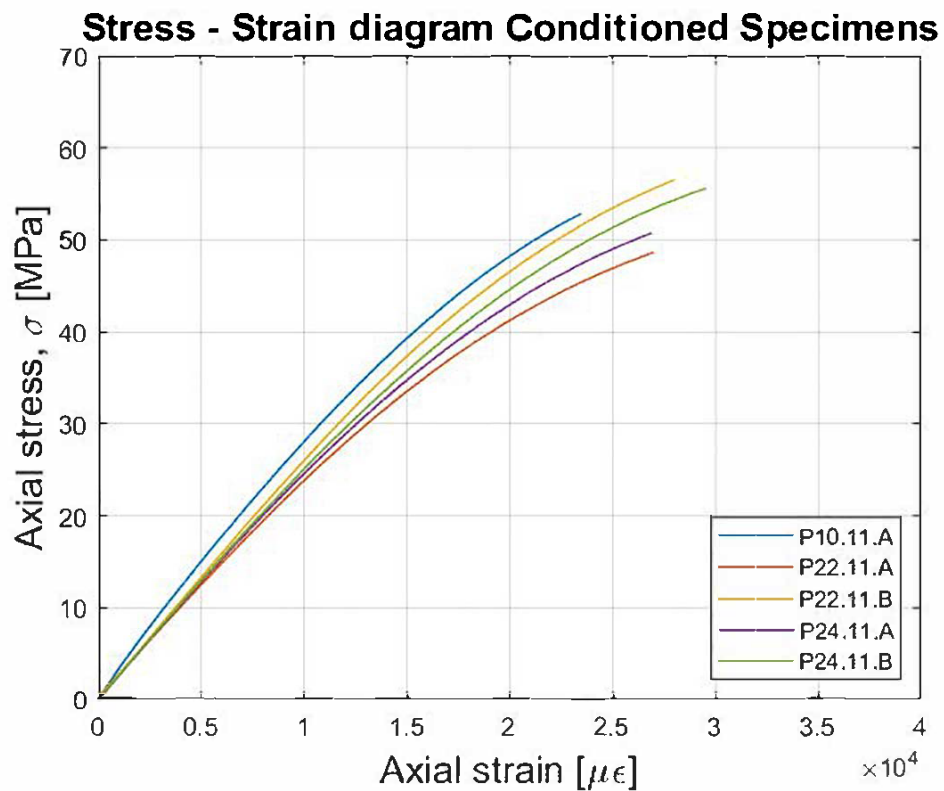


Figure 45 - Stress/strain diagram of conditioned specimens
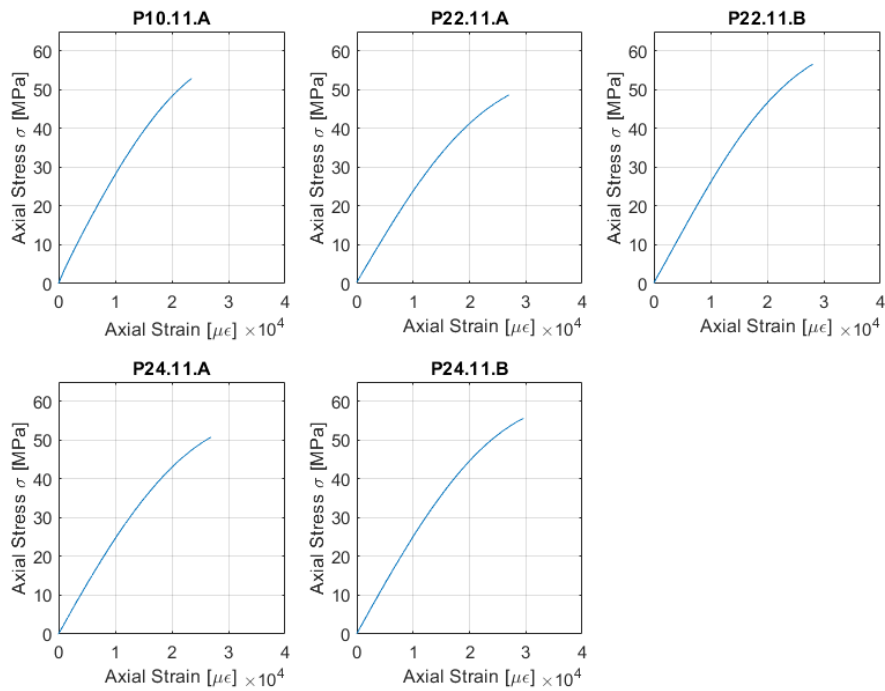
Figure 46 - Stress/strain diagrams of wet specimens

### 3.1.4. Drying process

As mentioned in Section 3.1.3, a group of four specimens underwent a drying process to check if the resin is able to recover its mechanical properties after letting all the water evaporate. The specimens selected for this procedure were: 18.11.B, 10.11.C, 8.11.B, and 8.11.D, whose characteristics are shown in Table 4.

The method selected to dry the specimens was to put them in a ventilated oven at 100°C in order to accelerate the drying process. The specimens were equipped with an extensometer through which it was possible to record all the strain generated on the components. The first specimen selected was 18.11.B but after two days of exposure, it was found bend because of the excessive temperature and the pressure carried out by the extensometer. In fact, high temperatures make the specimen to be more malleable. For this reason, the data collected on this first specimen were not relevant and with the other specimens, a temperature of 80°C was set in the oven.

The strains discovered on specimen 8.11.B are shown in Figure 47. The plot shows that, after sixty hours, the vibrations of the oven made the specimen fall and compromise the measurements. The test was stopped before the time requested by the specimen to lose all the moisture absorbed (Table 10 shows the values of the mass before and after this process).
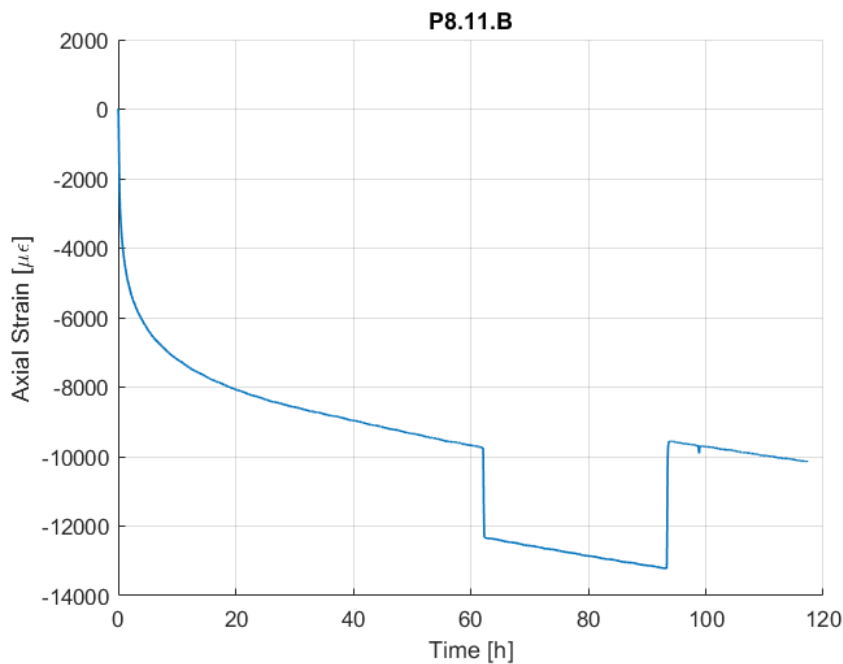
Figure 47 - Drying process of specimen P8.11.B

To solve the vibration problem, a small mass was placed over the structure in order to counterweight the specimen weight. In this way, the two next tests can be successfully performed. In Figure 48 and Figure 49 are reported the strain that specimens 8.11.D and 10.11.C underwent during the drying process. The strains recorded by the extensometer show a compression state during the evaporation of the water contained in the specimens, this means that the drying process implies a contraction of the component. When the epoxy resin specimens are subjected to a drying process to remove the moisture, the water trapped within the resin starts to evaporate. As the water evaporates, it creates empty voids within the material, causing it to compress and shrink in size. This compression state is due to the collapse of the voids created by the evaporating water.

The first segment of the curves is steep because the water starts to evaporate, but the slope decreases over time due to the increasing difficulty of the evacuation of the water. After 200-250 hours a plateau was reached and were not recorded any more deformations on the specimens.

From Table 10 is possible to observe the mass variation before conditioning, after conditioning, and after the drying process. As shown by these data, is not possible to recover the starting mass value measured. The cause of this phenomenon could be attributed to two different factors: the first is the possibility that some of the absorbed moisture remains trapped within the material, and the second is due to irreversible chemical reactions that may occur within the resin when it is subjected to moisture absorption. These chemical reactions may cause the formation of oxides during the conditioning process of the components. In fact, when exposed to water, the epoxy resin could react with water undergoing an oxidation reaction.
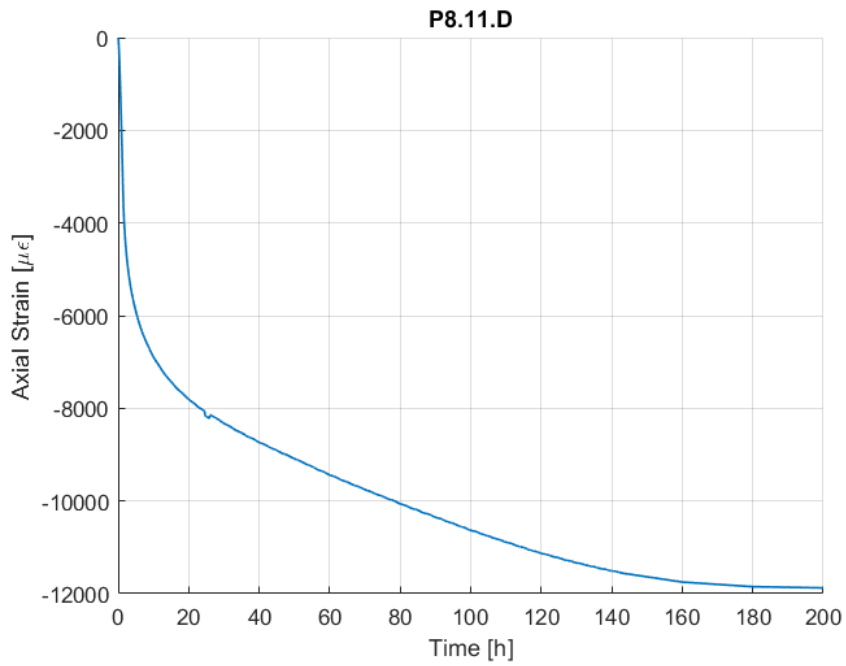
Figure 48 - Drying process of specimen P8.11.D
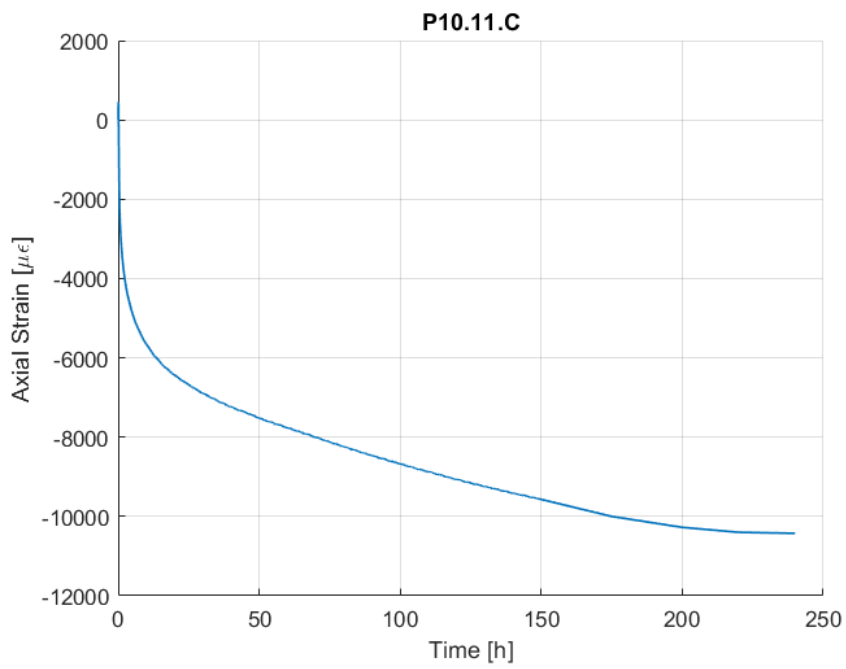


Figure 49 - Drying process of specimen P10.11.C

| Specimen | Mass before conditioning [$g$] | Mass after conditioning [$g$] | Mass after drying process [$g$] | % of mass recovered |
|----------|------------------|------------------|------------------|------------------|
| 8.11.B | 9,39 | 9,94 | 9,52 | 76,4% |
| 8.11.D | 9.31 | 9,85 | 9,40 | 83,3% |
| 10.11.C | 10,42 | 11,05 | 10,52 | 84,1% |

Table 10 - Mass values

### 3.1.5. Tensile test on dried specimens

After undergoing the drying process, the specimens were subjected to a tension test to determine if they were capable to recover their original mechanical properties, which are presented in Table 6. In Figure 50 it is possible to observe the behavior of the specimen tested under tension. They show an elastic segment until they reach the breakage point. They do not show any yielding or plastic deformation. As presented in Table 11, the elastic modulus is a little lower than the original one but the stress and strain at break are widely lower than the original one.
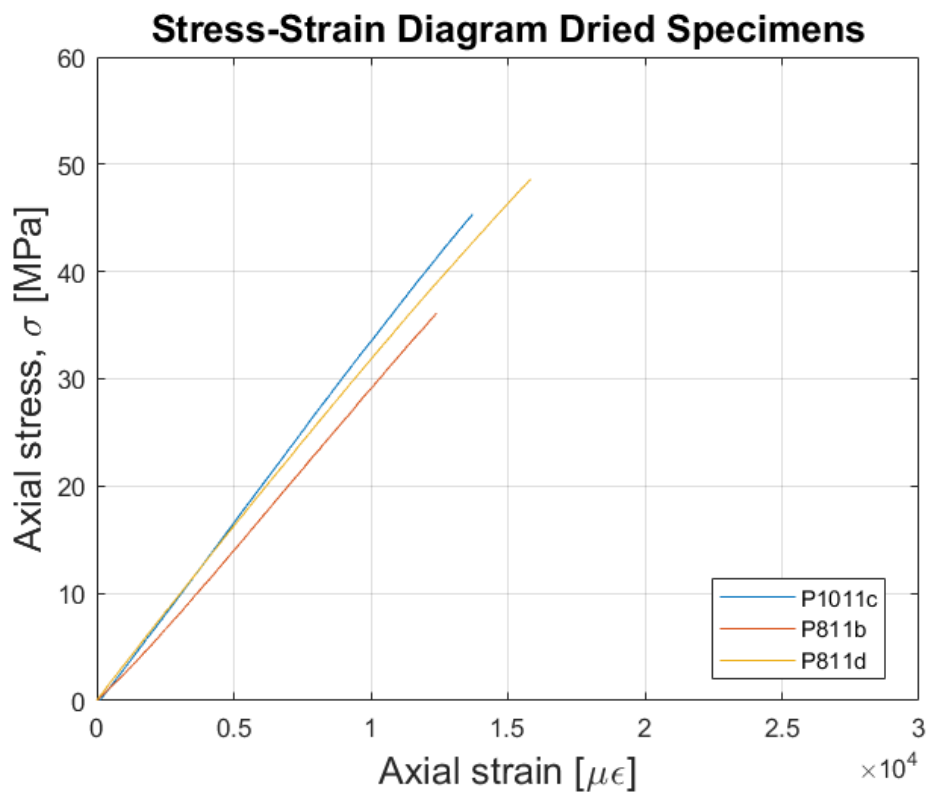


Figure 50 - Stress/strain diagram of dried specimens

| Name | Young's Modulus $E\ [GPa]$ | Stress at break $\sigma_{BREAK}$ $[MPa]$ | Strain at break $\varepsilon_{BREAK}$ |
|---|---|---|---|
| 8.11.B | 2,90 | 36,12 | 0,0124 |
| 8.11.D | 3,25 | 48,58 | 0,0158 |
| 10.11.C | 3,37 | 45,30 | 0,0137 |
| Average | 3,17 | 43,34 | 0,0140 |
| Standard Deviation | 0,2458 | 6,4589 | 0,0017 |

Table 11 - Values for Young's modulus, breakage stress, and max strain for each specimen, and their relative averages and standard deviations
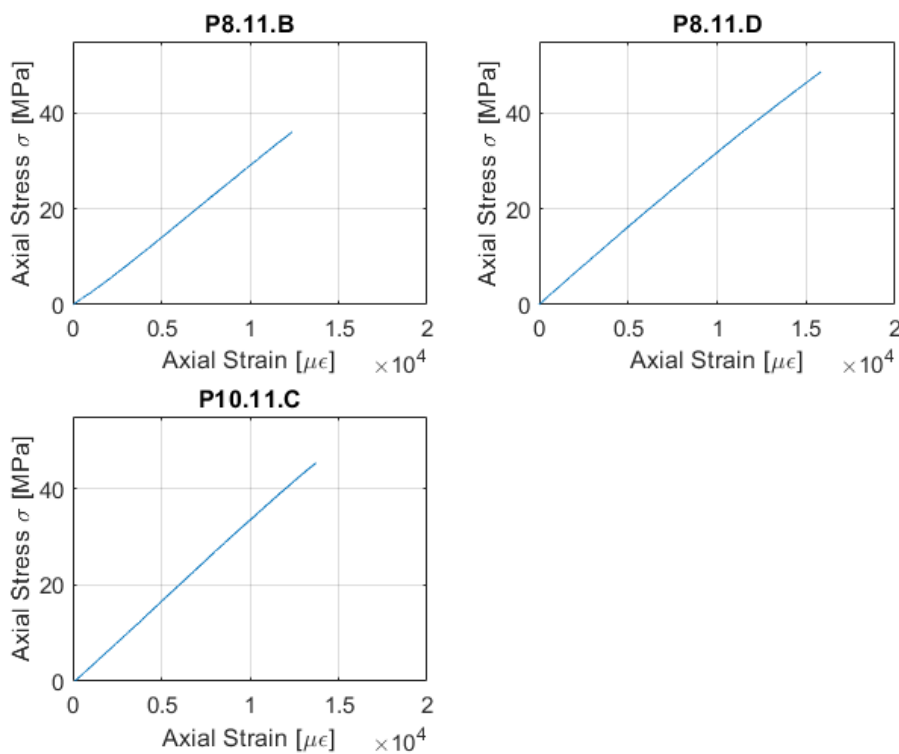


Figure 51 – Comparison between the three dried specimens

## 3.1.6. Comparison between dry, conditioned, and dried specimens

The plot presented in Figure 52 shows the behavior of the specimens tested in the previous section. The values were obtained by performing a mean on the values determined with tensile tests. From the picture above it is possible to observe that the

dry specimens show an initial elastic behavior until they reach the yield point, in which plastic deformation starts and proceeds until the breakage strain is reached.
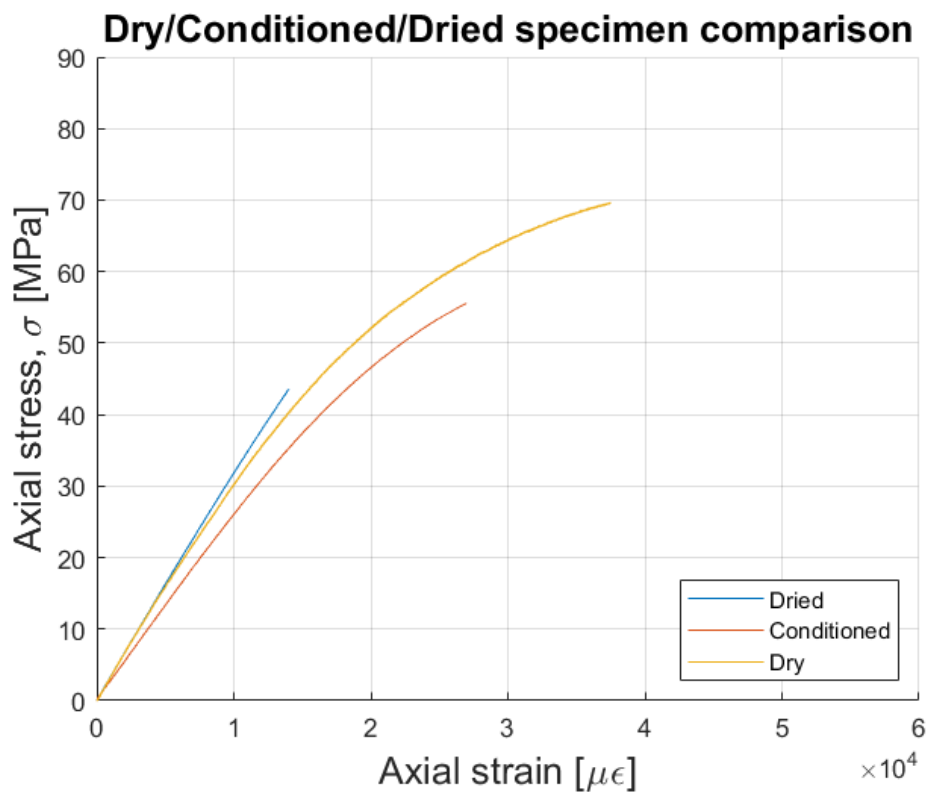


Figure 52 – Comparison between dry/wet/dried tensile tests

The conditioned specimens show a shorter elastic segment, characterized by a lower elastic modulus than the dry one. The breakage strain and stress are lower than the dry ones. These data confirm the deterioration of the material with a partial loss of the mechanical properties after a conditioning process with moisture absorption. When epoxy resin specimens are conditioned for an extended period in a hot water tank, they absorb water molecules, causing a chemical reaction known as hydrolysis. This reaction breaks down the chemical bonds in the resin, leading to a decrease in its mechanical properties, such as strength and elasticity. The absorbed water also causes swelling in the resin, which can lead to internal stresses and cracking when the specimens are subjected to mechanical loads.

Moreover, the dried specimens exhibit an elastic-fragile behavior where the components undergo a breakage phenomenon without presenting any plastic deformations. Contrary to what was presented in Section 1.1.2, the dried components are not able to recover their mechanical properties after a drying process in which the humidity absorbed was eliminated. The reason why the epoxy resin specimens do not recover their properties after a drying process is that the hydrolysis reaction that occurred during the conditioning process is not reversible. The breakdown of the chemical bonds within the resin and the subsequent formation of new chemical bonds with the water molecules cannot be undone by simply drying the specimens.

Additionally, during the drying process, the absorbed water molecules are driven out of the component, leading to a loss of mass and volume. This can cause the resin to shrink and develop internal stresses, which can further damage the material's mechanical properties. Furthermore, the hydrolysis reaction can also cause degradation of the resin's molecular structure, leading to a permanent decrease in its mechanical properties. This can result in a loss of strength, toughness, and elasticity, which cannot be fully restored even after drying the specimens. Overall, the irreversible nature of the hydrolysis reaction and the associated degradation of the resin's molecular structure are likely the main reasons why the epoxy resin specimens do not recover their properties after a drying process and may even show worse mechanical properties than before.

The average values for Young's modulus, stress, and strain at break are presented in Table 12.

|  | DRY | CONDITIONED | DRIED |
|---|---|---|---|
| Young's Modulus [$GPa$] | 3,20 | 2,74 | 3,17 |
| Stress at break [$MPa$] | 69,57 | 52,87 | 43,34 |
| Strain at break $\varepsilon_{BREAK}$ | 0,0394 | 0,0270 | 0,014 |

Table 12 - Average characteristic values of dry, conditioned, and dried specimens

## 3.2. Sensorized specimens

The next step in the experiment was to create the specimens for the conditioning cycle, in which were now embedded special fibers that had previously undergone laser engravings to create a Fiber Bragg Grating sensor, which was required to assess the material's hygrothermal effects, rather than simple fibers. The fragility and expense of the optical fibers, which posed a significant risk given that the fiber's length had to be sufficient to connect to the optical interrogator for calculating the variations in reflected wavelength, made the manufacturing process of these sensorized components crucial. This instrument is called Micron Optics and generates a light signal at the input of the fiber and reads the reflected one. To carry out the connection, the fiber's coating had to be removed using a specific tool called a stripper, which allows to apply the correct pressure to obtain the fiber coated with the cladding only. The bare stretch of fiber was then heated with a lighter flame and cleaned with an alcohol-soaked cloth. The actual fiber was then cut using a tool capable of making perpendicular cuts to the fiber's axis, which was crucial to obtain accurate readings. The two ends are then put into a precise welding machine, which can precisely align the two filaments and unite them by using a tiny electric arc. Polyimide material was used to coat the specified fibers, because of its hygroscopic properties. After being prepared, the sensorized fibers were placed in the mold and secured to a metal plate to keep them stretched. To get as much information as possible regarding the levels of strain inside the material during the production cycle, the equipment was placed in the oven. Two sensorized specimens and a non-sensorized one, which served as a sentinel throughout the conditioning test, were created during this phase. The implanted fibers were given two separate identification codes, FBG6466 and FBG6463. In the following sections, the FBG6466 will be identified with the subscript "$a$", while the FBG6463 with the subscript "$b$".

The fibers were linked to Micron Optics so that they could gather wavelength fluctuations during the whole production process, conditioning phase, and tensile tensing. Equation ( 1.22 ) will be utilized in the operations where the fiber was not embedded in the host material in the next sections, and ( 1.32 ) will be used in procedures where the fibers were embedded in the matrix. Analysis of the varied findings reveals that they are almost identical when using the alternative formulation described in Section 1.4.2.5 to compute the results.

In the following section, the values reported in Table 13 will be used.

|                                                                 | Glass Core | Polyimide Coating | Epoxy Resin |
|-----------------------------------------------------------------|------------|-------------------|-------------|
| Cross sectional Area $A \, [mm^2]$                              | 0,307      | 0,165             | 37,528      |
| Young's Modulus $E \, [GPa]$                                    | 72         | 2,45              | 3,2         |
| Coefficient of thermal expansion $\alpha \left[\frac{\mu\varepsilon}{K}\right]$ | 0.5        | 49                | 50          |
| Coefficient of hygroscopic expansion $\beta \left[\frac{\mu\varepsilon}{\%RH}\right]$ | 0          | 74                | 2000        |

Table 13 - Coefficient values for core, coating and host material

### 3.2.1. Manufacturing process

#### Fibers placing

The initial process involved putting the prepared fibers into the mold and fixing them to the metal plate. An initial stress condition on the fibers may result from this treatment. Because the fibers were not yet incorporated into the host material, this pre-stress may be estimated using Equation ( 1.22 ), as follows:

$$\frac{\Delta\lambda_B}{\lambda_B} = (1 - p_e)\varepsilon_M + (1 - p_e)\frac{E_c A_c}{E_c A_c + E_f A_f}\beta_c\Delta RH + \left\{(1 - p_e)\frac{E_c A_c \alpha_c + E_f A_f \alpha_f}{E_c A_c + E_f A_f} + \xi\right\}\Delta T$$

( 3.1 )

At $RH = 21,3\%$ and $T = 21,5°C$, the environment's relative humidity and temperature were measured. Since their values were stable during this procedure, $\Delta RH = \Delta T = 0$ was achieved. As a result, Equation ( 3.1 ) becomes simpler and reads as:

$$\frac{\Delta\lambda_B}{\lambda_B} = (1 - p_e)\varepsilon_M$$

( 3.2 )

The following equation was used to calculate the mechanical strains that generated on the fibers:

$$\varepsilon_M = \frac{\frac{\Delta\lambda_B}{\lambda_B}}{(1 - p_e)}$$

<div align="right">( 3.3 )</div>

Here, $\Delta\lambda_B$ is the difference between Bragg's wavelength recorded at $RH = 21{,}3\%$ and $T = 21{,}5°C$ without any mechanical stress applied and the wavelength measured after the insertion into the mold.

The measured strain was:

$$\varepsilon_{Ma} = 350{,}71 \; [\mu\varepsilon]$$

$$\varepsilon_{Mb} = 866{,}13 \; [\mu\varepsilon]$$

Using a value of $p_e = 0{,}2126$. Since this was a manual process, it was not possible to apply the same stress to both fibers, which is why the two numbers above were different. Pre-stress (PS) was determined by multiplying the strains by the fibers' Young's modulus, $E = 72MPa$, and getting the following values:

$$\sigma_{PSa} = E\varepsilon_{Ma} = 25{,}3 \; MPa$$

$$\sigma_{PSb} = E\varepsilon_{Mb} = 62{,}4 \; MPa$$

### Heating in the oven

The mold with the fibers was placed in the oven as the second stage to get it ready for casting the resin. The temperature ranges from $21{,}5°C$ to $120°C$ throughout this phase, and wavelength data were gathered. Analyzing the wavelength fluctuations, it was feasible to determine the strains resulting from temperature changes, and from the dilatations of the mold and metal plate. By adjusting Equation ( 1.16 ), the following results can be attained:

$$\varepsilon = \frac{\left(\frac{\Delta\lambda_B}{\lambda_B} - \xi\Delta T\right)}{(1 - p_e)}$$

<div align="right">( 3.4 )</div>

These strains are made up of three components: a mechanical contribution from the stretching of the fibers caused by mold and metal plate expansion; a thermal contribution from the dilatation of the grating pitch due to $\Delta T = 98{,}5°C$ (from 21,5 to 120°C), and a final contribution from $\Delta RH = -23{,}5\%$ (null relative humidity inside the oven), as reported by the following equation:

$$\varepsilon = \varepsilon_M + \varepsilon_{RH} + \varepsilon_T = \varepsilon_M + \frac{E_c A_c}{E_c A_c + E_f A_f}\beta_c\Delta RH + \left[(1 - p_e)\frac{E_c A_c \alpha_c + E_f A_f \alpha_f}{E_c A_c + E_f A_f} + \xi\right]\Delta T$$

<div align="right">( 3.5 )</div>

The plot in Figure 53, which shows the strains created in this phase, was derived by substituting the wavelength variation values, $\xi = 5{,}81 * 10^{-6}[K^{-1}]$, and $\Delta T$ in the Equation ( 3.4 ).
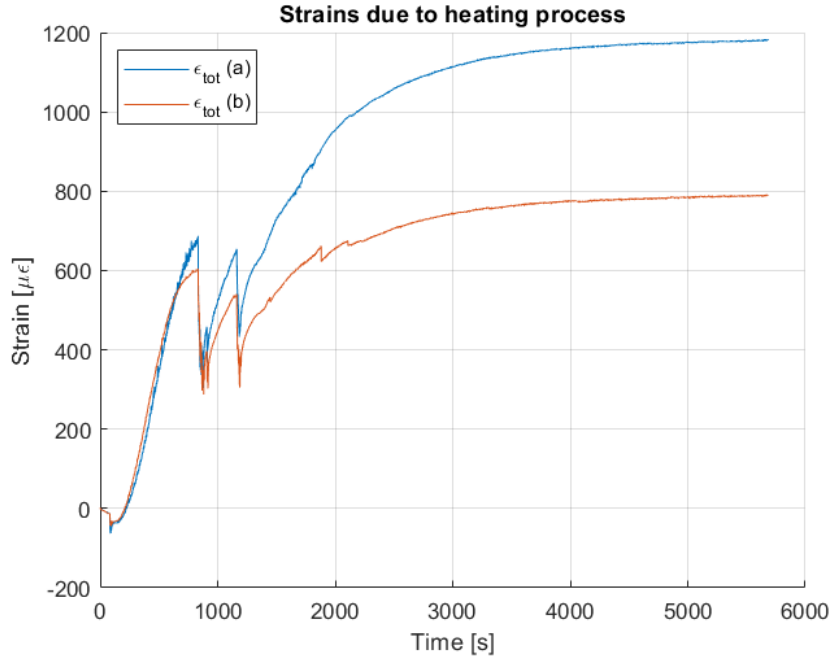


Figure 53 - Strains due to the heating process.

The image above demonstrates how sensitive the sensors are to temperature changes: throughout the heating process, the oven's door was partially opened in order to monitor the mold with the fibers, which results in considerable strain fluctuations in the range of hundreds of $\mu\varepsilon$. The two fibers had a different position in the mold, and they might experience various stress conditions, this may be the cause of the disparity between the two curves.

The strains depicted in the picture above represent the total effects of moisture, heat, and mechanical stresses. Their final values might be determined individually using the following equations:

$$\varepsilon_T = \frac{E_c A_c \alpha_c + E_f A_f \alpha_f}{E_c A_c + E_f A_f} \Delta T = 131{,}0 \ \mu\varepsilon$$

$$\varepsilon_{RH} = \frac{E_c A_c \beta_c}{E_c A_c + E_f A_f} \Delta RH = -33{,}6 \ \mu\varepsilon$$

$$\varepsilon_{M_a} = \frac{\left\{ \frac{\Delta \lambda_B}{\lambda_B} - (1 - p_e) \frac{E_c A_c}{E_c A_c + E_f A_f} \beta_c \Delta RH - \left[ (1 - p_e) \frac{E_c A_c \alpha_c + E_f A_f \alpha_f}{E_c A_c + E_f A_f} + \xi \right] \Delta T \right\}}{1 - p_e}$$

$$= 1084{,}5 \ \mu\varepsilon$$

$$\varepsilon_{M_b} = \frac{\left\{\frac{\Delta\lambda_B}{\lambda_B} - (1 - p_e)\frac{E_c A_c}{E_c A_c + E_f A_f}\beta_c \Delta RH - \left[(1 - p_e)\frac{E_c A_c \alpha_c + E_f A_f \alpha_f}{E_c A_c + E_f A_f} + \xi\right]\Delta T\right\}}{1 - p_e}$$

$$= 691,3 \ \mu\varepsilon$$

### Casting of the resin

The resin then proceeded through the cycle described in Section 2.1 to become liquid and allow any air bubbles to escape from it. The resin was then injected with a syringe into the mold. This phase was crucial for correct specimen production since poor casting could leave gaps and bubbles that would interfere with the moisture absorption process and compromise the accuracy of data acquisition. The resin may also redirect the fibers as a result of the casting process, producing incorrect measurement acquisition. Additionally, an incorrect casting technique could degrade the mechanical properties of the specimen.

During this procedure, wavelength variations were recorded, and they showed a decreasing trend due to the temperature drop caused by the opening of the oven and the compression state generated by the resin, mold, and metal plate.

The temperature decreased from 115°C to 95°C, giving rise to $\Delta T = -20°C$, while the relative humidity remained constant at 0%, therefore $\Delta RH = 0\%$. Equation ( 3.4 ) was used to compute the strains and stresses brought on by the contraction of the mold and the casting of the resin. The results for strains, expressed in micro-strains, are shown in  Figure 54.
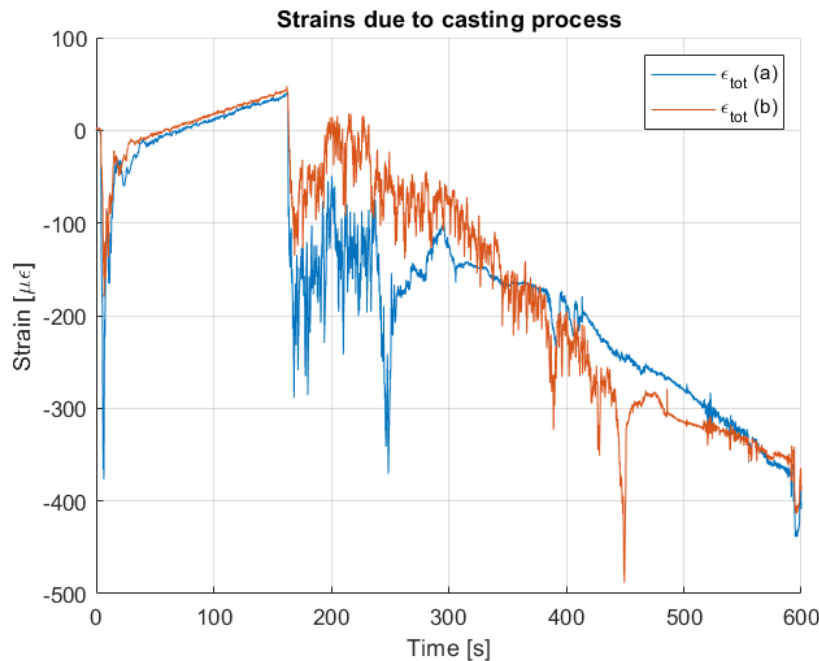


Figure 54 - Strains trend during the casting procedure

The resin was put into the mold at the time indicated by the two downward peaks in the plot. Due to the timing discrepancy between the casting processes for the two holes in the mold, these peaks happened at various times.

It is feasible to identify the individual contributions of the final strains, just as was done for the heating process:

$$\varepsilon_T = \frac{E_c A_c \alpha_c + E_f A_f \alpha_f}{E_c A_c + E_f A_f} \Delta T = -27{,}4 \ \mu\varepsilon$$

$$\varepsilon_{RH} = 0$$

$$\varepsilon_{M_a} = \frac{\left\{ \frac{\Delta \lambda_B}{\lambda_B} - \left[ (1 - p_e) \frac{E_c A_c \alpha_c + E_f A_f \alpha_f}{E_c A_c + E_f A_f} + \xi \right] \Delta T \right\}}{1 - p_e} = -374{,}5 \ \mu\varepsilon$$

$$\varepsilon_{M_b} = \frac{\left\{ \frac{\Delta \lambda_B}{\lambda_B} - \left[ (1 - p_e) \frac{E_c A_c \alpha_c + E_f A_f \alpha_f}{E_c A_c + E_f A_f} + \xi \right] \Delta T \right\}}{1 - p_e} = -355{,}4 \ \mu\varepsilon$$

### Curing process

After casting the resin into the mold, the oven was sealed, and the temperature was set to 120°C. the strains produced as the temperature increased to 120°C are depicted in Figure 55. The temperature increase did not occur instantly, it took some time to get going. The figure shows that the fiber's initial reaction was to go into compression as a result of the temperature drop. The deformations then turned positive, signifying an expansion of the fibers, as the temperature increased.
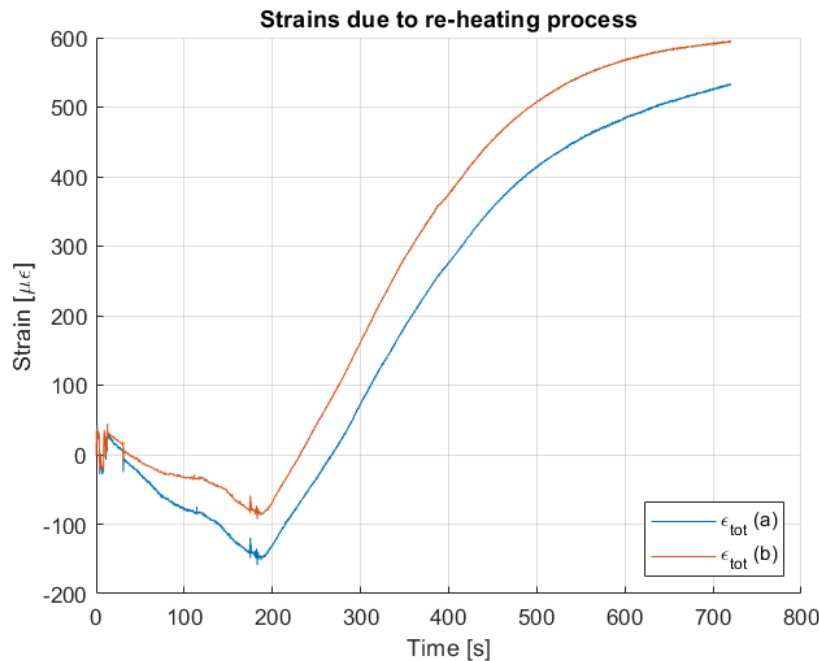


Figure 55 - Strains during the achievement of 120°C

The final strain values measured are:

$$\varepsilon_T = \frac{E_h A_h \alpha_h}{E_c A_c + E_f A_f + E_h A_h} \Delta T = 1052{,}8 \, \mu\varepsilon$$

$$\varepsilon_{RH} = 0 \, \mu\varepsilon$$

$$\varepsilon_{M_a} = \frac{\left\{\frac{\Delta\lambda_B}{\lambda_B} - \left[(1 - p_e)\frac{E_h A_h \alpha_h}{E_c A_c + E_f A_f} + \xi\right]\Delta T\right\}}{1 - p_e} = -520{,}9 \, \mu\varepsilon$$

$$\varepsilon_{M_b} = \frac{\left\{\frac{\Delta\lambda_B}{\lambda_B} - \left[(1 - p_e)\frac{E_h A_h \alpha_h}{E_c A_c + E_f A_f + E_h A_h} + \xi\right]\Delta T\right\}}{1 - p_e} = -458{,}1 \, \mu\varepsilon$$

It is evident that when the temperature rises, the resin expands with the fibers, while the resulting mechanical strains are negative due to the presence of the mold and the metal plate.

The curing procedure started once the target temperature was attained, and for an hour the temperature was kept constant ($\Delta T = 0$). The variation in relative humidity during this period can be considered as zero ($\Delta RH = 0$). Using Equation ( 3.3 ), it was once more feasible to calculate the strain produced during the resin's curing process. The acquired findings are presented in Figure 56. The trend reported in these plots displays a first increment of strain. This behavior is a result of the initial reaction of the curing process, which is characterized by a heat emission that gives rise to a temperature-related strain contribution. Then, the shrinkage phenomenon began, and it caused a steep drop in the deformations, generating a compression stress state. Epoxy resin shrinkage is a typical phenomenon that happens during the curing process, and it can cause several problems, such as cracking, distortion, and reduced mechanical properties. The polymerization reaction that takes place throughout the curing process is what causes this phenomenon. This reaction involves the conversion of the liquid resin into a solid polymer network. The resin's volume decreases as the polymerization reaction progresses, causing the shrinkage phenomenon and the development of a compression condition on the specimen. The fibers shank as the shrinking occurred, resulting in a decrease in the wavelength collected by the Micron optics.
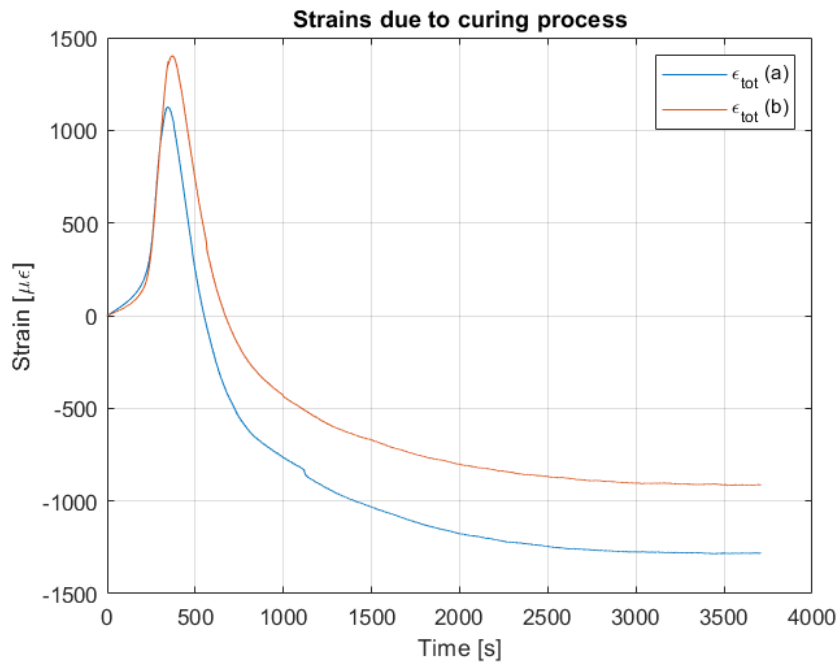
Figure 56 - Strains during the curing process

$$\varepsilon_T = \varepsilon_{RH} = 0 \ \mu\varepsilon$$

$$\varepsilon_{M_a} = \frac{\dfrac{\Delta\lambda_B}{\lambda_B}}{1 - p_e} = -1280,6 \ \mu\varepsilon$$

$$\varepsilon_{M_a} = \frac{\dfrac{\Delta\lambda_B}{\lambda_B}}{1 - p_e} = -912,6 \ \mu\varepsilon$$

Which correspond to the final values of the diagram reported above.

## Cooling process

The curing phase lasted for an hour before the oven was shut off, and the cooling began. The cooling process proceeded until the temperature reached 23°C (room temperature), from the initial temperature of 120°C, giving the result of $\Delta T = -97°C$. Variations in relative humidity variations can be regarded as insignificant ($\Delta RH = 0$). The decrease in temperature throughout the curing of the resin led to the development of a compression stress state, which caused the specimen to contract and the fibers to be compressed. Equation ( 3.4 ) was used to determine the strains from the wavelength data collected during this phase, and the results are presented in Figure 57. Despite a slight gain in the latest portion of the plot, their pattern is declining over time. Because data collection throughout the cooling process extended from the evening until the next morning and involved varied temperature values, this growth may be linked to an increase in the room temperature.
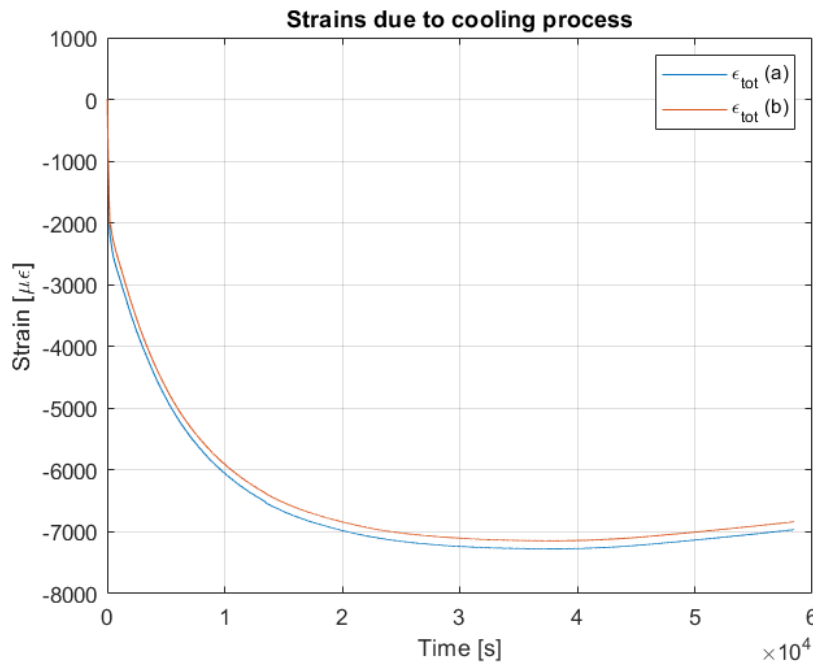
Figure 57 - Cooling process deformations trend

The final values for each strain are listed below:

$$\varepsilon_T = \frac{E_h A_h \alpha_h}{E_c A_c + E_f A_f + E_h A_h} \Delta T = -4084,9 \; \mu\varepsilon$$

$$\varepsilon_{RH} = 0 \; \mu\varepsilon$$

$$\varepsilon_{M_a} = \frac{\left\{ \frac{\Delta\lambda_B}{\lambda_B} - \left[ (1 - p_e) \frac{E_h A_h \alpha_h}{E_c A_c + E_f A_f + E_h A_h} + \xi \right] \Delta T \right\}}{1 - p_e} = -2878,9 \; \mu\varepsilon$$

$$\varepsilon_{M_b} = \frac{\left\{ \frac{\Delta\lambda_B}{\lambda_B} - \left[ (1 - p_e) \frac{E_h A_h \alpha_h}{E_c A_c + E_f A_f + E_h A_h} + \xi \right] \Delta T \right\}}{1 - p_e} = -2750,0 \; \mu\varepsilon$$

## Specimen extraction

Once the cooling phase was completed, the specimens needed to be removed carefully from the mold, so as not to damage the fiber integrity. Particularly, the discontinuity point where the fiber leaves the specimen might be weak. The strains created throughout this procedure are displayed in Figure 58.
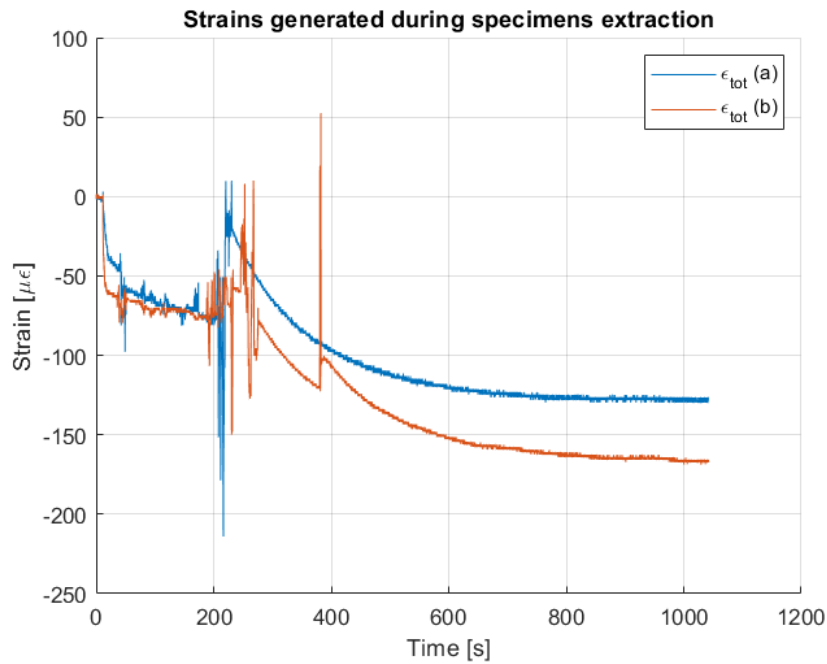
Figure 58 – Strains generated during the extraction process.

During the extraction phase, the strain contributions are:

$$\varepsilon_T = \varepsilon_{RH} = 0 \ \mu\varepsilon$$

$$\varepsilon_{M_a} = \frac{\dfrac{\Delta\lambda_B}{\lambda_B}}{1 - p_e} = -128{,}0 \ \mu\varepsilon$$

$$\varepsilon_{M_b} = \frac{\dfrac{\Delta\lambda_B}{\lambda_B}}{1 - p_e} = -167{,}3 \ \mu\varepsilon$$

### Complete manufacturing process

The total strain produced on the fibers may be estimated by adding together all of these phases, and the results are shown in Figure 59. It is possible to see that the fibers experienced a negative total strain as a result of the resin's tendency to shrink throughout the solidification process. This behavior demonstrates that residual compression stresses are produced during the specimens' production process.
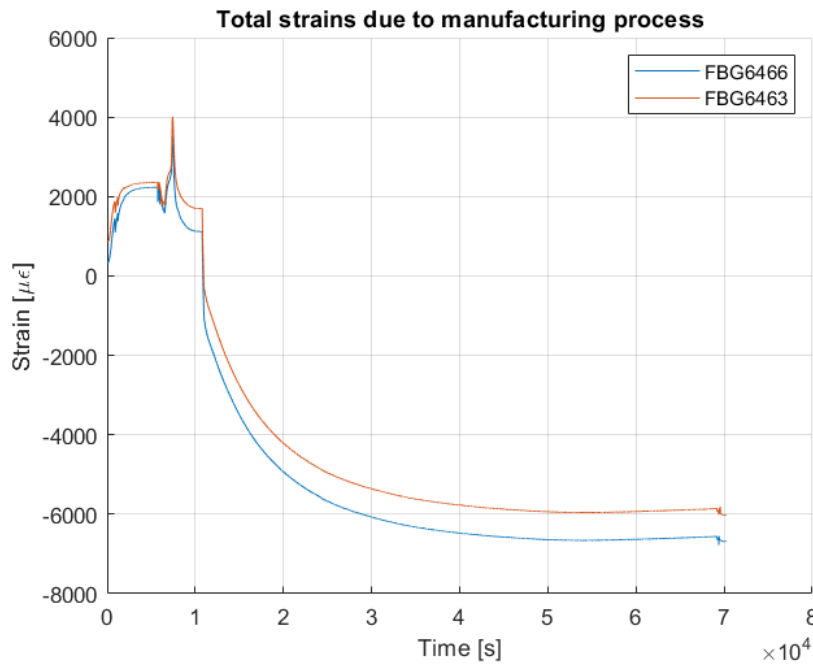
Figure 59 - Strains trend during the complete manufacturing process

The ultimate values for the strains developed over the whole manufacturing process are derived by adding together all the strains related to each production step, yielding the results listed below:

$$\varepsilon_T = -2928,5 \; \mu\varepsilon$$

$$\varepsilon_{RH} = -33,6 \; \mu\varepsilon$$

$$\varepsilon_{M_a} = -3749,9 \; \mu\varepsilon$$

$$\varepsilon_{M_b} = -3088,8 \; \mu\varepsilon$$

The strains mentioned above are relative to the fiber; the epoxy resin underwent only the strains related to casting, re-heating, curing, cooling, and extraction from the mold. Therefore, the strains that the material has acquired during the production process are obtained by omitting the pre-strains developed by the fiber during the insertion in the mold and the initial heating step.

$$\varepsilon_T = -3059,5 \; \mu\varepsilon$$

$$\varepsilon_{RH} = 0 \; \mu\varepsilon$$

$$\varepsilon_{M_a} = -5185,1 \; \mu\varepsilon$$

$$\varepsilon_{M_b} = -4646,2 \; \mu\varepsilon$$

The elastic modulus computed in Section 3.1.1 ($E_{dry} = 3,2 \; GPa$) was used to calculate the stresses created in the specimen from these strain values and the following results were obtained:

$$\varepsilon_{tot_a} = -8244,6 \; \mu\varepsilon$$

$$\varepsilon_{tot_b} = -7705,7 \; \mu\varepsilon$$

$$\sigma_{tot_a} = E_{mat}\varepsilon_{tot_a} = 26{,}4 \ MPa$$

$$\sigma_{tot_b} = E_{mat}\varepsilon_{tot_b} = 24.7 \ MPa$$
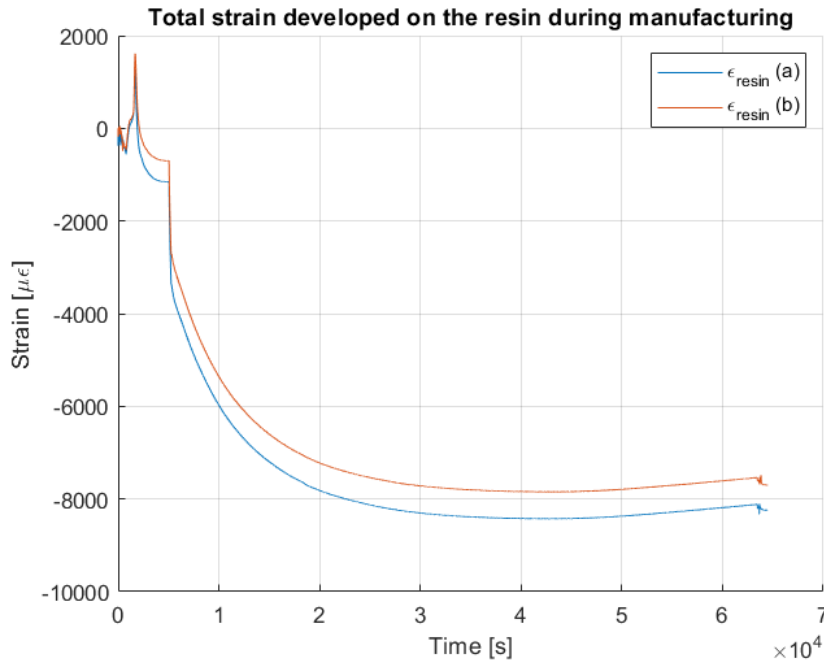


Figure 60 - Total strains on the specimen during manufacturing

## 3.2.2. Conditioning

An immersion test in water was the procedure's next step. In fact, the settling time to reach saturation for a composite material is in the range of a few years. However, by simulating atmospheric conditions where high temperatures and high levels of humidity coexist, such as through immersion tests, it is possible to experimentally accelerate these times. The tank used for this test was the same one used in the test described in Section 3.1.2, and its control mechanism keeps the water temperature fluctuating between 75 and 85°C.

An additional specimen with no FBG sensor was immersed alongside the two sensorized specimens in order to serve as a sentinel component. This specimen was weighted periodically, allowing to track the mass gain caused by conditioning and determine when the connectorized specimens' saturation condition was reached. The wavelength values of the light reflected by the FBG sensors installed in the two sensorized specimens were recorded by Micron Optics for the whole period of the immersion test, almost 1500 hours. The measured wavelength values that were captured by the instrumentation are shown in Figure 61. Due to the growing temperature from room temperature to 80°C during the first hour of the cycle, it is feasible to see that their values show a first increase. Figure 62 illustrates this tendency. The temperature varies continuously throughout the entire process, from 75 to 85*C, which affects the recorded wavelengths.
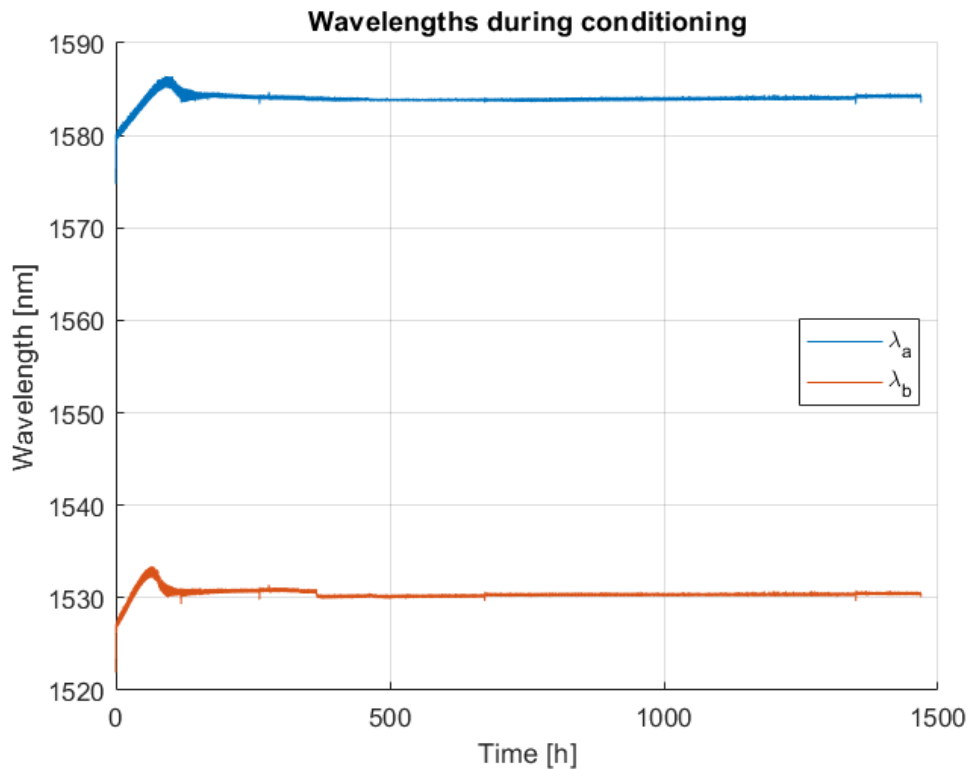
Figure 61 - Wavelength recorded during the conditioning process
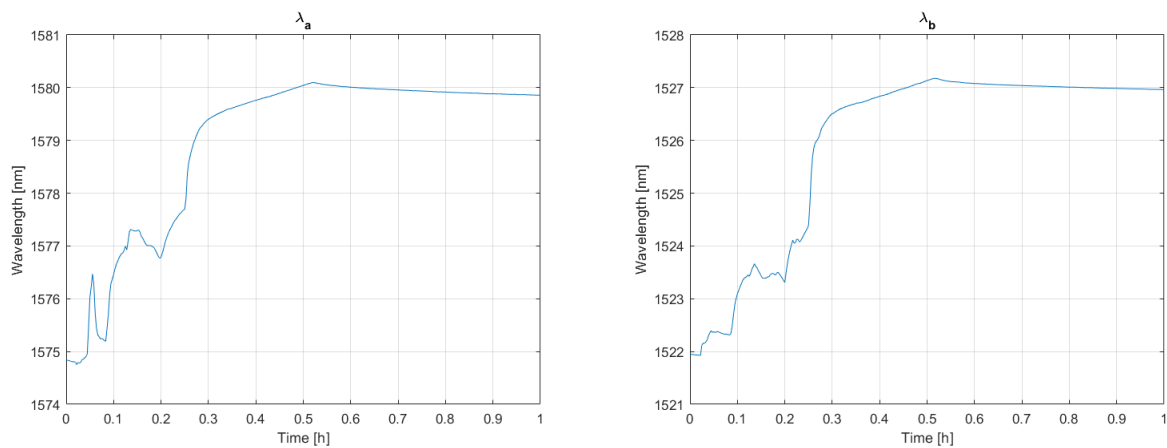


Figure 62 - Zoom in to the heating phase

These data may be used to identify the strains produced in the specimens during moisture absorption. At 80°C after its first increase, the temperature was regarded as steady.

The value of $\Delta T$ is considered linearly increasing from 0 to 60°C for the first hour and then settled constant at 60°C. therefore, it is possible to calculate the final value of the temperature-related strains:

$$\varepsilon_T = \frac{E_h A_h \alpha_h}{E_c A_c + E_f A_f + E_h A_h} \Delta T = 555,9 \ \mu\varepsilon$$

The strains due to moisture absorption are calculated using the following equation:

$$\varepsilon_{RH} = \frac{\left\{\frac{\Delta\lambda}{\lambda} - \left[(1 - p_e)\frac{E_h A_h \alpha_h}{E_c A_c + E_f A_f + E_h A_h} + \xi\right]\Delta T\right\}}{(1 - p_e)}$$

(3.6)

The findings in terms of strains are shown in Figure 63. The temperature-related contribution increased linearly during the first hour of the operation and remained constant after that. Mechanical forces did not contribute at all. The relative humidity term exhibits a rapid increase in the first 100 hours, followed by a sharp decline in value until it stabilizes at a value of roughly 6000 $\mu\varepsilon$. The non-monotonous trend of the micro-strains can be due to different dynamics which affect the material. One possible explanation for the first growth of the strains is that water initially penetrates rapidly into the surface because of the very high difference between the relative humidity inside the material (0%) and inside the tank (100%); therefore, the specimen is absorbing a lot of moisture, and this means that the dynamic of absorption is faster than the dynamic of relaxation of the material. The material accumulates water in the outermost zone of the specimen, causing rapid expansion. However, after about 100 hours of immersion, the water has diffused deeper into the resin, causing a decrease in the hydrostatic pressure on the surface of the specimen. This reduces the force that drives the resin to expand and, as a result, the deformation decreases. Furthermore, the hydrolysis reaction that occurs when water penetrates the resin can cause the breakage of chemical bonds in the structure of the resin, reducing its mechanical strength and decreasing the deformation over time. This hydrolysis reaction may be more intense in the early stages of immersion, causing a more rapid increase in deformation, but then slowing down after about 100 hours.
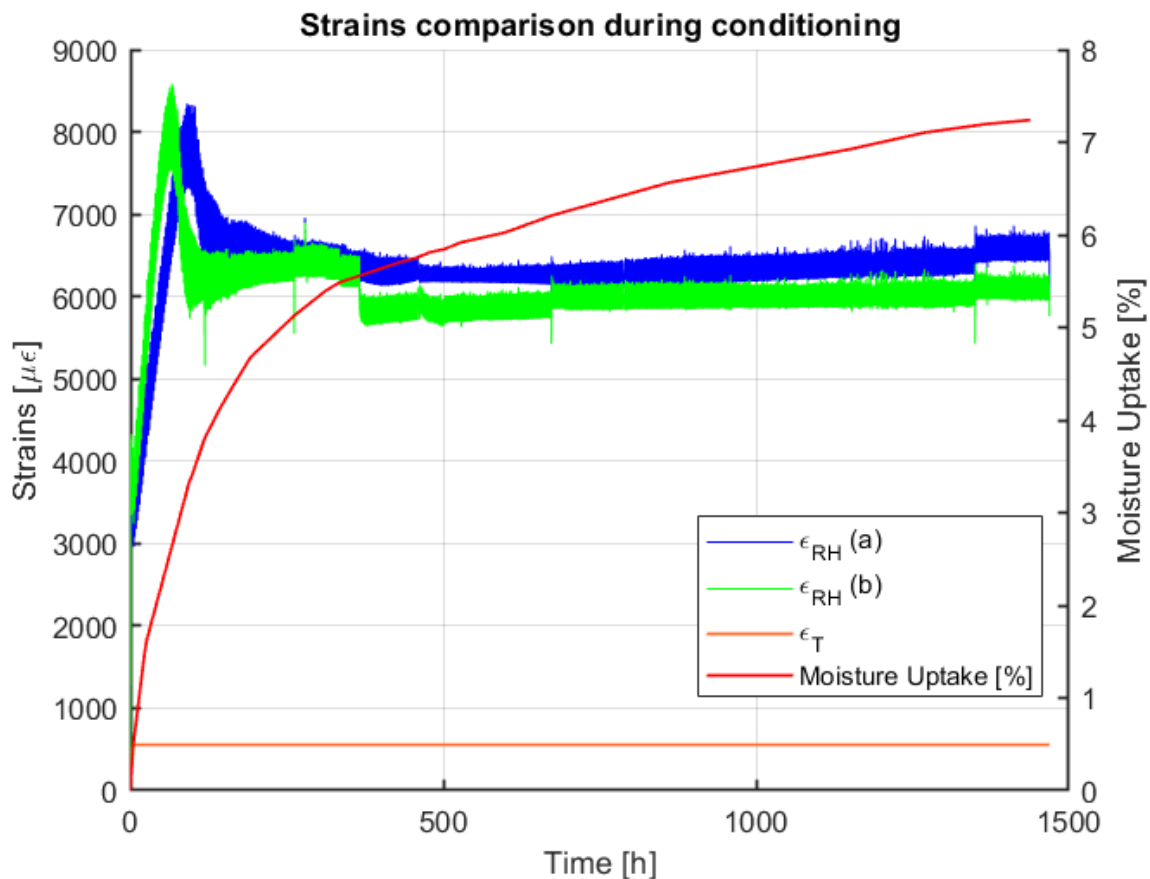
Figure 63 - Strains during conditioning / Moisture uptake

With periodic weighing of the sentinel specimen, the trend of moisture absorption, calculated as in Section 3.1.2, can also be shown in the image above. Despite the fact that the strains remain constant, the mass of the specimen is continuing to grow, and the moisture absorption achieves its maximum level of 7,24%.

### 3.2.3. Tensile tests

After almost 1500 hours of immersion in the hot water tank, the specimens were tensile tested to determine their mechanical characteristics after moisture absorption. While Micron Optics detected the wavelengths through the optical fiber, an extensometer monitored the axial strain and stress, as shown in Figure 64. Because the temperature and humidity remained constant during the experiments, the stresses on the specimens were purely mechanical. The equation ( 3.3 ) may be used to compute the stresses on the resin by determining the strains on the component from the wavelength fluctuations and multiplying them by the Elastic modulus determined in Section 3.1.3.

By comparing the results from the extensometer to those acquired through the fibers, it is feasible to establish whether the fiber coating is capable of appropriately transferring loads from the component to the sensor's core. This is an essential step in

establishing if the sensor developed is truly capable of operating appropriately for the intended purpose. The results for the two sensorized specimens and the sentinel specimen are shown in the subsections below. Finally, a comparison of these tests with the tests performed in Section 3.1.3  is presented.
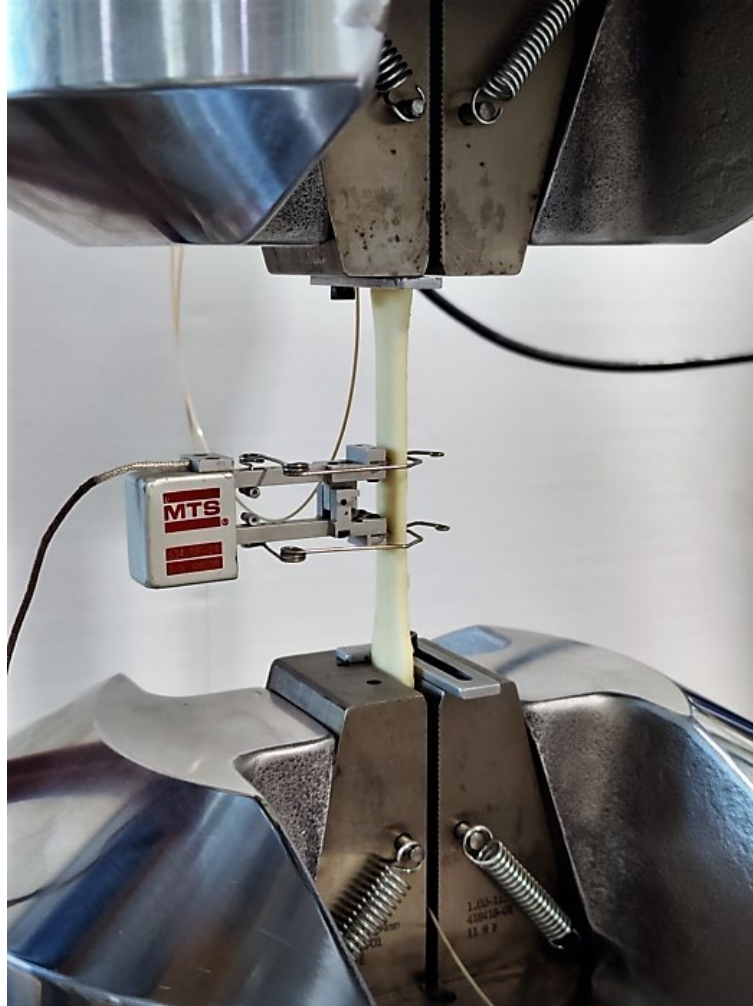


Figure 64 - Test setup

### FBG6463

The initial step in the test is to position the specimen and secure it in the tensile test machine, taking care not to damage the sensor. During this procedure, the wavelength values were gathered, and the component's pre-strains were measured. Figure 65 depicts the micro-strains reaching a value of 1500 $\mu\varepsilon$.
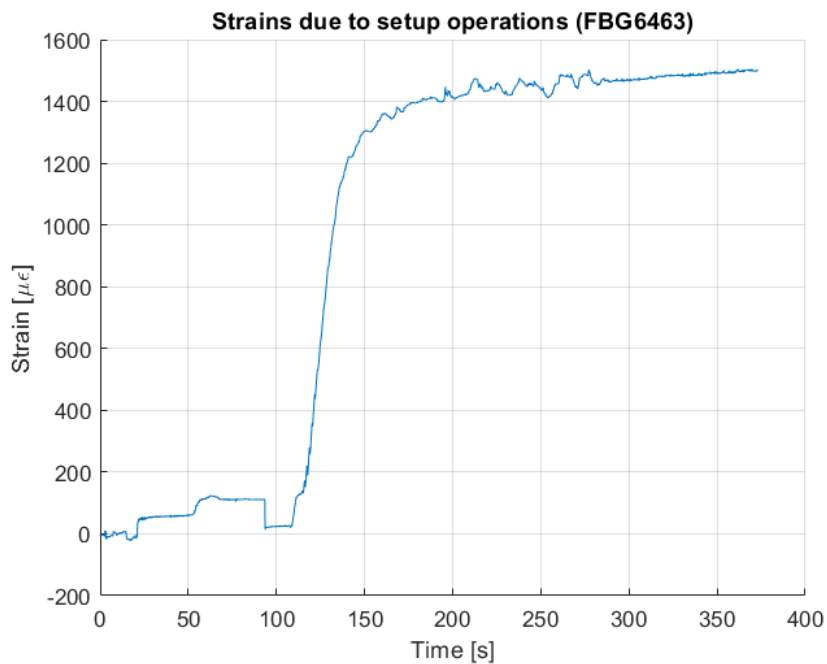
Figure 65 - Assembly operations of the specimen on the tensile machine (FBG6463)

The tensile test began after the specimen was ready, and Figure 66 depicts the strain trend. The strains measured through the fiber are lower than the strains observed by the extensometer. This might be due to a breakdown in the adhesion between the fiber's coating and the component, caused by the penetration of the water inside the material. Furthermore, as the strain reached 8700, an unloading phase began, followed by another load cycle. The fiber was no longer functional, and a signal loss was discovered because of sensor damage. The greatest stress imposed was 23,2 MPa until the sensor failed.

The specimen was then loaded until it broke, and the Stress-Strain diagram is shown in Figure 67.
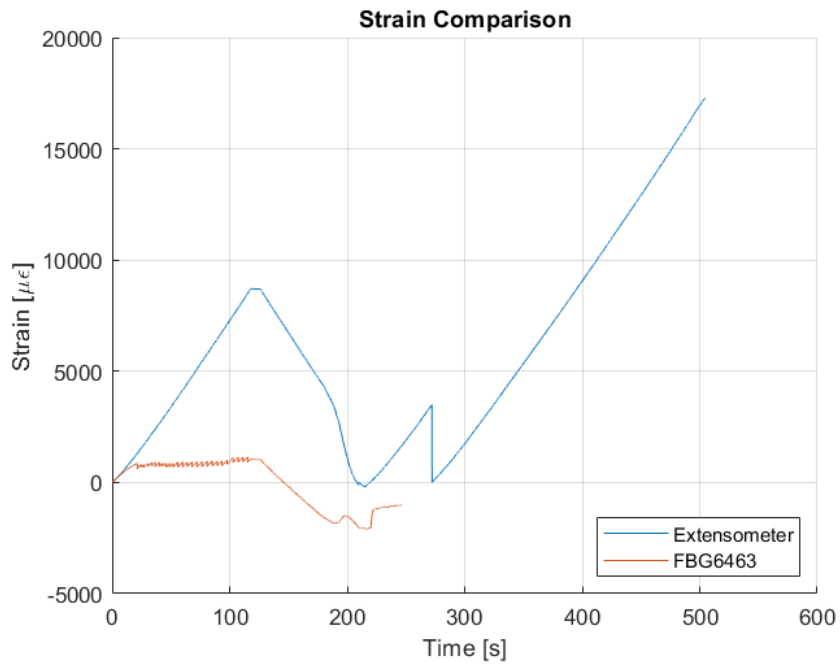
Figure 66 - Comparison between strains recorded with the fiber and the extensometer (FBG6463)
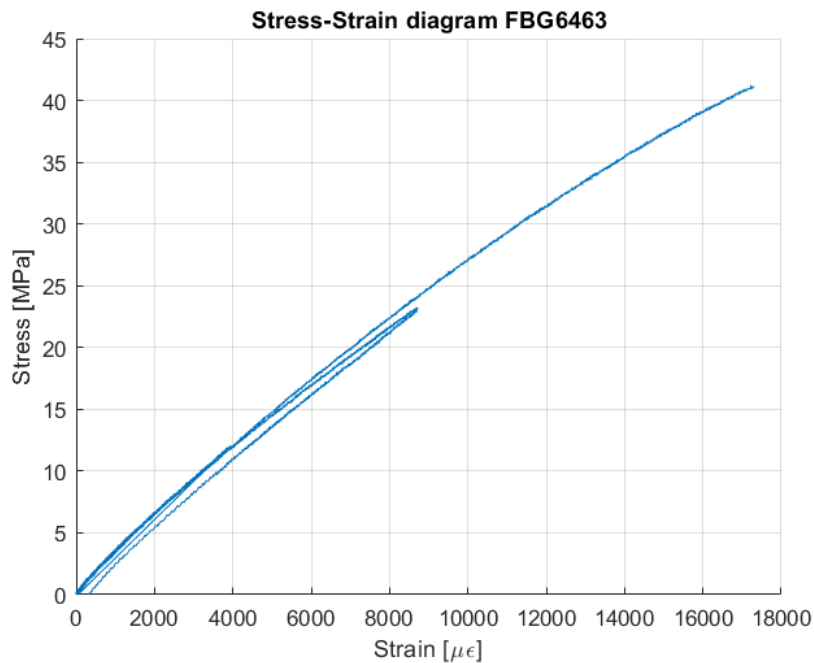


Figure 67 - Stress strain diagram obtained through the extensometer (FBG6463)

## FBG6466

The same tests were performed on the second specimen with the FBG sensor embedded, and as reported in Figure 68, a reduced pre-strain was developed on the component during setup construction. The fiber FBG6466 performed better than the

prior sensor because it could better follow the strains recorded by the extensometer, as shown in Figure 69. Anyway, after passing 8000 $\mu\varepsilon$, a signal loss was recorded, and the fiber sensor was no longer able to detect the peak. This sensor behavior denotes the fragilization of the fibers and the loss of adhesion between the sensor and the host material after the conditioning procedure.
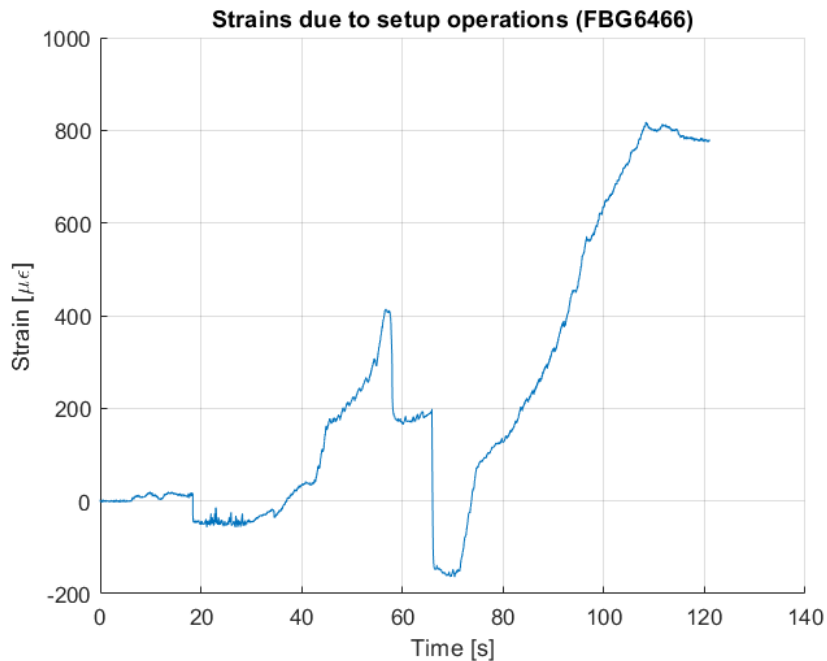


Figure 68 - Assembly operations of the specimen on the tensile machine (FBG6466)
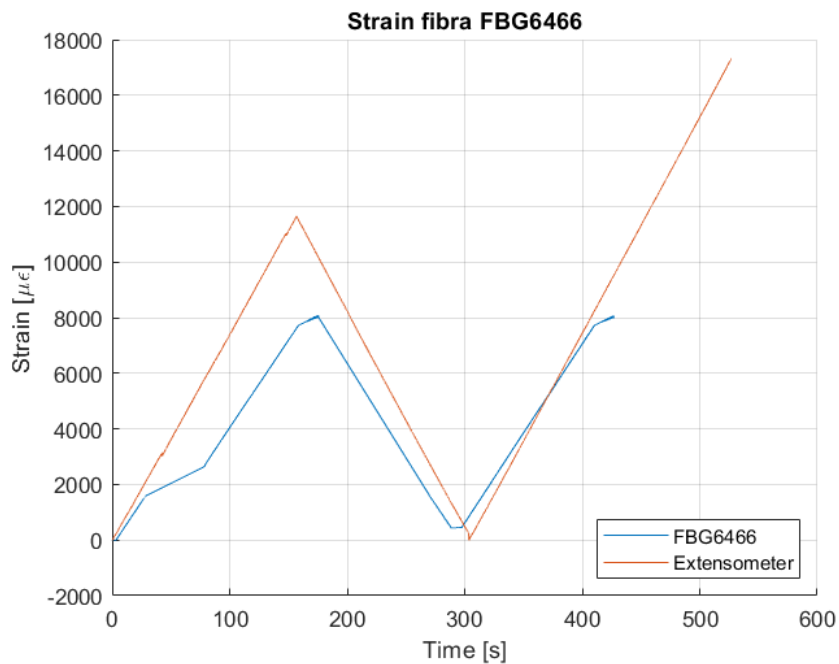


Figure 69 - Comparison between strains recorded with the fiber and the extensometer (FBG6466)

The stress-strain diagram of the sensor is shown below, with the data received by the extensometer and the fiber superimposed until the FBG detected the peak. This specimen behaves similarly to the previous one, indicating that the two components were manufactured in a comparable manner.
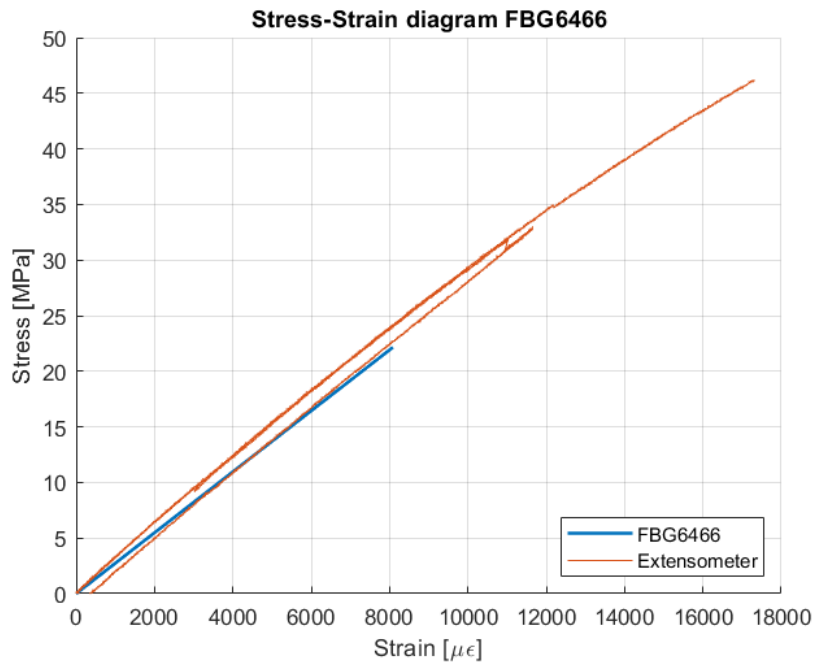


Figure 70 - Stress strain diagram obtained through the extensometer and the FBG sensor (FBG6466)

## Sentinel Specimen

The final step of this experimental phase is to test the sentinel specimen to see if the embedded fiber adds any strength to the component. The specimen was tested using an extensometer to measure the stress and strain, and the results are shown in the figure below. It is possible to observe that the specimen behaves similarly to the previously tested components.
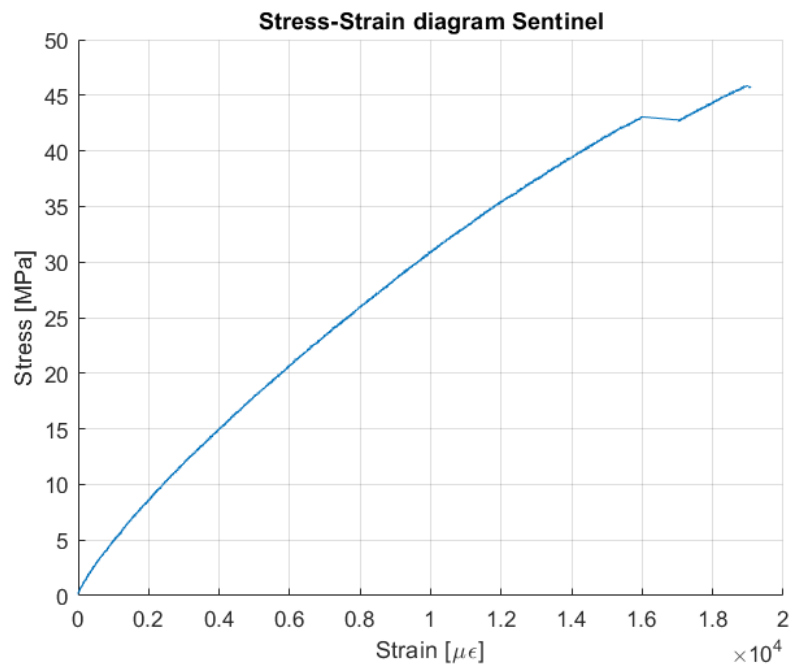
Figure 71 - Stress strain diagram obtained through the extensometer (Sentinel)

## Comparison

After the three specimens have been tested, the stress-strain curves may be compared to those produced in Section 3.1.3. It is reasonable to infer from the graph shown in Figure 72 that the behavior of the specimens recently examined has a comparable behavior in terms of elastic modulus but that they break earlier than the non-sensorized one. This result might be explained by the fact that these specimens were submerged for a longer period than in the previous conditioning test (1469 vs. 1195 hours), which could have resulted in a further loss of the constituents' mechanical properties.
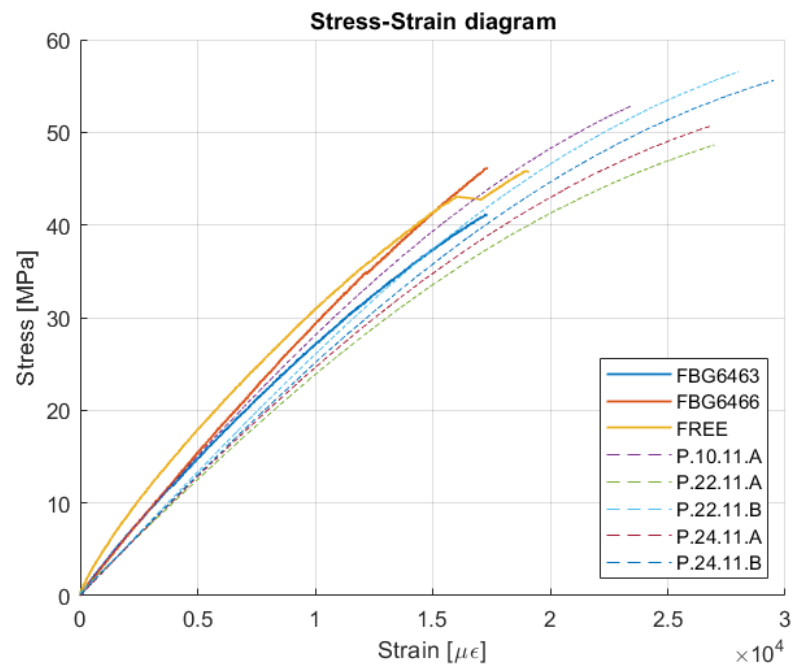
Figure 72 - Stress/Strain comparison between sensorized and non-sensorized specimens

## 3.3. DSC analysis

Differential scanning calorimetry is one of the most widely used analytical techniques for the characterization of polymers, thanks to the wealth of information it can provide and the ease with which the measurement can be performed on the sample of interest. A DSC calorimeter measures the heat flows associated with thermal transitions that occur in a sample when it is heated/cooled (dynamic conditions) or maintained at a constant temperature (isothermal conditions) in a controlled manner. This allows the user to determine at which temperature or temperature range any transitions (melting processes, crystallization processes, etc.) occur in the sample and to quantitatively measure the energies associated with them. In order to identify any differences in the glass transition temperature ($T_g$) of Epoxy resin samples before and after conditioning in water, DSC analysis was performed in this thesis research. This investigation was motivated by the fact that $T_g$ affects the material's mechanical characteristics by altering the mobility of the molecular chains. Specifically, the $T_g$ of a polymer is the temperature at which it transitions from a hard, glassy state to a rubbery, more flexible state. The molecular weight and cross-linking density of the transition can have an impact on the mechanical characteristics of the material, such as stiffness and toughness. Therefore, it is feasible to learn more about how the material's mechanical properties may be impacted by various environmental circumstances, such as high humidity environments, by examining changes in $T_g$ before and after conditioning the specimens in water. Table 14 displays the values of glass transition temperatures of selected specimens. In particular, two specimens were chosen, namely 25.10.B in the 2dry2 configuration and 24.11.A which underwent the conditioning cycle. From the table, it can be observed that the $T_g$ has significantly decreased after immersion in hot water. In fact, if a specimen is left in hot water for an extended period of time, the material may undergo a reduction in $T_g$ due to water absorption and the consequent decrease in polymer network density. The absorption can lead to an increase in the molecular mobility of the resin, causing greater deformations at high temperatures. In fact, when the specimens were taken out of the bath, they were highly malleable. This can result in a reduction in the mechanical strength of the material and compromise its structural integrity. Looking at the table, it can be noticed that the strain at break has significantly decreased.

|  | 25.10.B (DRY) | 24.11.A (WET) |
|---|---|---|
| $T_g$ [°C] | 121,06 | 99,55 |
| $E$ [GPa] | 2,7 | 2,6 |
| $\varepsilon_{brk}$ | 0,0598 | 0,0269 |

Table 14 - Glass Transition Temperature values
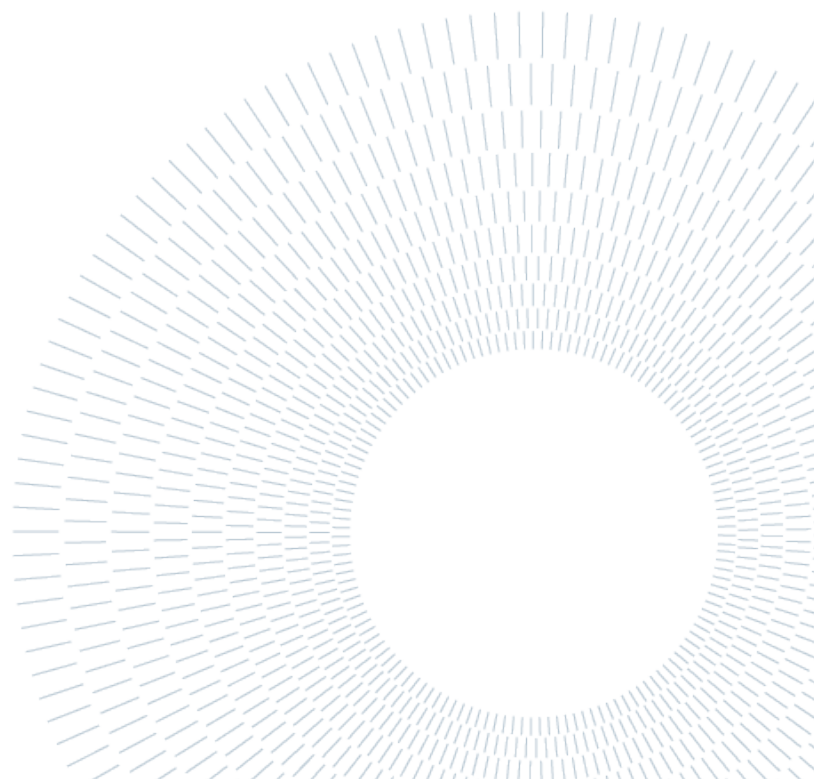
# 4  Conclusions

After completing the experimental tasks outlined in this thesis, it is feasible to present some general observations with the intention of giving the reader a helpful overview, highlighting the key technological challenges faced, and drawing conclusions about the work done.

The first challenge encountered in this thesis work was the correct production of epoxy resin specimens. It was necessary to develop a proper heating cycle, ensure air release from the resin, and establish a curing cycle to produce defect-free specimens without voids or air bubbles that could affect water absorption or mechanical properties of the material. After several attempts, a guideline was developed for the correct manufacturing process of the components, which could be useful in the future. Once familiar with the production process, two major areas of testing were programmed.

The first series of tests aimed to characterize the material's mechanical properties through tests of tensile strength under dry conditions, wet conditions after conditioning in a water tank, and post-drying conditions. Every test revealed interesting results. The data extracted from the extensometer used during the tensile test on dry specimens revealed the epoxy resin's elastoplastic properties from which the average elastic modulus of the specimens was determined to be $E_{dry} = 3,2\ GPa$. The average maximum stress supported by the material determined from the tests was $\sigma_{brk_{dry}} = 69,57\ MPa$, while the breakage strain was $\varepsilon_{brk_{dry}} = 0,0394$. Some exception aside, due to internal defects in the material, all specimens exhibited very similar characteristics, indicating a correct manufacturing process.

The second test, as previously mentioned, involved conditioning the specimens by immersing them in a hot water tank ($T = 80°C$) to simulate hot-wet environmental conditions and accelerate moisture absorption. The immersed specimens were daily weighted with a precision balance to monitor their mass gain and determine the percentage of water absorbed. After 1195 hours of immersion, the specimens reached saturation, with a mass gain of 6,11%. This monitoring made it possible to observe how the absorption process varied over time, with a rapid initial mass growth, followed by a slower process due to water molecules struggling to penetrate the material as porosities became more filled. In addition, water entry into the material can cause swelling and expansion, generating internal stress that further complicates water penetration. At saturation, an equilibrium state was achieved, where the amount of water entering was equal to that leaving the material. After conditioning, these

samples were then subjected to tensile testing to determine if their mechanical properties had changed after the conditioning process. As expected, these tests showed a deterioration in mechanical properties, with a Young's modulus of $E_{wet} = 2,74\ GPa\ (-14,3\%)$, stress and strain at fracture of $\sigma_{brk_{wet}} = 52,87\ MPa\ (-24\%)$ and $\varepsilon_{brk_{wet}} = 0,0270\ (-31,5\%)$, respectively. Observing the stress-strain curves, it can be noticed that the "wet" samples show a very short elastic phase that quickly goes into plasticization. This means that compared to the "dry" specimens, they are more deformable. This phenomenon can be attributed to the reduction of $T_g$ induced by the immersion in hot water, which leads to an increase in the mobility of the molecular chains and therefore to a reduction in the stiffness and strength of the material.

A portion of the samples that were subjected to conditioning were selected to undergo a drying process. The purpose was to monitor the deformations during drying and then determine, with other tensile tests, whether the material was able to recover its original mechanical characteristics after all the absorbed water was extracted. During the almost 250-hour drying process, the samples were instrumented with an extensometer, and it was possible to observe that the sample contracts (reaching strain around 0,01 in contraction) as the water exits it. One possible explanation for this phenomenon is that as the water exits the material, it frees up the voids present in the resin, which can collapse causing contraction and shrinkage. Another observation that can be made regarding this phase of the project is that the samples do not recover their initial mass. In fact, weighting the samples before conditioning, after immersion, and after drying, residual mass increase was observed. The reason can be attributed to any remaining moisture trapped in the material or irreversible chemical reactions that develop between the resin and water molecules, causing the formation of oxide products that remain deposited on the material, increasing its mass. Once dried, these specimens were also tested under tension, and the results revealed interesting findings. Contrary to what has been reported in the literature, these tests showed the resin's inability to recover its original mechanical properties. The behavior highlighted by the stress-strain curves is indeed elastic-fragile, with the total absence of a plastic phase. The measured Young's modulus approach the "dry" one, $E_{dried} = 3,17\ GPa\ (-0,9\%)$, while stress and strain at fracture are much lower: $\sigma_{brk_{dried}} = 43,34\ MPa\ (-37,7\%)$ and $\varepsilon_{brk_{dried}} = 0,0270\ (-64,5\%)$.

The second testing phase was conducted using two Fiber Bragg's Grating sensors directly incorporated into the resin specimens: FBG6463 and FBG6466. Due to their fragility and high cost, even more attention was necessary during the production phase of the specimens. These sensors allow real-time measuring of the deformations that develop in the material and trace them back to mechanical perturbations, temperature, and humidity variations. Their first use was throughout the manufacturing process, monitoring all the deformations and the residual stresses that were creating in the material during the heating, curing, cooling and extraction phases. By analyzing the wavelengths recorded by the fiber optic sensors, it was possible to

determine that the specimens developed residual compression stresses during their production process, totaling $\varepsilon_{manufacturing} = 7975{,}15\ \mu\varepsilon$ and $\sigma_{manufacturing} = 25{,}55\ MPa$ in compression (calculated as averages between the two sensors).

As for the specimens without sensors, after the manufacturing process, these two components were immersed in hot water along with a "sentinel" specimen that was used for comparison and weighted daily. Unlike the previous conditioning cycle, during this one, the wavelength detected by the sensors was continuously recorded. These collected data allowed the calculation of the deformations developed during the moisture absorption. The trend of the obtained strains is not monotonic. In fact, the deformations show a rapid initial growth, leading to a maximum peak of 8465 $\mu\varepsilon$, after which a descending phase begins until a stable value is reached around 6153,5 $\mu\varepsilon$. One possible explanation for the initial rapid growth could be the significant difference between the moisture inside the resin (0%) and that in the water tank (100%), resulting in rapid water absorption. The absorption dynamics are therefore faster than the relaxation dynamics of the material, causing a large and rapid deformation. Moreover, the material initially accumulates water in the outermost part of its volume, developing large strains, then the water begins to penetrate deeper, causing a decrease in hydrostatic pressure on the surface of the material. This reduces the force on the specimens and causes a decrease in deformations. A contribution to the relaxation of the resin is also given by the development of hydrolysis chemical reactions that break the chemical bonds within the resin and reduce the material's mechanical properties. This conditioning cycle lasted 1469 hours and generated a moisture uptake of 7,24% on the sentinel specimen.

The next step in the experiment was to test the previously immersed specimens under tension, this time collecting data on the deformation from both the extensometer and the sensors embedded in the specimens. The motivation behind this was to ensure that the sensors could maintain adhesion with the material even after conditioning phase. Adhesion between the material and the sensor coating is essential for the proper load transfer and therefore for the correct measurement of strains. The results obtained showed that the FBG6463 sensor was unable to satisfactorily measure the deformations of the first specimen. Its failure is likely due to the penetration of water into the interface between the coating and the resin, causing it to slip. Additionally, water molecules may have caused a loss of mechanical properties of the fiber, which may have caused its breakage and subsequent signal loss. On the other hand, the FBG6466 sensor seems to respond better and can measure deformations up to a value of 8000 $\mu\varepsilon$, beyond which there is a signal loss. The results provided by the extensometer for these two specimens and the "sentinel" one aligns with those obtained from the unsensorized specimens, although there was a reduction in maximum stresses and strains, likely due to the fact that these specimens were immersed for longer than the previous ones.

Finally, DSC analyses were performed on dry, wet, and dried resin samples to investigate any changes in $T_g$ and thus justify the changes in mechanical properties in the various phases. The results have confirmed that the immersion in hot water caused a significant reduction in $T_g$ and therefore a reduction of the strength of the resin.

The preliminary work carried out in this thesis, although complex, can be further deepened by studying the reasons for the malfunctioning of sensors equipped with a polyimide coating. It is important to discover the reasons for the signal loss and the failure to monitor deformations beyond the threshold of 8000 $\mu\varepsilon$. It would be interesting to understand whether the loss of adhesion occurs between the resin and the coating or between the coating and the sensor core. Further investigation could involve a chemical study of the reactions that occur between the material and the water molecules in order to understand whether oxides are formed that deposit on the sample, increasing its mass without generating additional deformations.

To complete this study, it would be of great interest to measure the effects of humid environments and temperature variations on composite materials, which are actually used in the aerospace industry. It would therefore be necessary to create samples that, in addition to the matrix and the optical fiber sensor, are enriched with reinforcement fibers. For these new specimens, it may be useful to perform tests at different levels of humidity and temperature, using a climatic chamber where the desired levels can be selected. This may increase the realism and accuracy of the experiments that are conducted.

# 5 Bibliography

[1] V. Giurgiuntiu, Structural Health Monitoring of Aerospace Composite, Elsevier, 2016.

[2] E. Kececi, «Highly durable hydrophobic thin films for moisture prevention of composite,» in *PhD thesis*, Wichita State University, 2012.

[3] G. Sala, L. Di Landro, A. Airoldi, P. Bettini, Dispense di tecnologie e materiali aerospaziali - Chapter 32 - Materiali compositi: Legge costitutiva ortotropa, Politecnico di Milano.

[4] Giuseppe Sala. Luca Di Landro, Dispense di tecnologie e materiali aerospaziali - Processi produttivi in autoclave, forno e pressa, Politecnico di Milano.

[5] G. Sala, L. Di Landro, A. Airoldi, P. Bettini, Dispense di tecnologie e materiali aerospaziali - Chapter 46 - Effetto della fatica e dell'ambiente sui compositi, Politecnico di Milano.

[6] B. C. Ray, D. K. Rathore, Environmental damage and degradation of frp composites: A review report., 2015.

[7] Iuri BCM Rocha, Sibrand Raijmaekers, Rogier PL Nijssen, and Frans P Van der, Hydrothermal ageing of glass/epoxy composites for wind turbine blades., Copenhagen: ICCM, 2015.

[8] A. Bayatpour, «Moisture Effects on Properties of Polymeric Composite Laminates,» Concordia University, Montreal, 2019.

[9] Erkan Kececi and Ramazan Asmatulu, «Effects of moisture ingressions on mechanical properties of honeycompo-structured fiber composites for aerospace applications,» *The International Journal of Advanced Manufacturing Technology,* 2017.

[10] M. Li, «Temperature and moisture effects on composite materials for wind turbine blades,» Montana State University-Bozeman, College of Engineering, 2000.

[11] B.C. Duncan and W.R. Broughton, «Absorption and diffusion of moisture in polymeric materials,» 2007.

[12] Bankim Chandra Ray, Rajesh Kumar Prusty, and Dinesh Kumar Rathore, «Fibrous polymeric composites: environmental degradation and damage,» in *CRC Press*, 2018.

[13] SG Prolongo, MR Gude, and Alejandro Ureña, Water uptake of epoxy composites reinforced with carbon nanofillers. Composites Part A: Applied Science and manufacturing, 20112.

[14] Maria Pia Falaschetti, Matteo Scafé, Nicola Zavatta, and Enrico Troiani, Hygrothermal ageing influence on bvi-damaged carbon/epoxy coupons under compression load, 2021.

[15] Kishora Shetty, Ramesh Bojja, and Shylaja Srihari, «Effect of hygrothermal aging on the mechanical properties of ima/m21e aircraft-grade cfrp composite,» in *Advanced Composites Letters*, 2020.

[16] Dimitrios Mamalis, Christophe Floreani, and Conchúr M Ó Brádaigh, «Influence of hygrothermal ageing on the mechanical properties of unidirectional carbon fibre reinforced powder epoxy composites,» in *Composites Part B: Engineering*, 2021.

[17] Olesja Starkova, Samuel T Buschhorn, Evgenij Mannov, Karl Schulte, and Andrey Aniskevich, «Water transport in epoxy/mwcnt composites,» *European Polymer Journal*, 2013.

[18] Andrey E Krauklis, Abedin I Gagani, and Andreas T Echtermeyer, «Hygrothermal aging of amine epoxy: reversible static and fatigue properties,» in *Open Engineering*, 2018.

[19] A. Krauklis, Environmental aging of constituent materials in fiber-reinforced polymer composites, 2019.

[20] Jia-Yu Ye and Lu-Wen Zhang, «Damage evolution of polymer-matrix multiphase composites under coupled moisture effects,» in *Computer Methods in Applied Mechanics and Engineering*, 2022.

[21] L. Carminati, «Hygrothermal aging in composite structures: literature review and perspectives,» in *Master's thesis*, Politecnico di Milano, 2021.

[22] F.-G. Yuan, Structural Health Monitoring (SHM) in Aerospace Structures, Elsevier, 2016.

[23] Helena Rocha, Christopher Semprimoschnig, João P. Nunes, «Sensors for process and structural health monitoring of aerospace composites: A review,» *Science Direct*, 2021.

[24] P. Bettini, «Fiber Optics,» in *Smart Structures: Types, Technology and Applications*, Politecnico di Milano, 2021.

[25] M. Iazzi, «Evolution of residual strains due to manufacturing and hygrothermal effects on an aeronautical epoxy resin,» in *Master's Thesis*, Politecnico di Milano, 2021.

[26] Nezih Mrad and Henry C.H. Li, «Fiber Optic Systems: Optical Fiber Sensor Technology and Windows,» 2008.

[27] G. D. Paolo, «Development of a fiber optic technique for process monitoring of composite structural elements,» in *Master's thesis*, Politecnico di Milano, 2018.

[28] Jasjot K. Sahota, Neena Gupta, and Divya Dhawan, «Fiber Bragg grating sensors for monitoring of physical parameters: a comprehensive review,» Punjab Engineering College, 2020.

[29] G. Sala, L. Di Landro, A. Airoldi, P. Bettini, «Materiali Intelligenti,» in *Dispensa di Materiali e Tecnologie Aerospaziali*, Politecnico di Milano.

[30] P. Bettini, «Embedding Techniques,» in *Smart Structures: Types, Technology and Application*, Politecnico di Milano, 2021.

[31] Jianxin Zhang, Xueyun Shen, Miao Qian, Zhong Xiang, Xudong Hu, «An optical fiber sensor based on polyimide coated fiber Bragg grating for measurement of relative humidity,» *Science Direct*, 2021.

[32] Jun-Yi Guo, Bin Shi, Meng-Ya Sun, Cheng-Cheng Zhang, Guang-Qing Wei, Jie Liu , «Characterization of an ORMOCER®-coated FBG sensor for relative humidity sensing,» *Science Direct*, 2021.

[33] Jun-Yi Guo, Bin Shi, Meng-Ya Sun, Wei Cheng, Cheng-Cheng Zhang, Guang-Qing Wei, Xing Wang, «Application of PI-FBG sensor for humidity measurement in unsaturated soils,» *Science Direct*, 2022.

[34] Nigel A David, Peter MWild and Ned Djilali, «Parametric study of a polymer-coated fibre-optic humidity sensor,» *Measurement Scince and Technology*, 2012.

[35] Teck L. Yeo, Tong Sun, Kenneth T. V. Grattan, David Parry, Rob Lade, and Brian D. Powell, «Polymer-Coated Fiber Bragg Grating for Relative Humidity Sensing,» *IEEE Sensor Journal*, 2005.

[36] Pascal Kronenberg and Pramod K. Rastogi, Philippe Giaccari and Hans G. Limberger, «Relative humidity sensor with optical fiber Bragg gratings,» *Optics Letters*, 2002.

[37] P. Aceti, «Sensing principles of FBG in humid environments,» Politecnico di Milano, 2023.

# 6   List of figures

# 7 List of tables